Time-series analysis of oscillating red giant stars

Dennis Stello

A thesis
submitted for the degree of
Doctor of Philosophy
at the
University of Sydney

August 2006

Front cover design by Hans Bruntt and Dennis Stello using Gimp. The background image is a composite image of three images of the open stellar cluster M67 taken with the Danish 1.54m telescope at La Silla (Chile) using the V, B and I filters, respectively. The images were taken during the M67 campaign described in Chapters 5 and 6. The composite image was created with the IDL program tctool.pro and Gimp to give it the final touch. Several of the stars discussed in this thesis can be seen in this image. Both red giants and blue stragglers are clearly visible.

The University of Sydney crest was kindly supplied by Thomas Mauch.

This thesis is published by Dennis Stello.

ISBN 87-991685-0-2 (Hardback)
ISBN 87-991685-1-0 (Paperback)

To Lena Sahm

May you keep shining bright. . . lekker zo he'!?

Declaration of Originality

This thesis contains no material which has been presented for a degree at this or any other university, and, to the best of my knowledge and belief, contains no copy or paraphrase of work published by another person, expect where duly acknowledged in the text.

Note that Chapters 3–6 are reproductions of papers produced in collaboration with other researchers (Stello et al., 2004, 2006c,b,a). Nevertheless, they are a valid part of my thesis because the majority of the work can be credited as my own. The division of work between the authors is explained at the beginning of each of these chapters.

Dennis Stello

Preface

In this preface I would take the opportunity to acknowledge the support and thank the people that made the last three years an exciting, pleasant and memorable time.

Financial assistance was obtained from the International Postgraduate Research Scholarship (funded by the Department of Education, Science and Training), the International Postgraduate Award (awarded by the University of Sydney), the Denison merit award (awarded by the School of Physics, University of Sydney), Postgraduate Research Support Scheme (funded by the University of Sydney), Denison funding and the Relocation Scholarship (funded by the School of Physics, University of Sydney), ASA Travel Assistance (funded by the Astronomical Society of Australia), the Australian Research Council and the Danish Agency for Science, Technology and Innovation (SNF). I would also like to thank Derek Buzasi for his support during my PhD studies.

I thank my supervisor Tim Bedding for asking me to come to Australia and his subsequent efforts to make it a pleasant time at the University of Sydney. The entire astrophysics group at the School of Physics should have credit for their contribution towards creating a positive and relaxed (not lazy!) atmosphere, which I have appreciated. Thanks to Blair for helping me out rotating tables in LaTeX at the latest hour.

A significant part of my PhD work was focused on the M67 campaign. It has been a very valuable learning experience to run this campaign with participating scientists from all over the world, and I would like to thank all participants who joined to support this ambitious project. I will never forget the six-week observing run... almost like a Hollywood science movie. It was very exciting! A special thank goes to Torben Arentoft and family for their visit here in Sydney, which provided a good kick-start of the reduction of the huge data set of M67 and further gave me the tools to proceed the work independently. Not to forget the nice weekends in Manly both above and under water. Sku' det være en anden gang!? `;O)`

During my PhD studies I visited the asteroseismology group at Aarhus University led by Jørgen Christensen-Dalsgaard, and I appreciate very much the hospitality. I would like to thank my office mates at Aarhus University, Torben Arentoft and Michaël Bazot for a good and productive atmosphere and the hard practise of the Danish language by Michaël... "En øl, tak!". Exactly this phrase might have been the key to one if not the most enjoyable paper I have ever written. Without the hard work by all co-authors and the Belgian beer the paper would never have seen bright daylight. Due to its highly controversial humorous content the paper was classified and not released for peer-review publication but was shown as a poster at the "Stellar Pulsation and Evolution Workshop" in Rome 2004. For completeness it is included as an appendix in this thesis...sorry Hans `;0)`

Special thanks goes to Hans Kjeldsen at Aarhus University, my associate supervisor, for fruitful discussions about time-series analysis and what not, both during my visit at Aarhus University and the early morning hours on the phone while I was in Sydney.

Tim Bedding should be thanked for reading through most of my publications and his efforts to teach me rules to navigate through the non-consistent English grammar, which all together have greatly improved the writing style throughout this thesis.

I thank my (office) mate in Sydney Chris Boshuizen, for all the nice training sessions in the pool and out in the ocean. Thank you for being so open minded regarding freediving, my other passion in live, and believing me fully when I said you could do at least 4 minutes the first time...it is all in your mind! Also thanks for the various dinner and cocktail parties, Aussie, Japanese and Newtown style.

Thanks to the parrots that come visit during the early hours to get fed. You guys make me start every day with a smile, and ensures I do not sleep till late in the morning `;0)`

Finally, a big warm knuffel to my wife Kristine. Thanks for your encouragement and support towards choosing Sydney instead of staying put. Grazie mia principessa grazie...I can not say that enough times...mille grazie `8-)`

Dennis Stello
Sydney, August, 2006

Contents

List of Tables

List of Figures

Chapter 1

Introduction

Stars are the building blocks of the Universe and, as such, are essential to understanding many aspects of astrophysics. Our understanding of cosmology, galaxies and planetary formation all depend on stellar evolution. The chemical evolution of galaxies and the Universe has been, and still is, taking place inside stars, and they are the creators of all heavy elements, which are essential for the formation of planets. Further, tests of stellar evolution theory are key to understanding many aspects within physics such as the equation-of-state of matter, nuclear processes, convection and rotation. To understand how stars evolve we need to investigate stars in different evolutionary stages.

The goals of the work presented in this thesis are to investigate the prospects of applying asteroseismic techniques (see Sect. 1.2) to studying the interiors of red giant stars. The specific goals are to detect solar-like oscillations in red giants, and to characterise their oscillation properties, including mode amplitude, lifetime, and regularity in frequency spacing. On this basis it is desired to compare these characteristics to solar-like oscillations of main-sequence stars and to highlight possible limitations of applying asteroseismology to red giants. To facilitate this, I will implement realistic simulations of stochastically excited and intrinsically damped oscillations and to develop new methods for characterising the oscillations from observations. In particular, I want to use the simulations to reveal information about the mode lifetime, which I found during my MSc. (Stello, 2002) to be a critical parameter for the interpretation of the observations. However, those conclusions were based on a few simulations and no measurements of the mode lifetime were performed. At that time, the only star for which mode lifetimes had been measured was the Sun (Chaplin et al., 1997).

In this chapter I will put these goals in the context of what has been achieved so far using asteroseismology on various types of cool stars that exhibit solar-like oscillations, with emphasis on the red giant stars. First, I introduce in Sect. 1.1 the evolution of red giant stars, give the typical values of the global parameters

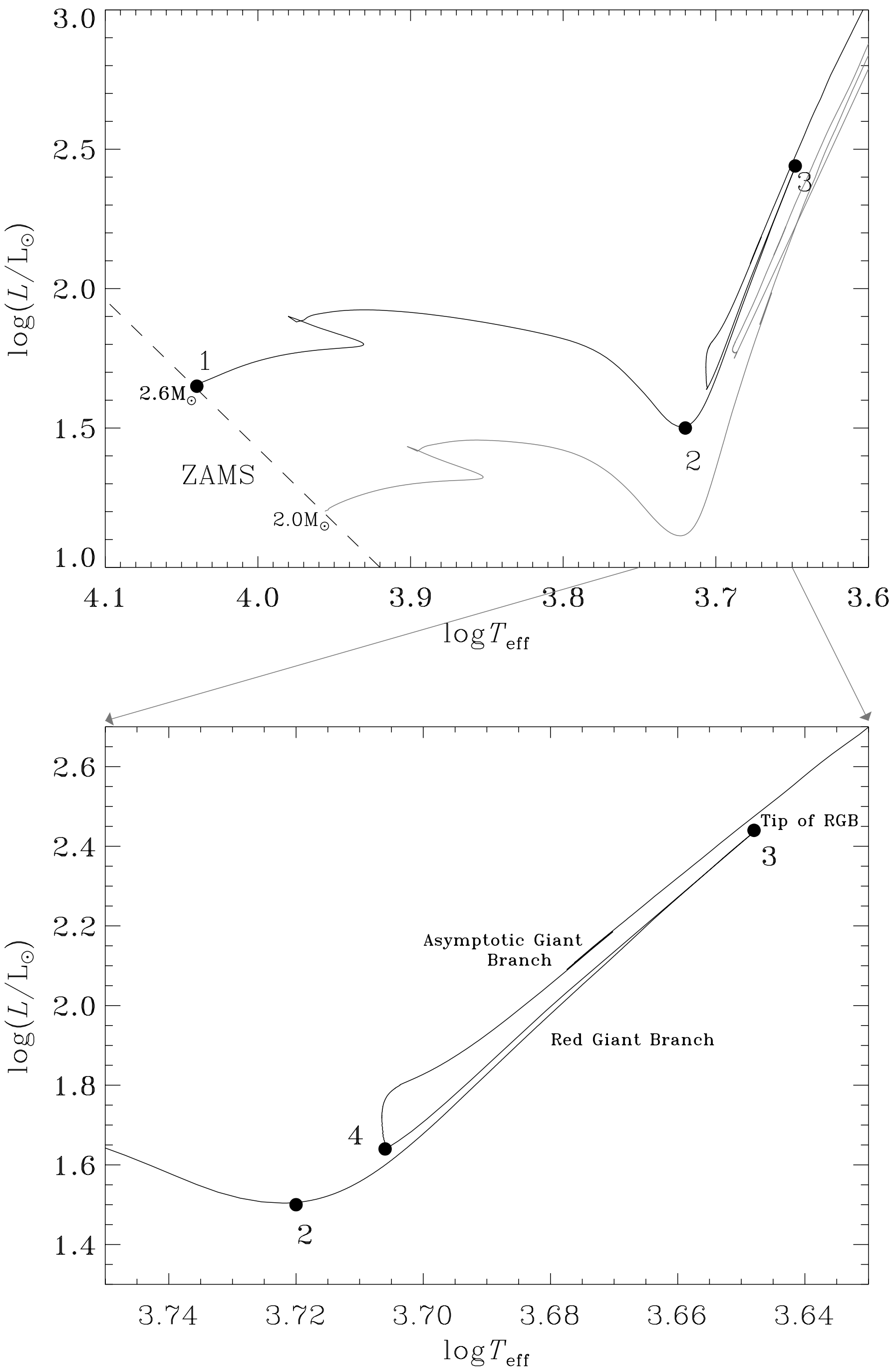

Figure 1.1: Hertzsprung-Russell diagram. Stellar evolution tracks are shown for 2.6 $M_\odot$ (black curve) and 2.0 $M_\odot$ (grey curve) (BaSTI database Pietrinferni et al., 2004). The diagonal dashed line indicates the zero age main sequence (ZAMS). Dots marks different evolutionary stages (see text).

and explain why these parameters can be difficult to measure. I then introduce the basic concept of asteroseismology in Sect. 1.2. For the non-expert in asteroseismology, I have included a short introduction to how solar-like oscillations can be characterised and how these characteristics can be used to obtain information about interior properties of the stars (see Sect. 1.3). An overview of the most resent observational results in the field is given in Sect. 1.4, and in Sect. 1.4.2 I finish this chapter by putting one of the main projects of this thesis in the framework given in the previous sections.

1.1 Red giant stars

In this section I will introduce red giant stars and explain how they fit in the broad picture of the evolution of stars. An excellent introductory text on stellar evolution has been written by Christensen-Dalsgaard (1995) (see also Kippenhahn & Weigert, 1990).

According to theoretical calculations of stellar evolution, stars will expand when the hydrogen in their core is exhausted, which causes them to be more luminous and cooler. They evolve to become red giants. Stars of a large mass range, corresponding to main-sequence spectral classes from late B to K, all end up in roughly the same part of the Hertzsprung-Russell (HR) diagram when they evolve from being main-sequence stars (stage 1 in Fig. 1.1, top panel) to become red giants (after stage 2) with spectral classes from late G to M. Here, the evolutionary tracks become very closely spaced (see Fig. 1.1, top panel), which makes it difficult to estimate the mass, and hence to determine the progenitor, of a red giant star from its position in the HR diagram. This is further illustrated in the HR diagram plotted in Fig. 1.2, which shows stellar evolution tracks for masses ranging from 1 to $20\,\mathrm{M}_\odot$ (black solid curves). Red giant stars typically have radii in the range 2–$100\,\mathrm{R}_\odot$ (Hatzes & Cochran, 1998) and luminosities of a few tens to a couple of thousand times that of the Sun. During the expansion, the surface gravity, rotation rate and temperature all decrease. Typical values are: $\log g \sim 1.5$–$3.0\,\mathrm{cm/s^2}$, $v \sin i \sim 1$–$10\,\mathrm{km/s}$ and $T_{\mathrm{eff}} \sim 3500$–$5000\,\mathrm{K}$ (Allen, 1973; Pasquini et al., 2000).

The low temperature in the outer envelope causes the opacity to become high, blocking much of the radiation. As a consequence, radiation will not be efficient enough to transfer all the energy outwards through the star. Hence, the dominant mechanism of energy transport is convection. Via turbulent gas motion, this process transfers energy mechanically as hot gas cells rise and release energy to cooler surroundings, while cooled gas moves downward between the hot cells.

Stars undergo dramatic evolutionary changes during the red giant phase. As a star ascends the red giant branch (stage 2 to 3 in Fig. 1.1, bottom panel) the convection zone extends inwards and in some cases might reach all the way into the region of nuclear fusion, which has a significant effect on the evolution due to mixing of elements (Gray & Nagel, 1989). When the star reaches the tip of the red giant branch, the triple-alpha process ignites, which starts He-core burning (stage

3). This either happens as a runaway process called the helium flash (for low mass stars $\lesssim 2\,M_\odot$) or gradually (for higher mass stars). In both cases the star will quickly contract and settle down on the horizontal branch (stage 4). When helium is exhausted in the core the star again expands, this time ascending the asymptotic giant branch with a hot core of carbon (beyond stage 4). Whether the star will undergo new nuclear fusion processes after this stage depends on its mass.

The parts of the evolution just described are within a very narrow temperature range. In addition, a star can have very similar luminosities as it 'moves' up and down the red giant branch and up the asymptotic giant branch. This makes it very difficult and sometimes impossible to determine the evolutionary state of these stars, despite their interior being quite different. This ambiguity was clearly illustrated for the red giant ξ Hya by Stello (2002) and Christensen-Dalsgaard (2004). Asteroseismology carries the potential of determining much more precisely the evolutionary state of these stars from investigations of their interiors.

1.2 Asteroseismology

Asteroseismology provides a unique tool to investigate the interior of stars. A star is a sphere of gas that, if excited, can oscillate in many different modes. In cool stars, including the Sun, the gas undergoes convection near the surface. This turbulent gas motion constantly excites (stochastically) standing sound waves that are intrinsically damped, causing the star to oscillate in many different modes simultaneously, each with a slightly different frequency (Goldreich & Keeley, 1977). The frequencies depend on the internal sound speed, which in turn depends on the physical properties of the stellar interior like density, temperature and composition. Each mode carries information about the stellar interior that is different from that of any other mode. Hence, by measuring frequencies from many different modes we can reconstruct the sound speed profile of the star to learn about physical properties that we otherwise cannot measure (Brown & Gilliland, 1994; Christensen-Dalsgaard, 2004). This analysis, called asteroseismology, is analogous to the seismic study of the Earth's interior. These convectively driven oscillation modes were first observed in the Sun as tiny variations (both in luminosity and velocity) with periods of roughly five minutes (Leighton et al., 1962), and are now generally known as solar-like oscillations. Because the dominant restoring force is pressure, the modes are called p-modes, in contrast to g-modes observed in e.g. white dwarfs, where the restoring force is buoyancy (gravity) (Winget et al., 1991).

Seismology has proved to be very powerful in the solar case (called Helioseismology), where it has provided dramatic insight into the properties of the solar interior (Christensen-Dalsgaard, 2002). Applying the same technique to other stars promises a similar leap in understanding their interiors (Elsworth & Thompson, 2004). It should be noted that because the disk of a distant star cannot be resolved, unlike in the solar case, high degree modes (Sect. 1.3), which require high spatial resolution, cannot be detected due to cancellation in whole-disk integrated light.

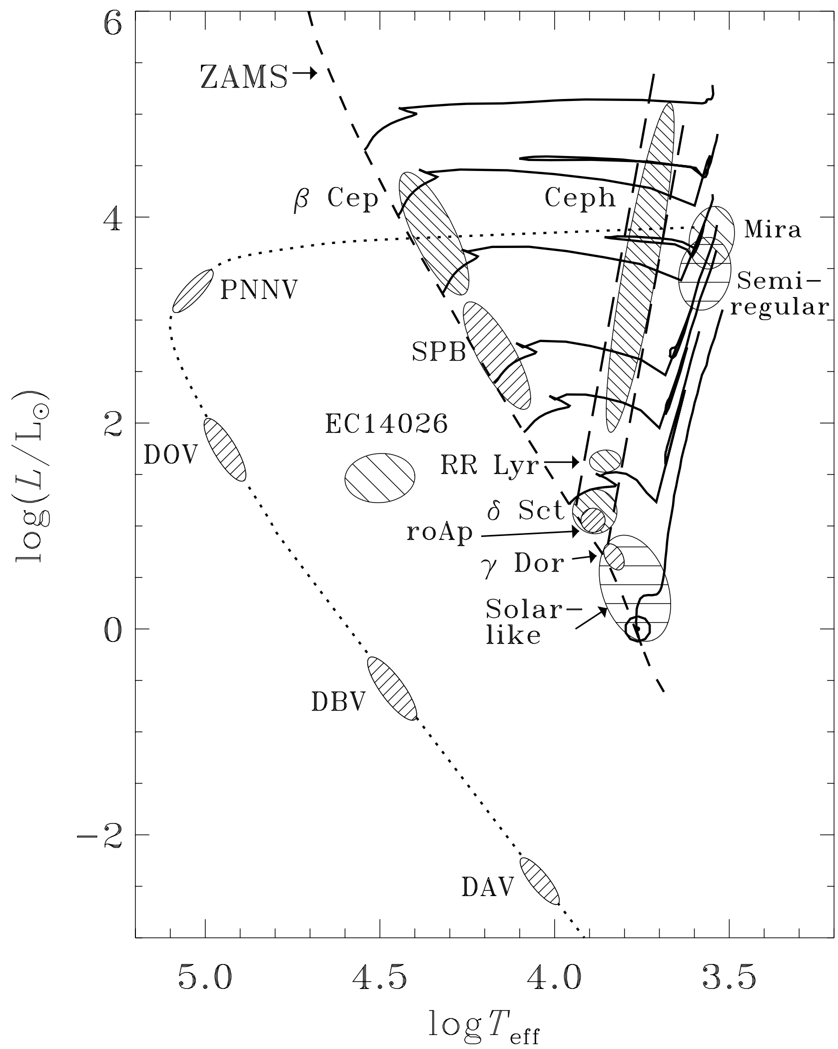

Figure 1.2: The Hertzsprung-Russell diagram with indicated names and approximate locations of known groups of pulsating stars. The diagonal dashed line indicates the zero age main sequence (ZAMS). The nearly vertical long dashed lines show the location of the instability strip. Stellar evolution tracks (black curves) are shown for 1, 2, 3, 4, 7, 12 and 20 $M_\odot$. The location of the 'Mira' and 'Semi-regular' pulsators is in accordance with Schultheis et al. (2004). (The figure is slightly modified compared to the original, which was kindly supplied by J. Christensen-Dalsgaard.)

We can therefore not expect to unveil the same degree of detail (especially about the surface structure) of distant stars as in the solar case. Fortunately, information about the stellar core, and hence stellar age, can to a great extent be determined by the low-degree modes.

Apart from the convectively driven (or solar-like) oscillations, which are found in cool stars like the Sun, we see stellar oscillations in other parts of the HR diagram as well. Figure 1.2 gives a schematic overview of the different regions in the HR diagram where oscillations occur. Some of the most commonly known pulsating stars are located inside the instability strip, which is between the two parallel long-dashed lines. Here we find the Cepheids and the δ Scuti stars. In these stars the driving comes from the κ-mechanism, which is due to opacity variations (Baker & Kippenhahn, 1962; Cox, 1980). However, as pointed out on page 1, this thesis is aimed at the investigation of solar-like oscillations. Hence, when using the term 'asteroseismology' in the following I refer to the study of solar-like oscillations.

1.3 Properties of solar-like oscillations

For small displacements, global oscillation modes of a sphere (and hence of slowly rotating stars) can be characterised by a function ξ, which is a product of a radial component, $\xi(r)$, and a spherical harmonic, $Y(\theta, \phi)$ (also known from quantum physics). ξ could be any scalar perturbation (e.g. intensity or velocity) associated with the oscillation mode. With notation of Brown & Gilliland (1994)

$$\xi_{nlm}(r, \theta, \phi, t) = \xi_{nl}(r) Y_l^m(\theta, \phi) e^{-i2\pi\nu_{nlm}t} , \tag{1.1}$$

where r, θ, ϕ are the usual spherical coordinates, t is the time, and ν_{nlm} is the mode frequency, which depends on the set of mode quantum numbers (n, l, m) that define the mode structure. The radial order n specifies the number of nodes between the centre and the surface of the star. Since n is related to the depth structure of the mode, it is not directly observable. Figure 1.3 shows spherical harmonics of different values of l and m. The angular degree l, or rather $\sqrt{l(l+1)}$, is roughly speaking the number of wavelengths along the stellar circumference (Christensen-Dalsgaard, 2003). Thus high-degree modes show many variations (sign changes) across the stellar hemisphere. The azimuthal order m is the projection of l onto the stellar equator, thus taking values between $-l$ and $+l$.

When a wave associated with a given mode penetrates into the interior of a star it refracts due to the increasing sound speed, and therefore reaches a certain depth and moves outward again, to be reflected at the surface, etc. Modes of lower degree reach larger depths. A special case is the $l = 0$ mode, which is purely radial. This is schematically shown in Fig. 1.4.

As briefly mentioned on page 6, the stellar surface is not resolved when observing a distant star, causing high-degree modes to cancel out. This cancellation depends on both classical limb darkening (Gray, 1992) and on the kind of perturbation observed (e.g. intensity or velocity). In intensity one can only expect to observe modes

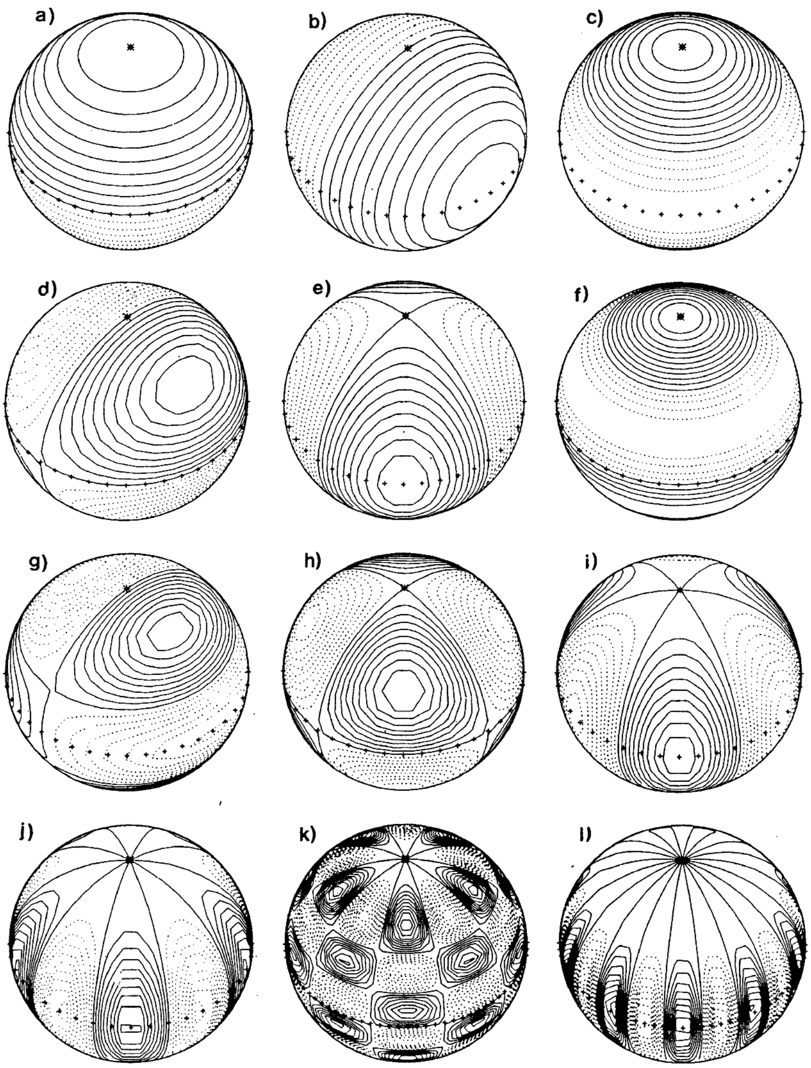

Figure 1.3: Contour plots of the real part of spherical harmonics Y_l^m (see 1.1). Positive contours are indicated by continuous lines and negative contours by dashed lines. The polar axis is inclined towards the viewer indicated by the asterisk. The equator is shown by "+++++". The following cases are illustrated: a) $l = 1$, $m = 0$; b) $l = 1$, $m = 1$; c) $l = 2$, $m = 0$; d) $l = 2$, $m = 1$; e) $l = 2$, $m = 2$; f) $l = 3$, $m = 0$; g) $l = 3$, $m = 1$; h) $l = 3$, $m = 2$; i) $l = 3$, $m = 3$; j) $l = 5$, $m = 5$; k) $l = 10$, $m = 5$; l) $l = 10$, $m = 10$. (The figure is copied from Christensen-Dalsgaard (2003).)

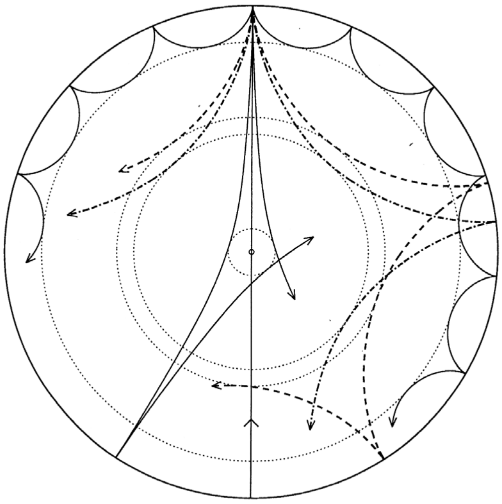

Figure 1.4: Wavefront propagation of sound waves inside a star. Modes of low degree l penetrate deeper into the star. A purely radial mode ($l = 0$) goes straight through the center. (The figure is copied from Christensen-Dalsgaard (2003).)

with $l = 0, 1$ and 2. However, due to the projection onto the line-of-sight, velocity measurements could be used to detect $l = 3$ as well. Higher degree modes show a very small response (see Fig. 1.5).

1.3.1 Distribution of frequencies and their amplitudes

In general, there is no simple relation between frequency, ν_{nlm}, and the quantum numbers n, l, and m. However, for non-rotating stars the frequencies are independent of m due to arbitrary orientation of the polar axis. For low-degree high-order modes ($l \ll n$), as we see in the Sun, asymptotic theory can be applied (e.g. Tassoul, 1980) and the frequency can be approximated by (with notation of Brown & Gilliland, 1994)

$$\nu_{nl} = \Delta\nu_0\big(n + \frac{l}{2} + \epsilon\big) - \frac{Al(l+1) - \eta}{n + l/2 + \epsilon}\,, \tag{1.2}$$

where $\Delta\nu_0$, A, ϵ, and η are constants involving integrals over the structure of the stellar interior. If we ignore the second term on the right-hand side (which is small), this equation tells us that the Fourier spectrum shows a regular series of peaks with a primary separation of $\Delta\nu_0$, called the *large separation*, between successive values of n. Modes with odd values of l fall halfway between even l modes, which are degenerate with those of successive n. In Fig. 1.6 (panel a) the solar frequency spectrum is shown, which clearly illustrates the characteristic comb pattern. In panel (b) the large separation, $\Delta\nu$, is indicated.

$\Delta\nu_0$ is roughly equal to the inverse of the sound travel time across the star, which is related to its mean density, $\bar{\rho} = M/R^3$ (Kjeldsen & Bedding, 1995). The

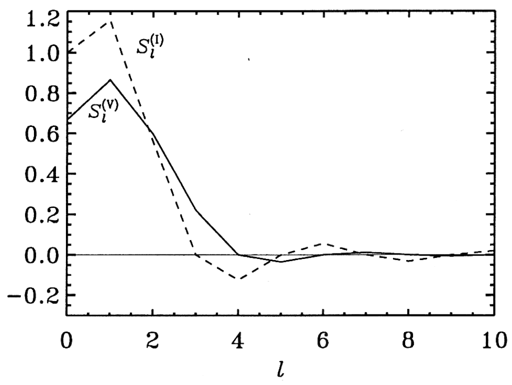

Figure 1.5: Response functions S for observations of intensity (I) and velocity (V) in light integrated over the stellar disk. (This figure is copied from Christensen-Dalsgaard (2003).)

last term on the right-hand side of Eq. 1.2, defined as $\delta\nu_{nl} \equiv \nu_{nl} - \nu_{n+1\,l-2}$, is called the *small separation*, and is indicated in Fig. 1.6 (panel b). This quantity is a measure of the molecular weight in the stellar core and hence the age of the star, due to the changing molecular weight during nuclear burning (Ulrich, 1986). Figure 1.7 shows the average small versus large separations for a series of evolution tracks with different masses. It illustrates how $\Delta\nu$ and $\delta\nu$ can measure the stellar mass and age, respectively.

Solar-like oscillations are seen in the Fourier spectrum in a broad frequency range reflecting the stochastic nature of the excitation mechanism (see Christensen-Dalsgaard & Frandsen, 1983). This frequency distribution is modulated by an envelope, which has a maximum "peak" and two tails reflecting the balance between acoustical energy generation by turbulent convection and damping. Figure 1.8 shows solar-like oscillations in six different stars from main-sequence stars to red giants. The position in the HR diagram of these stars can be seen in Fig. 1.9. The comparison of the amplitude distribution of the Sun with that predicted by theory shows a non-perfect match, especially at the high frequency range (Houdek et al., 1999, Fig. 8). The imprecise theoretical description of the amplitude distribution is primarily due to the lack of a proper theory of convection in a pulsating environment. Investigating the excitation and damping processes are therefore important, and this is one of the main goals of this thesis.

1.4 Observations of solar-like oscillations

The amplitudes of solar-like oscillations are extremely small ($\sim 10^{-6}$ in luminosity or less than a meter per second in velocity for main-sequence stars) and very hard to detect. For many years, asteroseismology suffered from a lack of data with the required precision, but recent improvements in observational techniques have changed

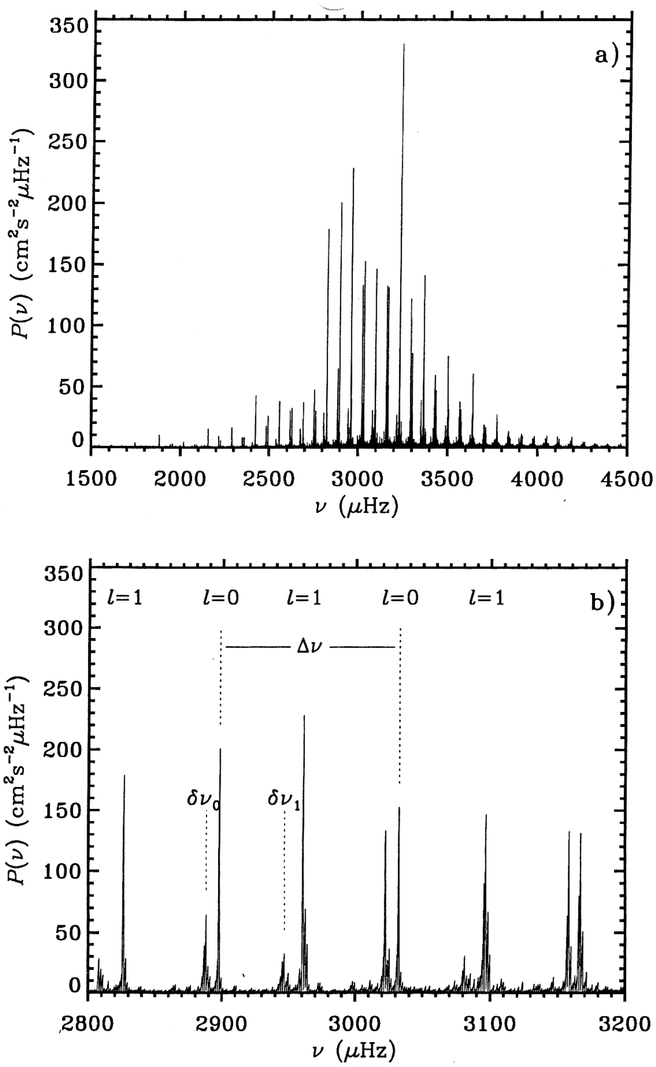

Figure 1.6: Power spectrum of solar oscillations obtained in velocity of whole disk integrated light (based on four months of observation from six sites). Panel (b) shows the detailed frequency pattern and the characteristic frequency spacings $\Delta\nu$ and $\delta\nu_{nl}$. The degree l of every second clearly visible mode is indicated. (This figure is copied from Christensen-Dalsgaard (2003).)

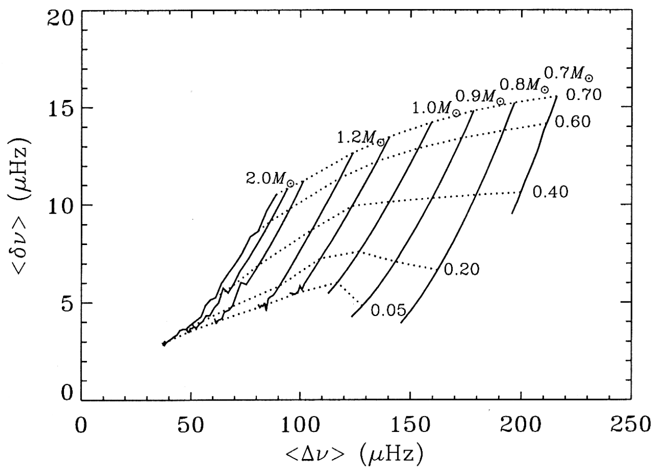

Figure 1.7: Evolution tracks (solid) and curves of constant central hydrogen abundance (dashed). Stellar masses and values of the central hydrogen abundance are indicated. (This figure is copied from Christensen-Dalsgaard (2003).)

the situation dramatically. Within the last five years, results on a dozen bright main-sequence and subgiant stars have seen clear detections of oscillations, demonstrating that asteroseismology is indeed a promising tool to probe stellar physics. These include the main-sequence stars α Cen A (Bouchy & Carrier, 2002; Butler et al., 2004), α Cen B (Carrier & Bourban, 2003; Kjeldsen et al., 2005), 70 Oph (Carrier & Eggenberger, 2006b), μ Ara (Bouchy et al., 2005) and β Vir (Carrier et al., 2005b), the subgiants α CMi (Procyon) (Martić et al., 2004), η Boo (Kjeldsen et al., 2003; Carrier et al., 2005a; Guenther et al., 2005), β Hyi (Bedding et al., 2001), δ Eri (Carrier & Eggenberger, 2006a), χ Eri (Carrier & Eggenberger, 2006a) and the metal-poor star ν Ind (Bedding et al., 2006) (see Figs. 1.8 and 1.9). Clear detections have further been shown for a few red giant stars, which will be discussed in the following section.

1.4.1 Solar-like oscillations in red giant stars

Theoretical calculations predict that convection becomes very vigorous for red giant stars and the oscillation amplitudes are therefore expected to be significantly higher than in the Sun and other main-sequence stars (Christensen-Dalsgaard & Frandsen, 1983). Based on these calculations Kjeldsen & Bedding (1995) proposed that the amplitude of solar-like oscillations would scale as L/M, which makes red giants promising candidates for asteroseismic analysis.

Oscillations in red giants have been studied by many authors. In the majority of cases these investigations were aimed at long-period (few days to several hundred days) and high-amplitude (several millimagnitudes) variability (e.g. Walker et al., 1989; Hatzes & Cochran, 1993; Horner, 1996; Edmonds & Gilliland, 1996; Henry et

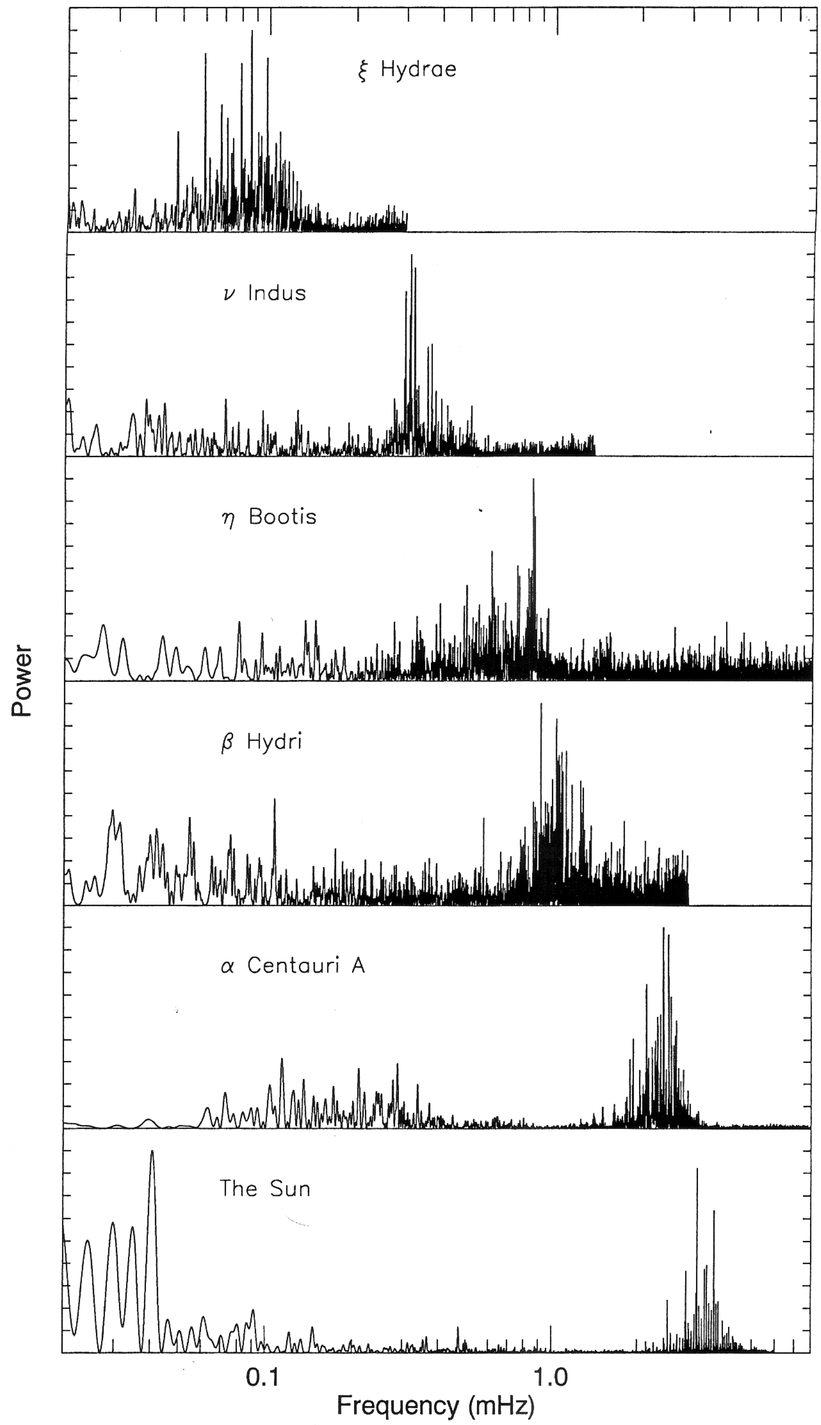

Figure 1.8: Power spectra of six stars (including the Sun). The power axis is arbitrary and the frequency axis is in logarithmic scale. (This figure has been kindly provided by Hans Kjeldsen.)

al., 2000; Hekker et al., 2006a). Those stars are more luminous than those addressed in this thesis, and the variations seen in these high-amplitude red giants are in many cases likely to be of a different origin than the solar-like oscillations discussed here (Hatzes & Cochran, 1993). However, solar-like oscillations have been reported in two rather luminous stars. Buzasi et al. (2000) report detection of solar-like oscillations in α UMa A (see Fig. 1.9), but this results is questionable according to Dziembowski et al. (2001). The other star is α Bootis (Arcturus) (see Fig. 1.9), which has been studied by several authors (e.g. Smith et al., 1987; Cochran, 1988; Belmonte et al., 1990; Hatzes & Cochran, 1994; Retter et al., 2003). There are general indications for periods of 2–3 days (corresponding to 3–6 μHz) in agreement with expectations from solar-like oscillations (see Eq. 6.2, page 101), but the presence of a typical solar-like frequency pattern is not established (Retter et al., 2003).

The first unambiguous detection of solar-like oscillations in a red giant star was by Frandsen et al. (2002), which was based on the work on the star ξ Hya in my MSc (Stello, 2002) (see Fig. 1.9). This result indicated new prospects for asteroseismology on evolved stars. The one month single-site observations showed periods of roughly 2–3 hours (corresponding to $\sim 90\,\mu$Hz), in agreement with expectations, and amplitudes of approximately 2 m/s in velocity, which was lower than expected from the scaling relation by Kjeldsen & Bedding (1995). Individual frequencies were extracted and a general frequency separation of 6–7 μHz was reported, in agreement with the expected large frequency separation of the comb pattern from solar-like oscillations (see Eq. 1.2, page 8). During my PhD, I used a large amount of simulations to investigate the intrinsic properties of the oscillations such as amplitude and mode lifetime (Stello et al., 2004, see Chapter 3). The most striking result from these studies was the apparent disagreement between the observed Fourier spectrum and the simulated spectra based on theoretical calculations of the mode lifetime by Houdek & Gough (2002). Using a new technique to measure the mode lifetime, I confirmed that the theoretical value of 15–20 days (Houdek & Gough, 2002) disagreed with the observations, which supported a much shorter value of roughly 2 days (Stello et al., 2006c, see Chapter 4). However, uncertainties were quite large due to the non-continuous data coverage.

Following that, Barban et al. (2004) observed two red giants (ε Oph, η Ser; see Fig. 1.9) from two sites, and could report clear detections of solar-like oscillations in both stars. However, due to bad weather the window function was not significantly better than the single-site observations of ξ Hya, and results on the large frequency separation were tentative. The location and amplitude of the peaks ($\sim 130\,\mu$Hz, ~ 2 m/s) in the Fourier spectrum of η Ser were slightly lower but in agreement with expectations. The more luminous star ε Oph also showed lower-than-expected amplitudes in the Fourier spectrum (according to the L/M amplitude scaling relation by Kjeldsen & Bedding (1995)). These results could indicate that the mode lifetime was short (a few days). A more detailed study of the ε Oph-data was performed by De Ridder et al. (2006), who reported that the observations indicated that only radial modes were excited to significant amplitudes, which was the same result found by Stello et al. (2004) for ξ Hya. De Ridder et al. (2006) further noted that the amplitude scaling relation for main-sequence stars by Samadi et al. (2005), which predict lower amplitudes than the L/M-scaling, agreed with the observations of ε Oph.

Theoretical calculations by Dziembowski et al. (2001) predict that only radial modes should be excited in red giant stars. This is supported by Christensen-Dalsgaard (2004), who derived a model of the red giant ξ Hya. It was shown that, despite the mode mass[1] being very similar for the radial and some non-radial modes (Teixeira et al., 2003), there was apparently significant radiative damping of the non-radial modes near the core, which suggested that radial modes would dominate the frequency spectrum. Interestingly, Hekker et al. (2006b) reported that non-radial modes are present in ε Oph and η Ser based on line profile analysis of previous observations by Barban et al. (2004). Their results were however not definitive for ξ Hya based on observations by Frandsen et al. (2002). It should be noted that the analysis by Hekker et al. did not give estimates of the amplitudes of the non-radial modes.

Very recently, Barban et al., (2006, in prep.) presented data of ε Oph obtained with the MOST satellite, which provided almost continuous coverage for 28 days in photometry. The Fourier spectrum showed an almost equally spaced pattern, in agreement with damped radial modes. With these data it was possible to measure the mode lifetime by fitting Lorentzian profiles to each mode (assuming only radial modes were present). The mode lifetime found was $2.68^{+1.05}_{-1.73}$ days.

In summary, asteroseismology applied to red giant stars started just before the work presented in this thesis was initiated. The field has been pursued by different groups and interesting results have been shown from both velocity and photometry measurements. Further comments are given in Chapter 7.

1.4.2 Asteroseismology on clusters

A significant part of this thesis is devoted to the investigation of solar-like oscillations in the old open cluster M67. The campaign on M67 was initiated in 2002 as a direct consequence of the detection of oscillations in the red giant ξ Hya (Frandsen et al., 2002; Stello, 2002). A similar campaign has been targeting the red giants in the globular cluster M4 (Frandsen et al., 2006, in prep.).

Observing a cluster of stars has the great advantage that we can assume the age and composition of the stars are roughly the same, leaving fewer free parameters to fit to the data. Detecting oscillations in an ensemble of cluster stars all in slightly different evolutionary states enables one to test more strongly stellar evolution theory.

In Fig. 1.9 we plot the cool part of the HR diagram shown in Fig. 1.2. The red giant stars observed in M67 (see Chapters 5 and 6) are indicated with black dots

[1]The mode mass is equal to the total energy of the mode divided by the surface rms velocity squared.

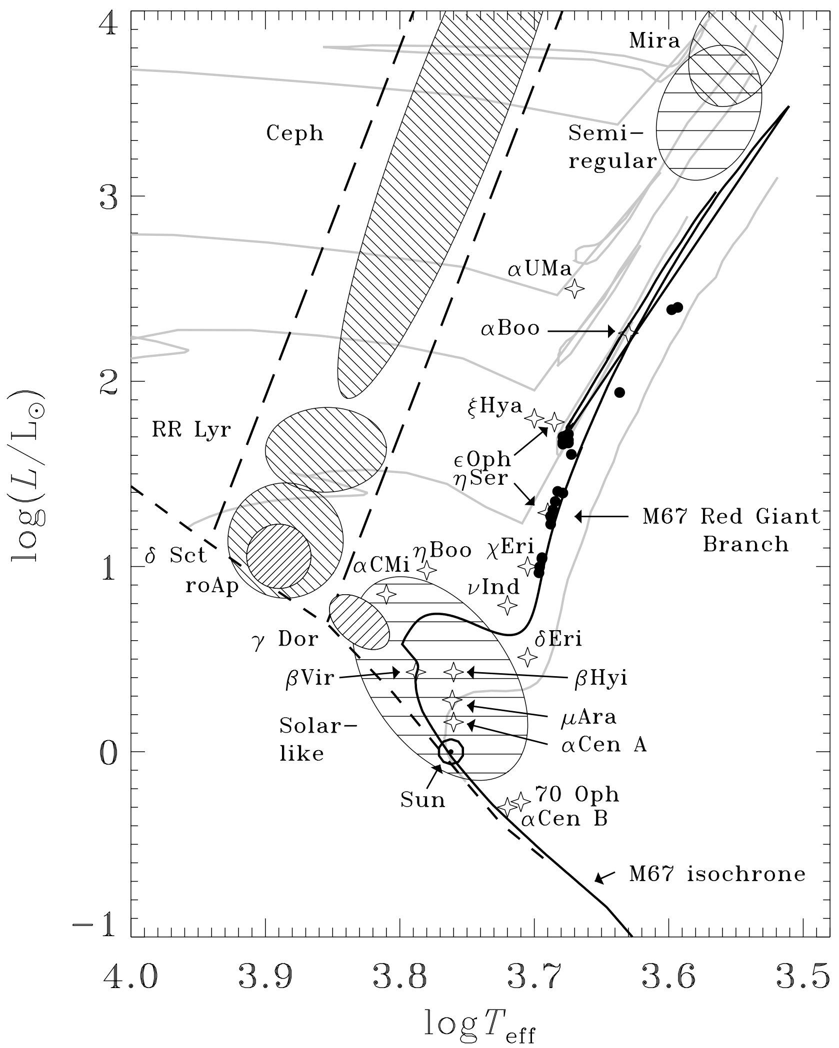

Figure 1.9: Similar to Fig. 1.2 but with focus on the region of solar-like oscillations. The isochrone is from the BaSTI database (Pietrinferni et al., 2004). Filled symbols are the red giant stars in M67. The power spectra of some of the plotted stars are shown in Fig. 1.8. (The figure is a modified version of the original, which was kindly supplied by J. Christensen-Dalsgaard.)

and an isochrone that matches that of the cluster is plotted as well. For comparison other selected cool stars in which solar-like oscillations have been reported are marked (see Sect. 1.4). This figure clearly illustrates that the red giants in M67 are excellent targets to investigate relatively "unexplored territory" of the HR diagram. Assuming the red giants in M67 are "typical", detection of oscillations in these stars would create a link of the oscillation characteristics between the less evolved (more solar-like) stars and the highly evolved giants in the semi-regular region.

Thesis outline

The goals of the thesis, described on page 1, are outlined in Chapters 2–6, which are reproductions of an unpublished report and four papers published or submitted to peer-reviewed journals. The work is presented in the chronological order by which it was carried out. Chapter 2 is a search for solar-like oscillations in red giant stars based on photometric time series from the STARE project. Chapter 3 describes a simulator to produce stochastically excited and intrinsically damped oscillations, and the application of using these simulations to infer characteristics of the red giant ξ Hya based on observations from my MSc (Stello, 2002). A new method to measure the mode lifetime of solar-like oscillations is described in Chapter 4. In Chapter 5, I introduce the M67 campaign including the reduction of the data. The time-series analysis of the red giant stars in M67 is given in Chapter 6. I conclude on the entire work presented in this thesis in Chapter 7, where I also give the future prospects for applying asteroseismology to red giant stars.

Chapter 2

The STARE data set of red stars

This chapter is a reproduction of an unpublished science report that I wrote in June 2003. I did the analysis based on data from the STARE Cygnus0 region, which was supplied by Timothy Brown. I was supervised by Tim Bedding. The STARE project was initiated to detect transiting giant exoplanets around distant stars in crowded fields of the sky. The STARE telescope has an aperture of 10 cm and obtain images with a scale of 10.8 arcseconds per pixel over a field of view 6.1 degrees square.

The data product comprised huge amounts of time-series photometry of red giant stars located in the observed fields, and could therefore potentially be valuable for the investigation of solar-like oscillations in these stars. Although I have not been further involved in the STARE project the reader is referred to the official STARE Web site (http://www.hao.ucar.edu/public/research/stare/stare.html) for further details.

2.1 Introduction

The purpose of this report is to investigate whether the STARE data are likely to reveal solar-like oscillations in the sample of red stars, which in many cases are believed to be giants. It is not the aim of this report to answer the question if it is possible to find a star in the STARE data sample which show solar-like oscillations. The investigation and discussion will be based on comparisons of observations with the predicted characteristics of solar-like oscillations for a selection of red stars from the STARE data set. A further comparison is made with a red giant star in which solar-like oscillations have clearly been detected.

2.2 Selection

The data sources used for this investigation are the two files cyg0_red00_ed_cl.bfl (time series and a bunch of quality control data) and cyg0_redpow.sav (photometric information and results from power spectrum analysis of each star). Both files were supplied by Tim Brown.

The time span of the series is roughly 60 days and the sampling interval is 15 min. In total there are 637 measurements for each of the 3347 red stars selected by having either $B - V > 0.9$ mag or $V - R > 0.9$ mag. Observing coverage is 11% of the 60 days ($N_{\rm data} \times T_{\rm samp}/60\,{\rm days}$).

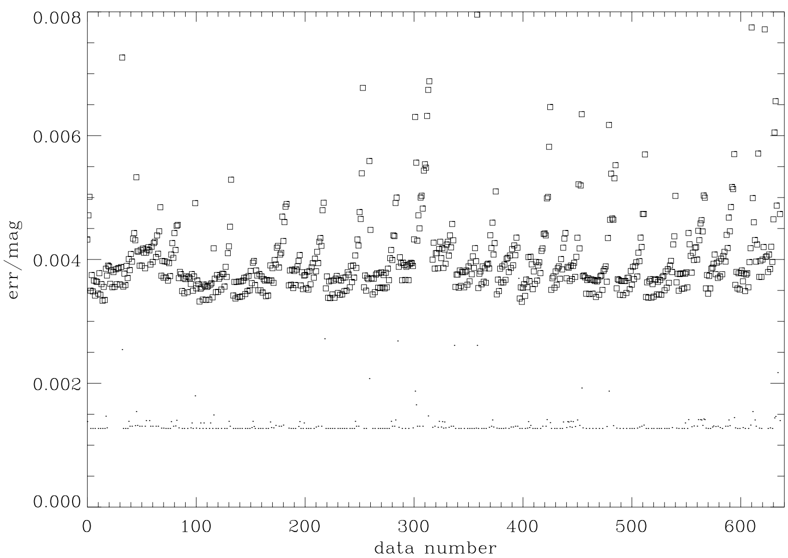

Figure 2.1: Error per data point for the entire time series for two stars (dots: a low noise star) (squares: a high noise star). The effect from airmass is clearly seen.

To be able to detect the tiny solar-like oscillations, we need as low noise as possible. Two typical examples of the error per measurement during the entire time series are shown in Fig. 2.1. In both cases, but most obviously in the low noise case (dots), there are jumps between a few distinct error values. The reason for this behavior is unknown to the author, but it looks like a truncation effect that have occurred during the data reduction.

The selection of a good low-noise test-sample was done by calculating the mean error for each star, and then selecting the best end of the error distribution (see Fig. 2.2). The selected stars are those with a mean error lower than 0.0015 mag, which gives a sample of 165 stars (using the median error did not effect the selection significantly). These stars are also the brightest stars in the STARE sample of red stars.

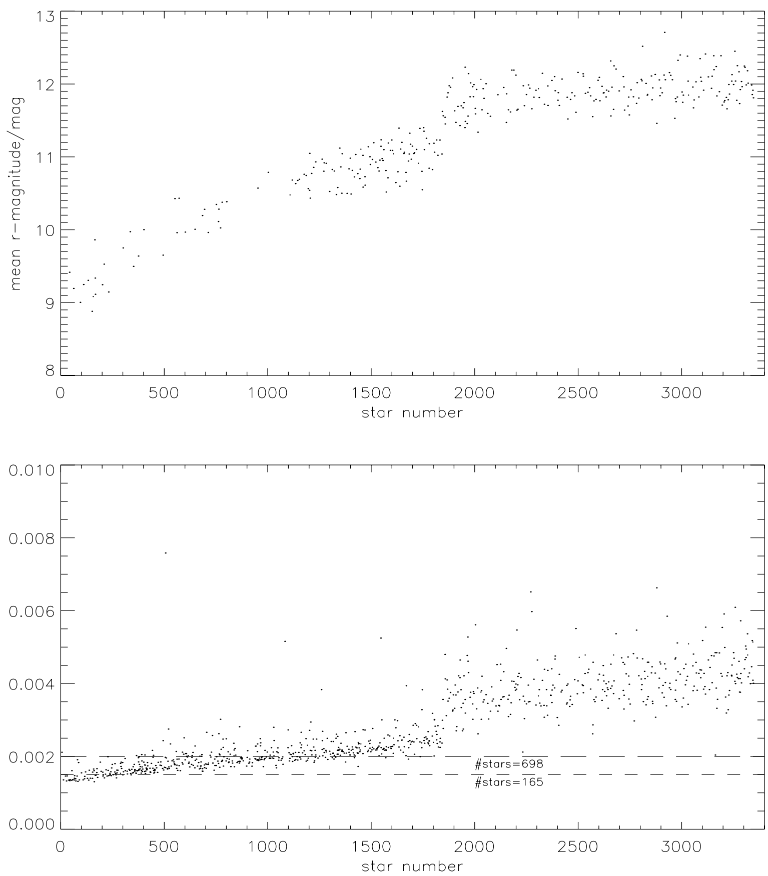

Figure 2.2: Mean error (bottom) and r-magnitude (top) per star for the entire set of 3347 red stars. The number of stars having a mean error between 0.0015 mag and 0.0020 mag, and those with mean errors below 0.0015 mag are indicated. The reason for the sloping trend is due to the ordering of the data in the cyg0_red00_ed_cl.bfl file according to increasing stellar magnitude for increasing star number. But the reason for the jump in error (and magnitude) is unknown to the author.

2.3 Amplitude estimates

2.3.1 Foundation: former results

The most firm pieces of evidence of solar-like oscillations in a red giant star has been observed (in velocity) in the star ξ Hya (Stello, 2002; Frandsen et al., 2002). The oscillation periods were detected to be roughly $P_{\xi\,\mathrm{Hya}} \sim 3$ hours. The amplitude in the Fourier spectrum was roughly 2 m/s based on a 30 day time series, while it was approximately 3–3.5 m/s for a 7 day window. The prediction based on the L/M scaling (Kjeldsen & Bedding, 1995) is $\mathrm{Amp_{est}} \simeq 4.7$ m/s. Furthermore, the red giant α Boo is likely to show p-mode oscillations (based on photometry) with a period of approximately $P_{\alpha\mathrm{Boo}} \sim 3$ days and an amplitude of roughly 1000 μmag (based on a 19 day time series) (Retter et al., 2003). The L/M scaling estimates 2000 μmag.

In both cases the amplitudes observed supports more the L/M scaling (Kjeldsen & Bedding, 1995) (see Eq. 2.1) more than the more optimistic $1/g$ scaling (Kjeldsen & Bedding, 2001), which predicts higher amplitudes for red giants. We note that these stars may have short mode lifetimes and hence show lower amplitudes when observed over a long time span (Stello, 2002). Based on the above arguments the L/M scaling relation has been adopted in the current investigation.

2.3.2 The parameter-independent scaling relation

The stellar parameters (mass and luminosity) of the red stars in the STARE data set are unfortunate not very well known. However, using the parameter-independent scaling relation for solar-like oscillations (Stello, 2002, his Eq. 5.1) enables derivation of amplitude estimates as a function of ν_{max} (the frequency of maximum power). These estimates are independent of the stellar parameters mass and luminosity, using only an estimated temperature range for the stars. Unlike the scaling relation in Stello (2002), which is for equivalent width measurements, the current amplitude estimates should be related to photometry. The derivation of the amplitude scaling is shown in the following.

Since 1 ppm equals 1.086 μmag and $\lambda = 680$ nm for R-band, the L/M scaling by Kjeldsen & Bedding (1995, their Eq. 8) can be written as:

$$(\delta L/L)_{\lambda=680\,\mathrm{nm}} \quad = \quad \frac{(L/\mathrm{L}_\odot)}{(M/\mathrm{M}_\odot)(T_{\mathrm{eff}}/\mathrm{T}_{\mathrm{eff},\odot})^2} \times (4.1 \pm 0.3)\,\mu\mathrm{mag}\ , \tag{2.1}$$

where $\mathrm{T}_{\mathrm{eff},\odot} = 5777$ K. Combining this with the scaling relation for ν_{max} (Brown et al., 1991),

$$\nu_{\mathrm{max}} = \frac{M/\mathrm{M}_\odot}{(R/\mathrm{R}_\odot)^2\sqrt{T_{\mathrm{eff}}/\mathrm{T}_{\mathrm{eff},\odot}}} \times 3.05\,\mathrm{mHz}\,, \tag{2.2}$$

provides the final parameter-independent scaling relation for amplitudes, using $L \propto R^2 T_{\rm eff}^4$:

$$
\begin{aligned}
(\delta L/L)_{\lambda=680\,\rm nm} &= \frac{(R/{\rm R}_\odot)^2 (T_{\rm eff}/{\rm T}_{\rm eff,\odot})^2}{(M/{\rm M}_\odot)} \times (4.1 \pm 0.3)\,\mu{\rm mag} \\
&= \frac{(R/{\rm R}_\odot)^2 (T_{\rm eff}/{\rm T}_{\rm eff,\odot})^{1/2}}{(M/{\rm M}_\odot)\,3050} \times (T_{\rm eff}/{\rm T}_{\rm eff,\odot})^{3/2} \times (12.5 \pm 0.9)\,{\rm mmag} \\
&= (\nu_{\rm max}/\mu{\rm Hz})^{-1} \times (T_{\rm eff}/{\rm T}_{\rm eff,\odot})^{3/2} \times (12.5 \pm 0.9)\,{\rm mmag}\,. \qquad (2.3)
\end{aligned}
$$

There is observational evidence that the uncertainty in frequency (uncertainty in the $\nu_{\rm max}$ estimate) is small (Bedding & Kjeldsen, 2003), and can be neglected compared to the uncertainty in the estimated amplitude at a fixed frequency.

2.3.3 Temperature estimate

In order to estimate the amplitudes of the selected stars their approximate temperature has to be know (Eq. 2.3). Fig. 2.3 shows the $B-V$ colour of the 165 selected low noise stars. A few outliers are not within the plotted range. The median $B-V$ colour is $\mathrm{Med}(B-V) = 1.2$ mag, and most of the stars are within $1.0\,\mathrm{mag} < (B-V) < 1.4\,\mathrm{mag}$. These values are also representative for the entire set of 3347 red stars.

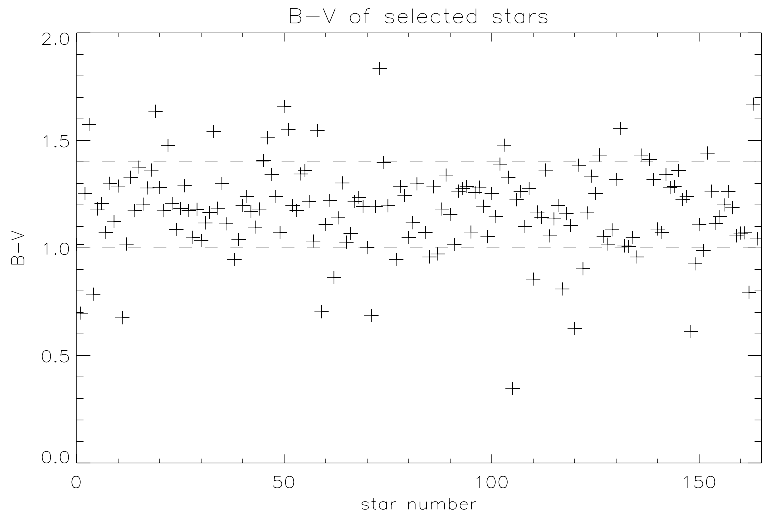

Figure 2.3: $B-V$ colour of the 165 selected low noise stars.

The $B-V$ colour is converted into effective temperature using the BaSeL grid (Lejeune et al., 1998). The effective temperatures were not very sensitive to the chosen metallicity and gravity in the ranges $-0.1 < \mathrm{Fe/H} < 0.1$ (dex), and $1.0 < \log g < 2.5\,(\mathrm{cm/s^2})$. Based on this, a rough estimate of the temperature range is: $4000\,\mathrm{K} < T_{\rm eff} < 5000\,\mathrm{K}$.

2.4 Comparing observations with amplitude estimates

The amplitude estimates (Eq. 2.3) can now be compared to observed amplitude spectra in order to determine if the noise in the observed amplitude spectra are significantly below the estimated amplitudes, which is desired in order to have likely detections of solar-like oscillations in the STARE data sample. Taking into account that the damping times for red giant stars probably are short (Stello, 2002), the criteria used for positive detections of solar-like oscillations to be likely will be that the noise in the spectra are at least a factor of five below the estimated amplitude ($S_{\rm expect}/N_{\rm obs} > 5$) in the frequency range of interest.

2.4.1 ξ Hya as an example

As an example, amplitude spectra of the red giant star ξ Hya are shown together with the estimated amplitudes using scaling relations similar to Eq. 2.3. The spectra are based on radial velocity (with a clear stellar signal) and equivalent width measurements (noise dominated).

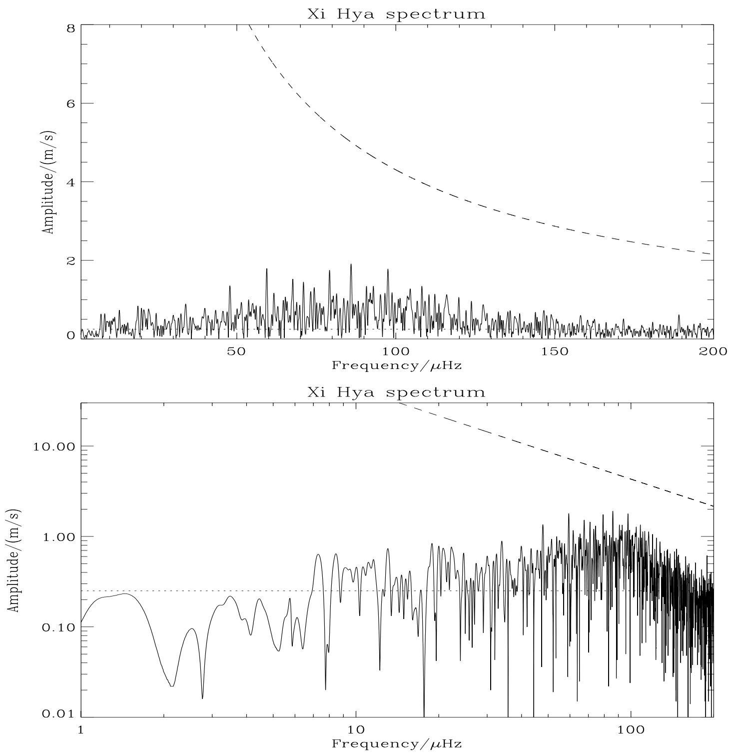

Figure 2.4: Amplitude spectrum of radial velocity measurements of ξ Hya represented on both a linear and logarithmic scale. The time span of the series is 30 days. The dashed line is the estimated amplitude vs. $\nu_{\rm max}$ based on the L/M scaling: $v_{\rm osc} = 1/\nu_{\rm max} \cdot (T/{\rm T}_\odot)^{3.5} \cdot 714\,{\rm m/s}$, $T_{\xi\,\rm Hya} = 5000\,{\rm K}$. The dotted line is the mean level measured in the frequency range 145–185 μHz (white noise).

In Fig. 2.4 the amplitude spectrum (based on a 30 day radial velocity time series) of ξ Hya is shown, both in linear and log-log plot. This figure shows an example of data with noise levels low enough to enable detection of solar-like oscillations. It can be seen that the noise in the spectrum is significantly below the estimated amplitudes as desired (dashed line). This spectrum showed clear evidence of solar-like oscillations, but with an observed amplitude lower than estimated from the L/M scaling (Stello, 2002; Frandsen et al., 2002).

In another attempt to detect oscillations in ξ Hya using the equivalent width technique (Kjeldsen et al., 1995; Stello, 2002), the spectrum looked quite differently due to a high 1/f-noise component, which is also known as drift noise (Stello, 2002). The amplitude spectrum and the estimated amplitudes (using Eq. 5.1 from Stello, 2002, directly) are shown in Fig. 2.5, both in linear and log-log plot. This figure shows an example of data with noise levels which were too high to enable detection of solar-like oscillations. The estimated amplitudes are at the same level as the noise.

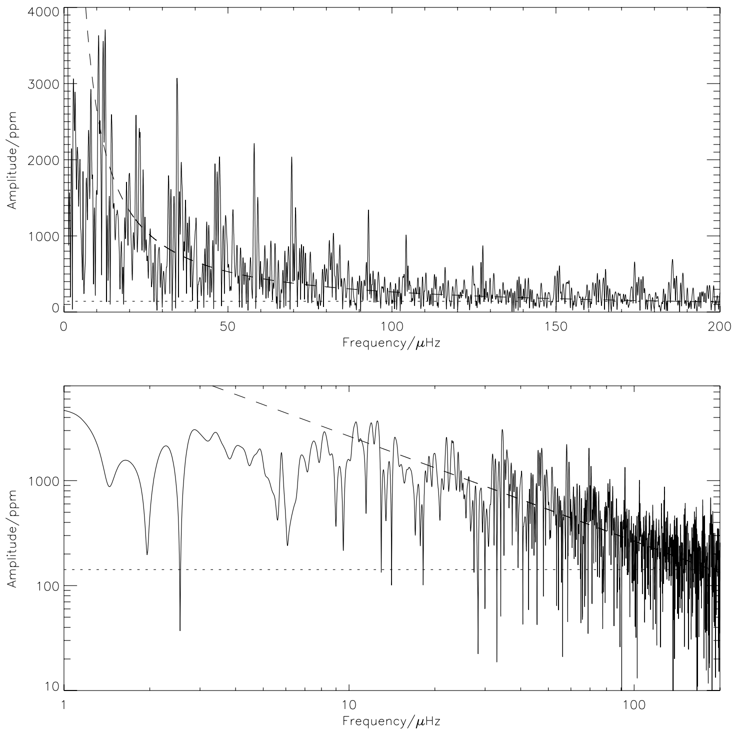

Figure 2.5: Amplitude spectrum of equivalent width measurements of ξ Hya represented on both a linear and logarithmic scale. The time span of the series is 30 days. The dashed line is the estimated amplitude vs. $\nu_{\max}$ based on the L/M scaling in Stello (2002, his Eq. 5.1). The dotted line is the mean level measured in the frequency range 200–300 μHz (white noise).

It was showed by Stello (2002) that the equivalent width measurements did not provide any detection of the oscillations detected in radial velocity, and that these data were highly dominated by an enormous 1/f-noise compared to the actual stellar signal, which was lower than expected (Stello, 2002, his Fig. 5.3).

2.4.2 The low-noise STARE amplitude spectra

In the following a random sample comprised of 10 time series of the 165 selected low noise stars from the STARE data are compared with the estimated amplitudes using Eq. 2.3 (see Fig. 2.6).

To be able to get a reasonable determination of the oscillation frequencies from these stars the periods should not be longer than 5–6 days. Hence the lower boundary of the frequency interval of interest is set to $f_{\rm min} = 2\,\mu$Hz.

In 2 out of the 10 cases shown in Fig. 2.6, the expected amplitude is roughly of the same level as the surrounding noise in the lower end of the relevant frequency interval. At higher frequencies the noise gets significantly larger than the expected amplitude. The other 8 plots show all low frequency noise levels which are higher than the estimated amplitudes.

In 3 cases (ID 772, 1081, 1247) of the 10 spectra shown in Fig. 2.6, the procedure (redpowfind.pro) used by Tim Brown to identify stars which were variables (including bad photometry) did not detect any viability.[1] These 3 cases are in fact those with the lowest noise in the amplitude spectra, both regarding the white noise and the low frequency noise components.

There are 2 stars (ID 277, 717) shown in Fig. 2.6, which where found to be variable (according to redpowfind.pro) with oscillation frequencies larger than $f_{\rm min} = 2\,\mu$Hz.[2] The detected periods and corresponding amplitudes were $\mathrm{P}_{277} \sim 4.94$ days ($\sim 2.34\,\mu$Hz), $\mathrm{Amp}_{277} = 0.025$ mag, and $\mathrm{P}_{717} \sim 4.83$ days ($\sim 2.40\,\mu$Hz), $\mathrm{Amp}_{717} = 0.016$ mag. This should be compared to the estimated amplitude for this frequency range which is 0.003–0.004 mag in the relevant temperature range (4000K–5000K) (see Eq. 2.3).

In Fig. 2.7 the amplitude spectra of all 165 low noise stars has been averaged for each frequency in order to remove particularities from the individual spectra. This is to reveal better the overall and general trends in these spectra. The amplitude estimates are indicated. It can be seen that the criteria $S_{\rm expect}/N_{\rm obs} > 5$ is not fulfilled even if only the white noise is taken into account ($S_{\rm expect}/N_{\rm white} < 3.25$), and seen from the plotted spectra (Figs. 2.6, 2.7) the low frequency noise can definitely not be neglected, since it is the dominating noise component in the relevant frequency interval.

The median spectrum show the same features as the mean spectrum but is lowered by 25% in amplitude relative to the averaged spectrum.

[1] There were 54 stars in the entire set of 165 low noise stars which where not found to be variable by redpowfind.pro.

[2] There were 21 stars in the entire set of 165 low noise stars which where found to be variable, by redpowfind.pro, with oscillation frequencies larger than $f_{\rm min} = 2\,\mu$Hz.

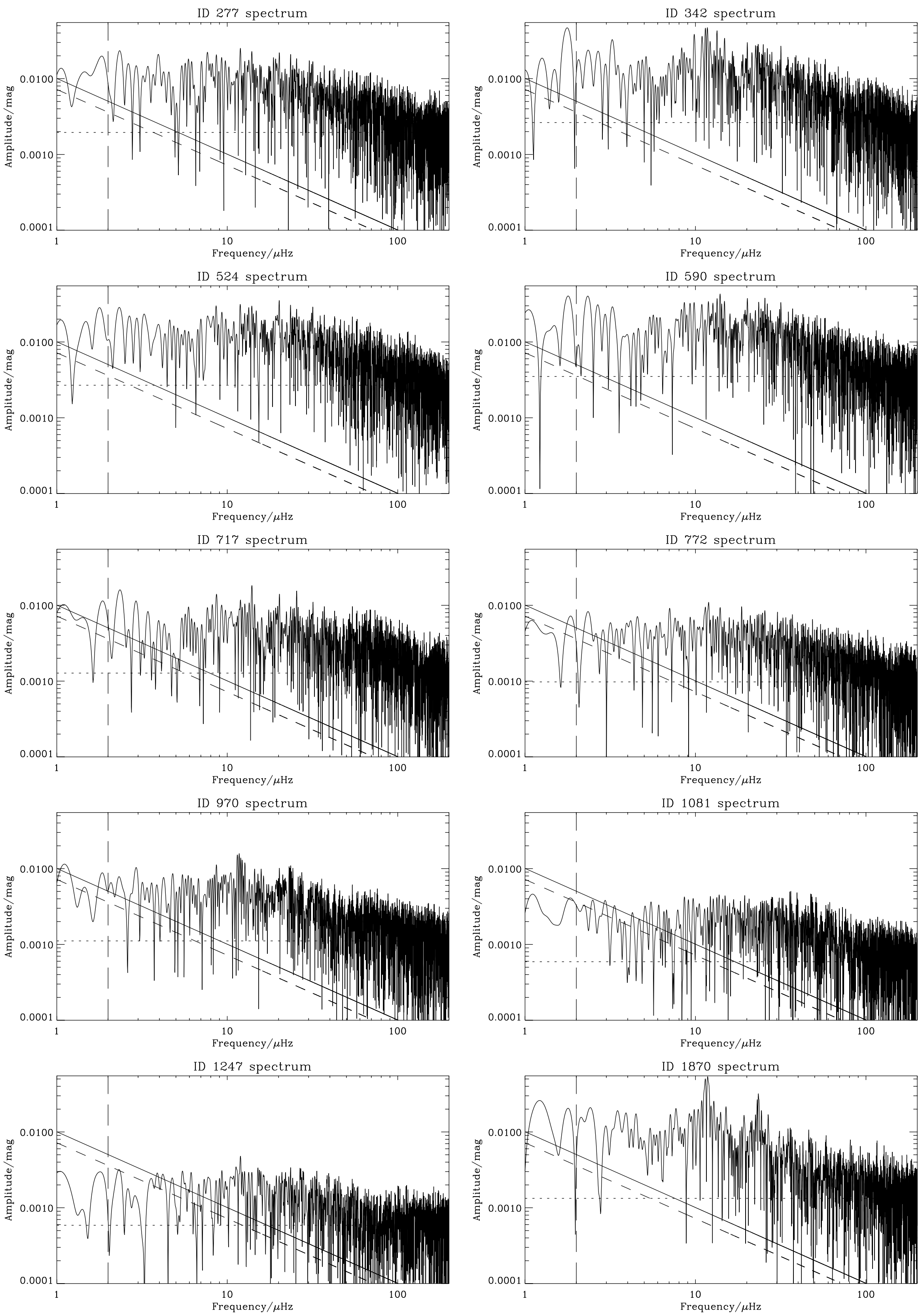

Figure 2.6: Randomly chosen amplitude spectra from the sample of 165 low noise stars in the STARE data set of red stars. The dotted line is the mean level measured in the frequency range 200–300 μHz (white noise). The sloping solid line is the amplitude estimate for the hot end of the selected stars ($T_{\rm eff} = 5000$ K), while the dashed line is the estimate for the cool end ($T_{\rm eff} = 4000$ K). The amplitude spectra are derived using weighted data: $data \times (1/err^2)$. The long dashed vertical line indicates the lower boundary of the frequency range of interest $f_{\rm min} = 2\,\mu$Hz.

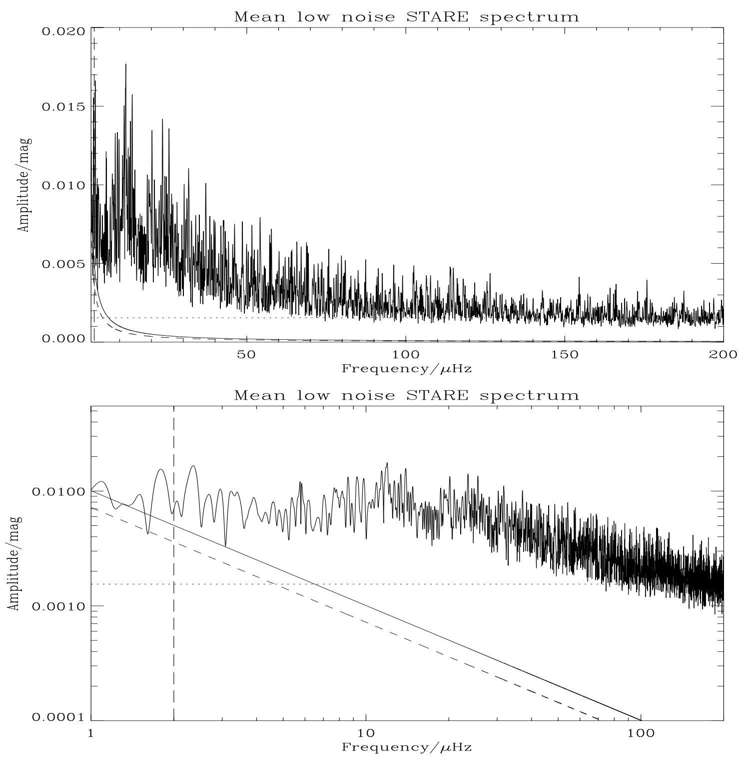

Figure 2.7: The mean spectrum of all 165 low noise stars in the STARE data set of red stars. The dotted line is the mean level measured in the frequency range 200–300 μHz (white noise). The sloping solid line is the amplitude estimate for the hot end of the selected stars ($T_{\rm eff} = 5000\,$K), while the dashed line is the estimate for the cool end ($T_{\rm eff} = 4000\,$K). The amplitude spectra are derived using weighted data: $data \times (1/err^2)$. The long dashed vertical line indicates the lower boundary of the frequency range of interest $f_{\rm min} = 2\,\mu$Hz.

2.5 Discussion

When drawing a conclusion on the above comparison of the STARE low noise amplitude spectra and the estimated amplitudes it should also be kept in mind that the time series are long compared to the expected damping times for red giant stars (Stello, 2002; Houdek & Gough, 2002). Hence it should not be expected that the amplitudes, measured from the amplitude spectra based on the entire time series, would be as high as predicted by the scaling relation (Eq. 2.3). This of course makes it less likely that the STARE data will be suitable for investigations of solar-like oscillations for stars with periods of maximum 5 days.

Since the selected stars are those with the best noise statistics it is not likely that other samples of the 3347 red stars in total would be more likely to show solar-like oscillations. One may argue that solar-like oscillations are more likely to be present (physically) in the fainter stars, but these would also have more noisy amplitude spectra, and hence more unlikely to be detected even if present.

2.5.1 Tim Brown's amplitude-period relation

The final question is though, what can be concluded from the amplitude vs. period diagram shown by Tim Brown, which indicates an amplitude-period relation (Brown priv. comm., 2003).

The amplitude vs. period diagram has been replotted using frequency instead of period to be consistent in the current report. Both the amplitude vs. frequency diagram for all the stars found to show variability by redpowfind.pro, and that of the smaller sample selected by Tim Brown as being really variables (using the criteria $\mathrm{amp}_{\mathrm{maxpeak}} > 0.8 \times \mathrm{rms}$, where rms is the standard deviation of the time series of each star) has been plotted in Fig. 2.8. The fairly broad scatter in amplitude shown

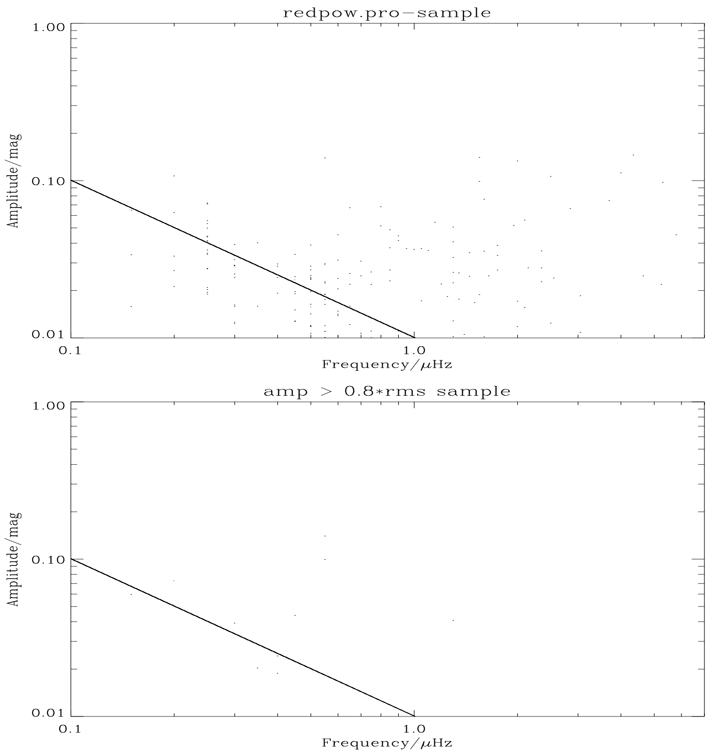

Figure 2.8: (Top) Amplitude vs. frequency for all stars detected by redpowfind.pro. (Bottom) Amplitude vs. frequency for stars which fulfill the criteria $\mathrm{amp}_{\mathrm{maxpeak}} > 0.8 \times \mathrm{rms}$, where rms is the standard deviation of the time series of each star. The solid line is the estimated amplitudes for the hot end of the stars ($T_{\mathrm{eff}} = 5000\,\mathrm{K}$).

in the top panel of Fig. 2.8 probably resembles the noise variation in the 3347 spectra of red stars. The frequency sampling is $0.05\,\mu\mathrm{Hz}$ which is the reason for the vertical bar structure in both plots for the entire plotted frequency range.

Based on the comparison of the estimated amplitudes and the amplitudes found by redpowfind.pro for the peaks at frequencies larger than $f_{\mathrm{min}} = 2\,\mu\mathrm{Hz}$ (and probably down to $f = 1\,\mu\mathrm{Hz}$), it is concluded that these peaks must be noise peaks.

The bottom panel of Fig. 2.8 is equivalent to the amplitude-period plot shown by Tim Brown. Due to the limited frequency resolution ($1/T_{\rm obs} = 0.2\,\mu$Hz) it is not really possible to say if the data points show an amplitude-frequency relation which is due to stellar oscillations, and it can not be excluded that the slow rise of the mean amplitude in each frequency bin for decreasing frequency is due to 1/f-noise.

2.5.2 Conclusions

One can of course hope that some of the observed stars in the STARE sample actually oscillates with a larger amplitude than estimated by Eq. 2.3, even though the time span of the time series is long compared to the expected damping times. Although it is not shown to be impossible, the conclusion is that it is certainly not likely that the STARE data will reveal solar-like oscillations in the sample of red stars.

Chapter 3

Simulating solar-like oscillations

The content of this chapter was published in a special issue of Solar Physics in 2004 by Dennis Stello in collaboration with Hans Kjeldsen, Tim Bedding, Joris De Ridder, Conny Aerts, Fabien Carrier and Søren Frandsen (Stello et al., SolPhys, 220, 207). I generated and analysed the data and developed the method for comparing the simulations with observations. I was supervised by Tim Bedding and Hans Kjeldsen.

3.1 Abstract

The discovery of solar-like oscillations in the giant star ξ Hya (G7III) was reported by Frandsen et al. (2002). Their frequency analysis was very limited due to alias problems in the data set (caused by single-site observations). The extent to which the aliasing affected their analysis was unclear due to the unknown damping time of the stellar oscillation modes. In this paper we describe a simulator created to generate time series of stochastically excited oscillations, which takes as input an arbitrary window function and includes both white and non-white noise. We also outline a new method to compare a large number of simulated time series with an observed time series to determine the damping time, amplitude, and limited information on the degree of the stochastically excited modes. For ξ Hya we find the most likely amplitude to be ~ 2 m/s, in good agreement with theory (Houdek & Gough, 2002), and the most likely damping time to be ~ 2 days, which is much shorter than the theoretical value of 15–20 days calculated by Houdek & Gough (2002).

3.2 Introduction

The recent detection of solar-like oscillations in the G7 giant star ξ Hya (Stello, 2002; Frandsen et al., 2002) promises new interesting prospects for asteroseismology in this part of the Hertzsprung-Russell diagram. The amplitude spectrum of ξ Hya, based on a one-month time series measured in velocity, showed a clear excess of power within a broad frequency envelope, similar to that seen in the Sun and other solar-type stars (Bedding & Kjeldsen, 2003). The envelope was centered at $\sim 90\,\mu$Hz, as expected from scaling the acoustic cut-off frequency of the Sun (Brown et al., 1991). The highest peak in the amplitude spectrum was ~ 1.9 m/s.

Following these observational results, Houdek & Gough (2002) calculated the theoretical damping rate, η, and amplitude for ξ Hya. The amplitude was ~ 2 m/s and, based on η, we calculated the damping time (or mode lifetime) as $1/(2\pi\eta) \sim 15$–20 days.

The autocorrelation function of the amplitude spectrum of ξ Hya revealed a characteristic frequency separation of $6.8\,\mu$Hz, in good agreement with the expected large frequency separation of the radial modes (i.e. $l = 0$) (Stello, 2002; Frandsen et al., 2002). However, using the frequencies extracted from the observed amplitude spectrum, Stello (2002) showed that a unique solution for the large frequency separation could not be found, due to aliasing. It seemed most likely, however, that the correct value was indeed in the range 6.8–7.0 μHz. The observed frequencies could be explained by purely radial modes, but the presence of non-radial modes could not be excluded, again due to aliasing (Stello, 2002; Frandsen et al., 2002).

Based on a small sample of simulated time series, Stello (2002) showed that the significance of the observed frequencies, due to the effect from aliasing, was strongly dependent on the mode damping time adopted for ξ Hya. Hence, in order to quantify the alias problems, the damping time for ξ Hya has to be known. However, as pointed out by Stello (2002), the damping time of ξ Hya could not be measured directly from the observed amplitude spectrum (by fitting Lorentzian profiles) because the power spectrum was too crowded. Neither was it possible to use the CLEANed spectrum to measure the damping time directly, since the number of frequencies and their position in the spectrum are not known. Therefore, extensive simulations would be needed to estimate the damping time. Furthermore, it should be noted that the preliminary simulations performed by Stello (2002) indicated that the damping time could be significantly shorter than predicted by theory (Houdek & Gough, 2002). It is therefore important to establish a more precise determination of the damping time from the observations than was done by Stello (2002).

In this paper we describe a time-series simulator, outlining the theoretical background and the technique used to simulate stochastically excited oscillations. We use this simulator to determine the damping time of ξ Hya using a new method, which is based on comparing the overall structure of the observed amplitude spectrum with a large sample of simulations. The method also gives the amplitude and some limited information about the mode degree of the oscillations.

The outline of the paper is as follows: Section 3.3 introduces the fundamental ideas used for simulating the stellar signal from stochastic pulsations, and describes the parameters that the simulator needs as input. Section 3.4 describes how the simulated time series of ξ Hya were constructed and outlines how we decided the input parameters. Based on a few results of the simulated data, we introduce in Sect. 3.5 the method used to determine the damping time of ξ Hya and present an optimum fit to the observations. Finally, we discuss the method and our results in Sect. 3.6, which also includes the conclusions.

3.3 Simulator

The simulator described in this paper uses the same fundamental ideas (also described by Chang & Gough (1998)) as the light curve simulator developed for the MONS and Eddington missions (Kjeldsen & Bedding, 1998; De Ridder, 2002; De Ridder et al., 2004).

3.3.1 Stochastic excitation model

The stellar signal, S, as a function of time, t, is modeled by

$$S(t) = \sum_{\nu=\nu_1}^{\nu_n} s_\nu(t)\,, \tag{3.1}$$

where each $s_\nu(t)$ is a continuously re-excited damped harmonic oscillator that represents a single oscillation mode.

In general, a damped harmonic oscillator without re-excitation can be expressed as

$$s_\nu(t) = A\sin(2\pi\nu t + \phi)e^{-t/d}\,, \tag{3.2}$$

where A, ν, ϕ, and d are the amplitude, frequency, phase, and damping time. Rather than assigning a constant amplitude to each oscillator, as in Eq. 3.2, we instead simulate the re-excitation and damping as a 'kicking' and damping of the amplitude A. The amplitude of each mode is kicked independently at a rate characterised by the small time step, Δt_{kick}, between each kick. The independence of the re-excitation is established by having different phases, chosen at random, for each mode, so that the time for each kick would not be simultaneous for the different modes. After n kicks the amplitude, A, assigned to a mode is

$$A_n = e^{-\Delta t_{\text{kick}}/d} A_{n-1} + \varepsilon_n \,, \tag{3.3}$$

where $e^{-\Delta t_{\text{kick}}/d}$ is the damping factor and ε_n is the nth re-excitation kick, taken at random from a Gaussian distribution with zero mean and standard deviation σ_ε. In order to vary both amplitude and phase in time, we generate the time series as the sum of sine and cosine terms (using $A\sin(x+\pi/4) = A/\sqrt{2}\,(\sin(x)+\cos(x))$), which are simulated independently. Hence the expression for $s_\nu(t)$ used in this simulator is

$$s_\nu(t) = A_{n,1}\sin(2\pi\nu t + \phi_{\nu,1}) + A_{n,2}\cos(2\pi\nu t + \phi_{\nu,2})\,. \tag{3.4}$$

The autoregressive process shown in Eq. 3.3 is asymptotically stable up to second order (i.e. it does not die out or 'explode' as $n \to \infty$), provided $|e^{-\Delta t_{\text{kick}}/d}| < 1$, which is always true for physically meaningful values (i.e. $\Delta t_{\text{kick}} > 0$ and $d > 0$) (Priestley, 1981). In the asymptotic limit, when the process has relaxed, the mean is $\langle A_n \rangle = 0$, and the variance, $\sigma^2_{A_n}$, can be expressed in terms of σ_ε as

$$\sigma^2_{A_n} \simeq \frac{\sigma^2_\varepsilon}{1 - e^{-2\Delta t_{\text{kick}}/d}}\,. \tag{3.5}$$

Using the amplitude-scaled discrete version of Parseval's theorem (see Kjeldsen & Frandsen, 1992) we have for each term in Eq. 3.4

$$\begin{aligned} P(\nu) &= 2\frac{1}{N}\sum_{n=1}^{N}|s_\nu(t_n)|^2 \\ &= 2\frac{1}{N}\sum_{n=1}^{N}|A_n|^2|\sin(2\pi\nu t_n + \phi_\nu)|^2 \\ &\simeq \frac{1}{N}\sum_{n=1}^{N}|A_n|^2 \\ &= \sigma^2_{A_n} \end{aligned} \tag{3.6}$$

for a large number of measurements, N, where $P(\nu)$ is the power at frequency ν in the power spectrum.

Finally, combining Eq. 3.6 with Eq. 3.5 gives the value of σ_ε required to simulate a continuously re-excited damped harmonic oscillator, as shown in Eq. 3.4, that has an average power $P(\nu) = A(\nu)^2$ in the power spectrum. The resulting expression for σ_ε is

$$\sigma_\varepsilon = A\sqrt{\Delta t_{\text{kick}}/d}\,, \tag{3.7}$$

where the first-order approximation of e^x has been used (which assumes $\Delta t_{\text{kick}} \ll d$). We obtained Eq. 3.7 by dividing σ_ε by $\sqrt{2}$ to produce the correct standard deviation of the resulting amplitude for the combined sine and cosine term (see Eq. 3.4).

We repeat the autoregressive process (Eq. 3.3) for a number of steps that is significantly longer than the characteristic relaxation time, to let it stabilise before the actual simulations of the stellar signal begin. As a rule of thumb, the minimum number of initial steps of the autoregressive process (before starting the actual simulations) should correspond to at least twice the damping time.

The simulated signal for each harmonic oscillator described above, $s_\nu(t)$ (Eq. 3.4), may be viewed as the sum of two vectors in the complex plane. The main vector with length (amplitude) A is anchored at the origin, cycling around it at the frequency of the oscillation. The excitation vector, with variable length, is anchored at the tip of the main vector. Its variable direction relative to the main vector can be separated into the two orthogonal components: phase (orthogonal to the main vector) and amplitude (parallel to the main vector). An example of such a stochastically excited oscillation at a single frequency is shown in Fig. 3.1. These simulations looks similar to observations of the Sun (Leifsen et al., 2001), which supports the theory of continuous excitation by convective elements (Goldreich & Keeley, 1977; Houdek et al., 1999).

3.3.2 Amplitude interpolation

The algorithm described in Sect. 3.3.1 calculates the amplitude (Eq. 3.3) at regular time steps, but these do not necessarily coincide exactly with the times of the observations. Since the amplitude varies slowly, we simply use the value closest in time to each actual observation. The sinusoidal oscillation itself (Eq. 3.4), on the other hand, is evaluated at the exact times of the observations. The result is a fast and reliable method for simulating stochastic excited oscillations with an arbitrary observational window function.

3.3.3 Noise calculation

To make realistic simulations of stochastically excited oscillations, it is very important to be able to include noise (Kjeldsen, 2003). In our simulator both white noise and non-white noise are included.

The white noise is generated by a Gaussian random-number generator. For each data point, the white noise is divided by the weight factor associated with that data point before it is added to the oscillation signal.

The non-white noise is created by first calculating the Fourier spectrum of a white noise source generated by a random generator. Then we multiply it by a function that describes the desired profile of the non-white noise. The result is then

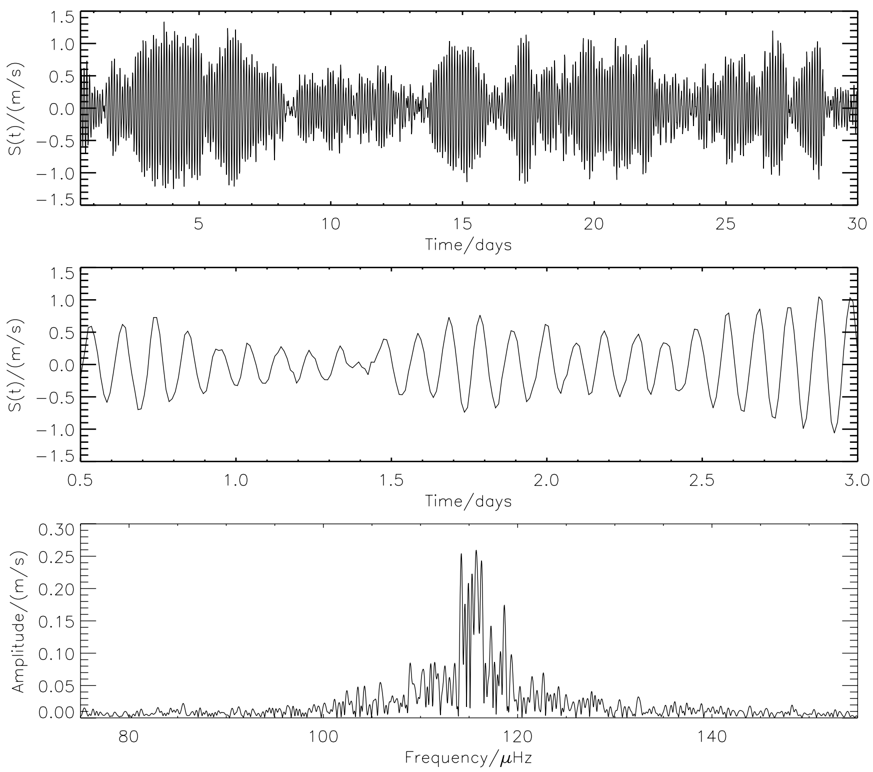

Figure 3.1: Simulated noise-free time series of a stochastically excited and continuously damped oscillation at a single frequency (Eq. 3.4). The input parameters are: $d = 1.6$ days, $\nu = 115.7\,\mu$Hz, $A = 0.71$ m/s, and $\Delta t_{\rm kick} = 2$ min. Top panel: Time series of 3000 data points sampled at 14.4 min. Middle panel: Close-up of the upper panel. Bottom panel: Amplitude spectrum of the time series.

converted back to the time domain, producing the time series of the non-white noise source, which finally is added to the oscillation signal.

3.3.4 Input parameters

To summarise, the following input parameters have to be supplied to the simulator:

1. A set of frequencies.
2. The amplitude corresponding to each frequency.
3. The damping time corresponding to each frequency.
4. The time of each observation (the observational window).
5. The weight of each observation.
6. A set of parameters defining the noise levels according to the chosen noise function.
7. The time step between each re-excitation kick $\Delta t_{\rm kick}$.

3.4 Simulating time series of ξ Hya

We used the simulator described in Sect. 3.3 to generate a large number of time series similar to that obtained for ξ Hya by Frandsen et al. (2002). The input parameters for the simulator were as follows:

1. Since the observations can be explained as purely radial modes (Stello, 2002; Frandsen et al., 2002), this simple case has been chosen for the main part of the current investigation. The input frequencies, $\nu_1, \ldots, \nu_n$, were the radial modes from a pulsation model (Stello, 2002), rescaled so that the mean frequency separation was $6.8\,\mu$Hz, in agreement with the observations (Stello, 2002; Frandsen et al., 2002).

2. The relative amplitude of each mode was defined according to an envelope (see Fig. 3.2, solid vertical lines). The envelope was obtained by smoothing the observed amplitude spectrum, subtracting the noise background and normalising the peak to unity. In order to match simulations with observations the width of the envelope was made adjustable. We chose to do this by raising the curve to the xth power, where x was a free parameter, which was a convenient way of changing the width of the envelope without changing the height. The envelope was then scaled vertically by a factor $\mathrm{Amp_{scale}}$, which was a free parameter that represents the oscillation amplitude of ξ Hya. Figure. 3.2 (dashed curve) shows the normalised envelope for $x = 2$ and $\mathrm{Amp_{scale}} = 1\,$m/s.

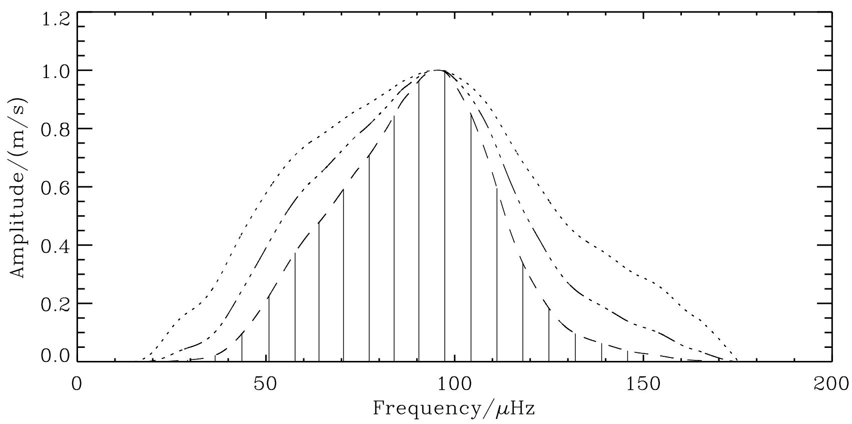

Figure 3.2: Three amplitude envelopes: dashed curve: $x = 2$ ($\mathrm{FWHM_{in}} = 48.0\,\mu$Hz); dashed-dot-dot-dot curve: $x = 1.2$ ($\mathrm{FWHM_{in}} = 64.0\,\mu$Hz); dotted curve: $x = 0.7$ ($\mathrm{FWHM_{in}} = 81.6\,\mu$Hz). The vertical solid lines indicate the mode frequencies.

3. The damping time, d, was a free parameter and was the same for all modes. This is probably a reasonable approximation, since the theoretical damping rate shows a flat plateau covering a fairly broad range of frequencies ($\sim$ 70–130 μHz) (Houdek & Gough, 2002).

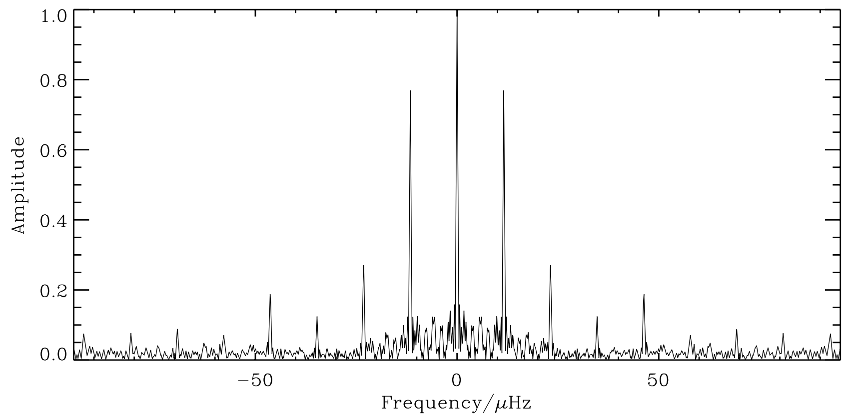

Figure 3.3: Spectral window of the ξ Hya time series.

4. The observational window function was exactly the same as for the actual observations (Stello, 2002; Frandsen et al., 2002). The amplitude spectrum of the observational window (the spectral window) is shown in Fig. 3.3.

5. The weight of each observation was $1/\sigma_i^2$, where σ_i was the noise associated with each observed data point.

6. The noise was the sum of a white and a non-white noise component, where the latter was described by a linear model. The noise was therefore specified by three parameters: the white noise level ($\mathrm{Noise_{white}}$), the slope of the non-white noise ($\mathrm{Noise_{slope}}$), and a scaling of the non-white noise ($\mathrm{Noise_{scale}}$).

7. The time step Δt_{kick} was set to 2 min to meet the requirement that $\Delta t_{\mathrm{kick}} \ll d$ for all damping times tested in this investigation.

Before starting the actual simulations, we repeated the autoregressive process (Eq. 3.3) for 120000 steps, corresponding to 167 days, which is significantly longer than the characteristic relaxation time for all the damping times tested in this investigation, to ensure it had stabilised.

3.5 Method and results

Examples of simulated amplitude spectra with different damping times are shown in Fig. 3.4.

We determined how well the simulated time series reproduced the observations by using eight measurable parameters that characterised different features of the amplitude spectra. It is clear that amplitude spectra based on a short damping time have much more densely packed peaks (top panel) than do those with long damping times (bottom panel). This arises because the continuous re-excitation of

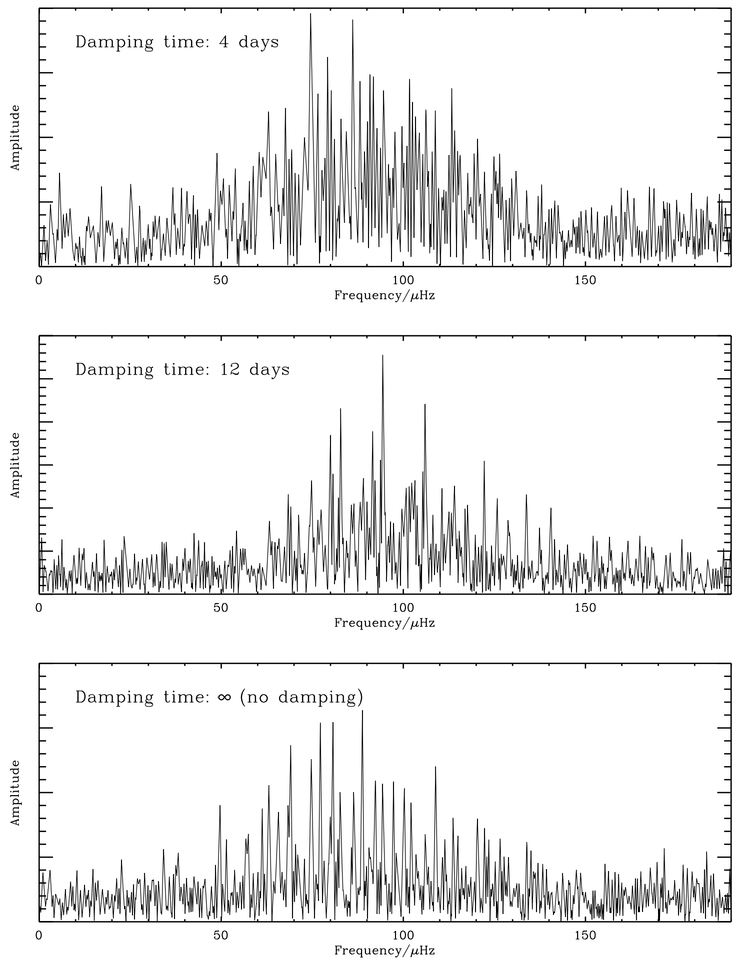

Figure 3.4: Amplitude spectra based on simulated time series. The input damping times for the time series are shown in each panel. For infinite damping time (bottom panel) the input amplitudes were randomised.

modes introduces slight shifts in the phase as a function of time, which shows up in the amplitude spectrum as extra peaks slightly offset in frequency. The fact that amplitude spectra based on different damping times display such different characteristics, as seen in Fig. 3.4, suggests the possibility of measuring the mode damping time from the overall structure of the amplitude spectrum.

In Fig. 3.5 we show the observed amplitude spectrum of ξ Hya, together with the measurable parameters that specify different characteristics of the amplitude spectrum.

The highest peak ($\mathrm{Max_{peak}}$) is the highest amplitude found in the spectrum, while $\mathrm{Max_{smooth}}$ is the height of the smoothed amplitude spectrum, where smoothing was done twice with a boxcar filter. The widths of the boxcars were $20\,\mu$Hz followed by $5\,\mu$Hz. The two noise levels, $\mathrm{Noise_{low}}$ and $\mathrm{Noise_{high}}$ are measured as the mean

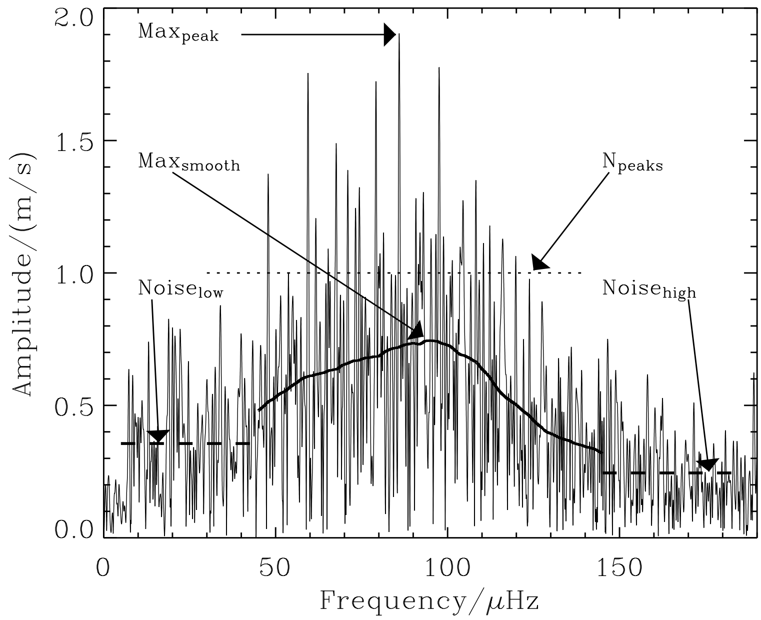

Figure 3.5: Amplitude spectrum (observed) of ξ Hya. Different parameters characterising the spectrum are indicated (see text page 37).

amplitude in the frequency ranges 5–45 μHz and 145–185 μHz, respectively. The number of detected peaks with amplitudes above a threshold of 1.0 m/s (S/N$\geq$ 3.5), denoted $N_{\rm peaks}$, is found by CLEANing the amplitude spectrum until the amplitude threshold has been reached. Our CLEAN process subtracts one frequency at a time (the one with the highest amplitude), but recalculates the amplitude, phase and frequencies of the previously subtracted peaks while fixing the frequency of the latest extracted peak. In this way, the fit of sinusoids to the time series is done simultaneously for all peaks. The mean amplitude is measured both over the entire frequency range 0–190 μHz ($\rm Amp_{tot}$) and in the central part that is dominated by the stellar excess of power, 40–140 μHz ($\rm Amp_{cen}$). Finally, the width of the excess power ($\rm W_{env}$) is measured as the FWHM of the smoothed spectrum after the noise has been subtracted. Due to the window function, stellar excess power 'leaks' into the frequency regions where we measure the noise. The subtraction of noise in the determination of the envelope width therefore includes some stellar power, making $\rm W_{env}$ smaller than the input widths (Fig. 3.2), which therefore should not be compared.

We now describe how the eight parameters measured from the simulated amplitude spectra ($\rm Max_{peak}$, $\rm Max_{smooth}$, $\rm Noise_{low}$, $\rm Noise_{high}$, $\rm N_{peaks}$, $\rm Amp_{cen}$, $\rm Amp_{tot}$, $\rm W_{env}$) are affected by changes in the input parameters, namely damping time (d), noise ($\rm Noise_{white}$, $\rm Noise_{slope}$, $\rm Noise_{scale}$), amplitude ($\rm Amp_{scale}$), envelope width (determined by the exponent x), and input frequencies ($\nu_1, \ldots, \nu_n$).

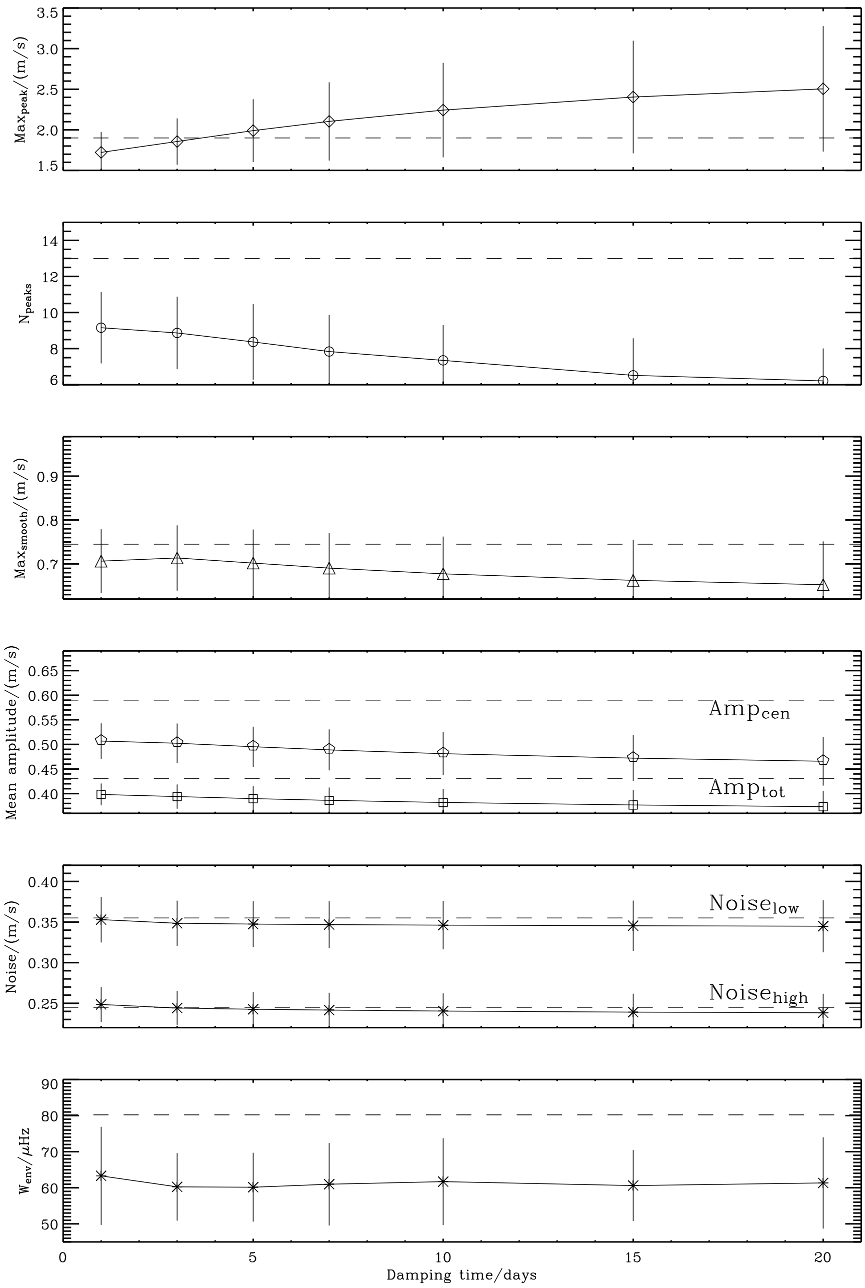

Figure 3.6: The eight measured parameters as a function of the damping time. The data points are based on 7 distinct sets of simulated spectra only differing in their damping time. Each set comprised 100 independent simulated time series. Each plotted point is the mean of the values found from the 100 simulations within each set, and the vertical bars indicate the rms scatter that results from the stochastic nature of the simulation. The points are connected by solid lines to guide the eye. The *dashed lines* denote the values measured from the observations. The common input parameters for the 7 sets are: $\mathrm{Amp_{scale}} = 2.1\,\mathrm{m/s}$, $x = 2.0$ ($\mathrm{FWHM_{in}} = 48.0\,\mu\mathrm{Hz}$), $\mathrm{Noise_{white}} = 0.20\,\mathrm{m/s}$, $\mathrm{Noise_{slope}} = 1.5$, $\mathrm{Noise_{scale}} = 3.0$, and 18 input frequencies with a mean frequency separation of $6.8\,\mu\mathrm{Hz}$.

3.5.1 Damping time

Figure 3.6 shows the dependence of each of the eight measured parameters on the damping time. Values adopted for the other input parameters are given in the figure caption. Each plotted point is the mean of 100 simulations with the same input parameters but different random number seeds, and the vertical bars show the rms scatter over these 100 simulations. This rms is the intrinsic scatter due to the stochastic nature of the oscillations, and is therefore the quantity we should use to decide whether the simulations match the observations. The parameters measured from the observed amplitude spectrum are indicated by horizontal dashed lines.

All the parameters increase as the damping time gets shorter except for $\mathrm{Max}_{\mathrm{peak}}$, which falls off. The fall in $\mathrm{Max}_{\mathrm{peak}}$ is simply because the re-excitation spreads the power over more peaks, giving less power in each. The relative change in most of the parameters over the range of damping times plotted in Fig. 3.6 is fairly small ($\lesssim 10\%$) and is generally less than the rms scatter. These parameters are therefore not very sensitive measures of the damping time but should still be matched with the observed values to constrain the other input parameters. However, $\mathrm{Max}_{\mathrm{peak}}$ and $\mathrm{N}_{\mathrm{peaks}}$ change by roughly 50% in the same range and in opposite directions, making them the obvious parameters of choice for constraining the mode damping time. The correlation coefficient between $\mathrm{Max}_{\mathrm{peak}}$ and $\mathrm{N}_{\mathrm{peaks}}$ is only $\rho \sim 0.10$–0.15, based on a few sets of 100 simulated amplitude spectra, where each set had different input parameters. These two parameters can therefore be regarded as uncorrelated.

The 2nd, 3rd, and 4th panels in Fig. 3.6 all indicate that, for all damping times, the amount of power in these simulations is too low. The bottom panel shows that this is partly because the width is too narrow. The input power can be adjusted by changing the input noise, amplitude, envelope width, and the number of frequencies (their mean separation). We address each of these possibilities in turn in the next sections.

3.5.2 Noise

We investigated how the measured parameters changed as a function of input noise. We only show the results of changes in $\mathrm{Noise}_{\mathrm{white}}$ because this parameter gave us all the control we needed to adjust the simulations to match the noise level in the observations. The two other noise parameters were fixed at the values used for Fig. 3.6.

Figure 3.7 shows that the parameters most sensitive to changes in the input noise are $\mathrm{Noise}_{\mathrm{low}}$ and $\mathrm{Noise}_{\mathrm{high}}$, while the other parameters show much smaller changes. The input noise can therefore be regarded as the final fine tuning parameter, and has less importance for constraining the other input parameters. The panel showing the measured noise will therefore be omitted in the following plots.

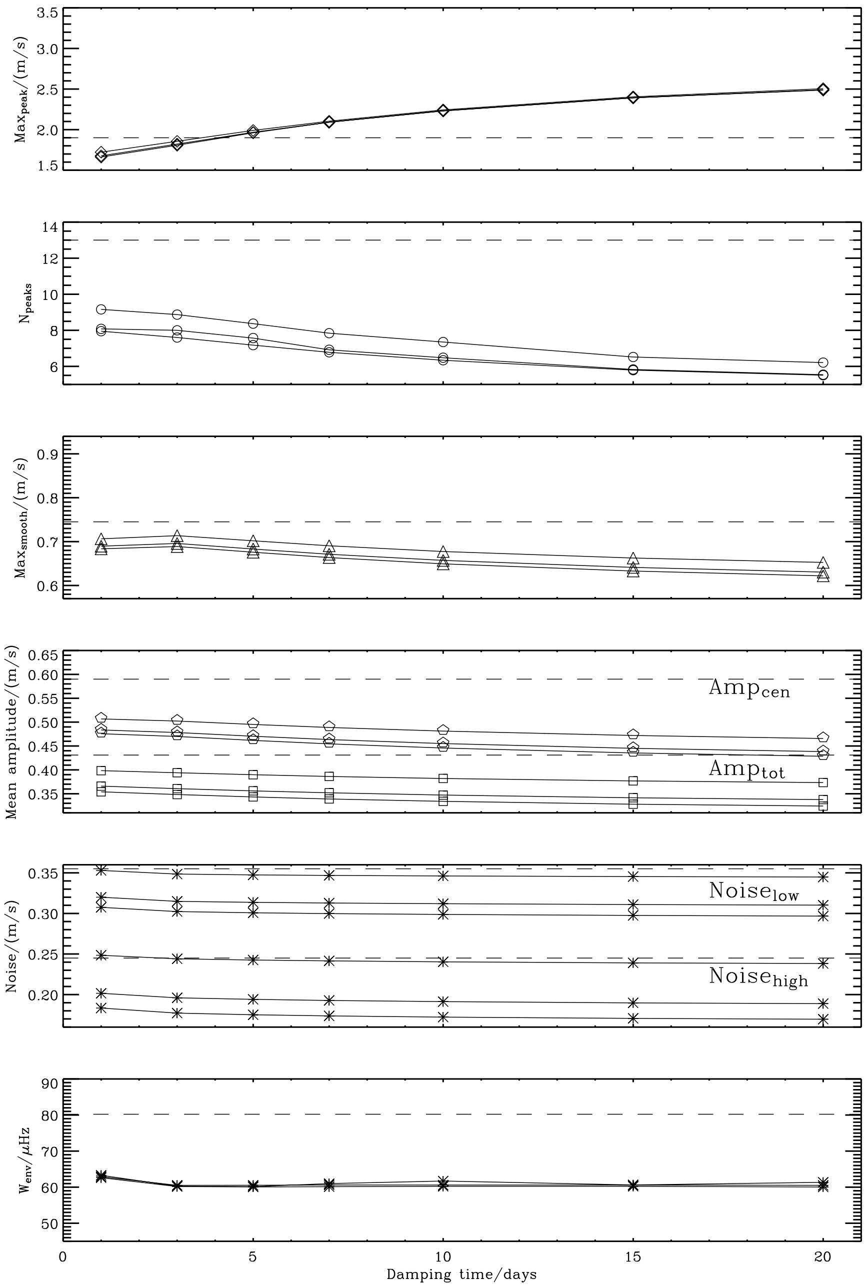

Figure 3.7: The effect of changing the white noise. These panels are similar to those plotted in Fig. 3.6, but for three different values of the white noise. Each measured parameter is therefore shown as three points for every damping time. The values for input noise (from top to bottom in each panel) are: $\text{Noise}_{\text{white}} = 0.2\,\text{m/s}$ (as in Fig. 3.6), $\text{Noise}_{\text{white}} = 0.1\,\text{m/s}$, and $\text{Noise}_{\text{white}} = 0.0\,\text{m/s}$. All parameters show a decrease as $\text{Noise}_{\text{white}}$ decreases. Note that the y-axis has been shifted, but not scaled, relative to Fig. 3.6. For clarity, the vertical bars indicating rms scatter have been omitted.

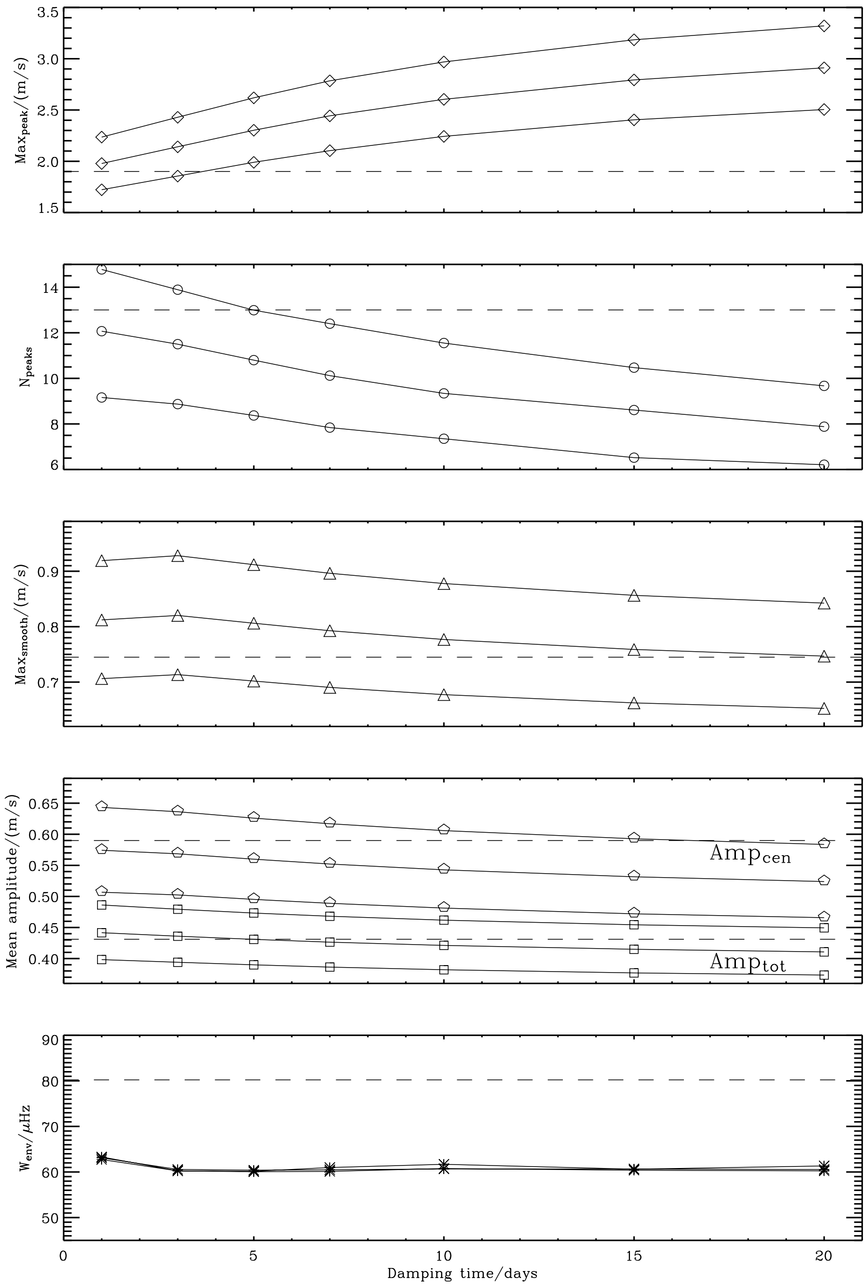

Figure 3.8: The effect of changing the input amplitude. These panels are similar to those plotted in Fig. 3.6, but for three different values of input amplitude. Each measured parameter is therefore shown as three points for every damping time. The input amplitudes (from bottom to top in each panel) are: $\mathrm{Amp_{scale}} = 2.1\,\mathrm{m/s}$ (as in Fig. 3.6), $\mathrm{Amp_{scale}} = 2.5\,\mathrm{m/s}$, and $\mathrm{Amp_{scale}} = 2.8\,\mathrm{m/s}$. All parameters show an increase as $\mathrm{Amp_{scale}}$ increases.

3.5.3 Amplitude

In Fig. 3.8 we show the dependence of the measured parameters on the input amplitude. It can be seen that all parameters show an increase with input amplitudes, which is expected due to the increase in power, although the change is very small for $\mathrm{W_{env}}$.

It is clear from Fig. 3.8 that the input amplitude is constrained by $\mathrm{Max_{peak}}$, which should not be too high, and by $\mathrm{N_{peaks}}$, which should not be too low. The difficulty in satisfying both constraints simultaneously becomes greater for larger values of the damping time.

3.5.4 Envelope width

Another way of injecting more power into the simulations, enabling more peaks to be detected without having $\mathrm{Max_{peak}}$ increase significantly, is by making the envelope wider (see Fig. 3.2). Figure 3.9 shows the dependence of the measured parameters on the envelope width. As expected, an increase in envelope width gives rise to an increase in all parameters, due to the power increase. $\mathrm{Max_{peak}}$ is, however, nearly unaffected. Thus, by increasing the width we construct simulations from which more peaks are detected ($\mathrm{N_{peaks}}$ increases), without affecting $\mathrm{Max_{peak}}$, hence making the simulations better fit the observations, which is also supported by the bottom panel. Since the input width is the only input parameter to induce significant changes in $\mathrm{W_{env}}$, we see from the bottom panel that the input width can be fixed at a value around $80\,\mu$Hz.

3.5.5 Input frequencies

Finally, we tested the dependence of the measured parameters on the number of input frequencies. The above examples have included only the radial modes, so we have simulated the presence of non-radial modes by decreasing the mean frequency separation. Since we used the radial modes from a pulsation model (Stello, 2002), they showed a small scatter of $0.2\,\mu$Hz from perfectly uniform spacing. This scatter was kept constant as we reduced the frequency separation and included more frequencies.

The results of the change in frequency separation are shown in Fig. 3.10. As expected we see an increase in all measured parameters when increasing the number of input frequencies (decreasing the frequency separation), due to the increase in the power, although $\mathrm{W_{env}}$ is nearly unaffected.

3.5.6 Finding the optimum input parameters

We find the most likely damping time by examining $\mathrm{Max_{peak}/Max_{smooth}}$, which is relatively insensitive to $\mathrm{Amp_{scale}}$, envelope width, input frequencies, and noise, but not to the damping time (see Fig. 3.11). Thus the properties of the amplitude spectra we measure with the ratio $\mathrm{Max_{peak}/Max_{smooth}}$ are mainly determined by

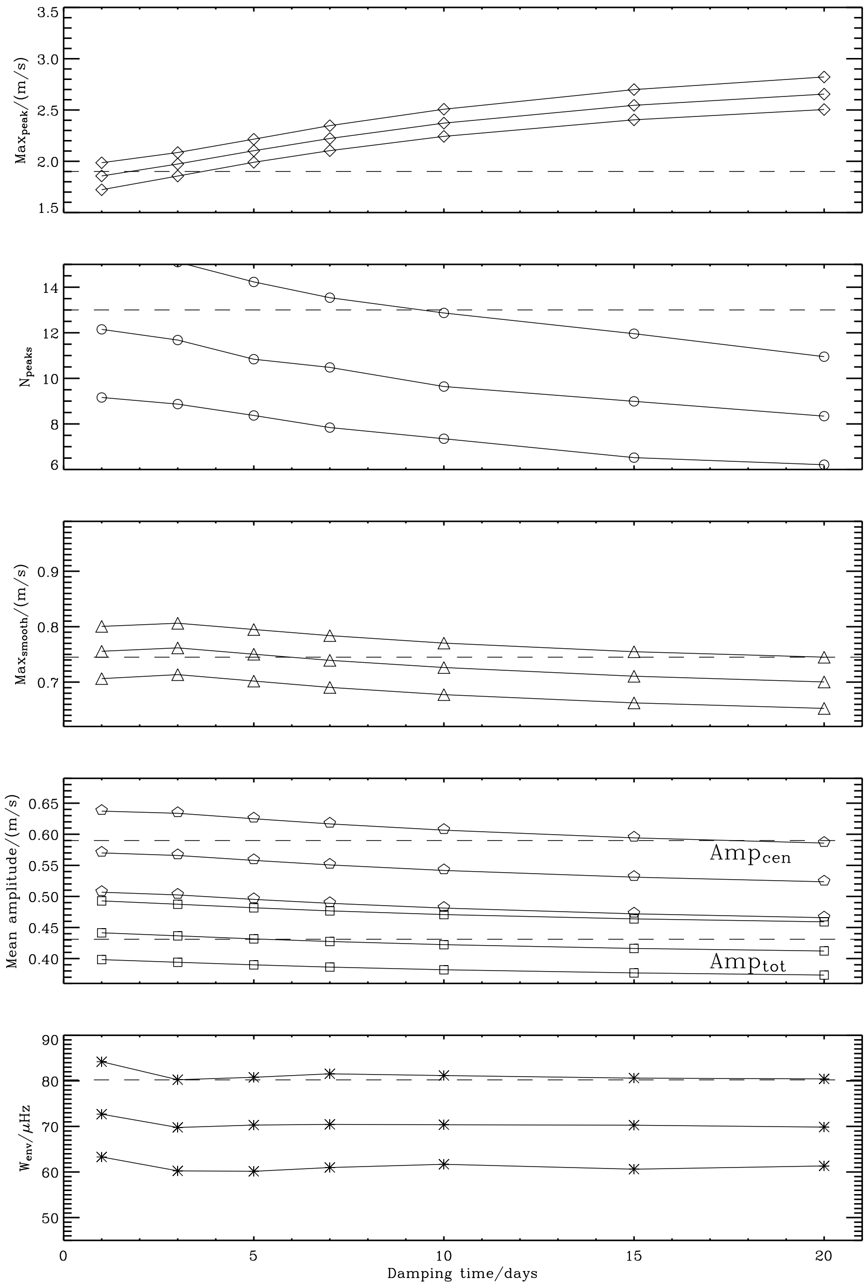

Figure 3.9: The effect of changing the envelope width. These panels are similar to those plotted in Fig. 3.6, but for three different values of envelope width. Each measured parameter is therefore shown as three points for every damping time. The input widths (from bottom to top in each panel) are: $x = 2$ ($\mathrm{FWHM_{in}} = 48.0\,\mu$Hz) (as in Fig. 3.6), $x = 1.2$ ($\mathrm{FWHM_{in}} = 64.0\,\mu$Hz), and $x = 0.7$ ($\mathrm{FWHM_{in}} = 81.6\,\mu$Hz). All parameters show an increase as the envelope width increases.

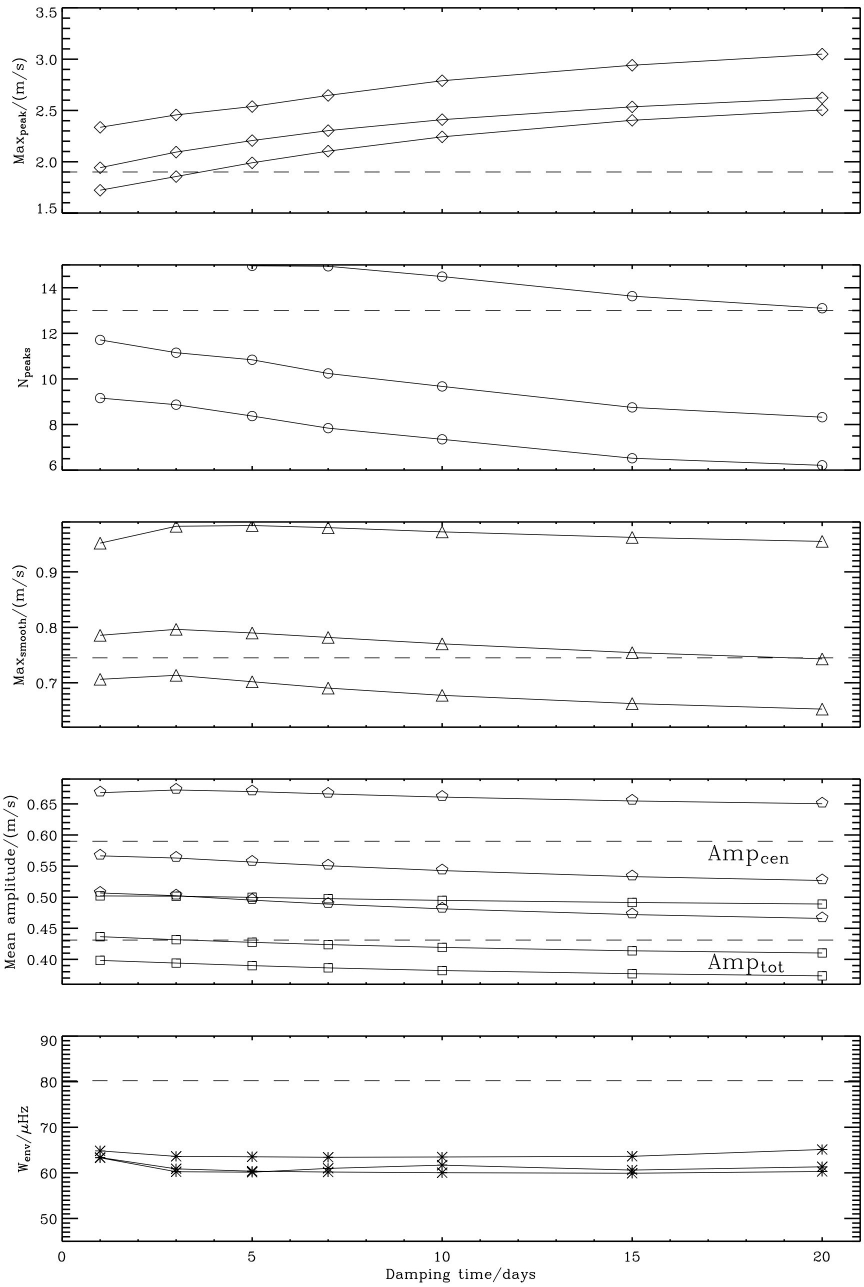

Figure 3.10: The effect of changing the number of input frequencies. These panels are similar to those plotted in Fig. 3.6, but for three different values of the frequency separation. Each measured parameter is therefore shown as three points for every damping time. The frequency separations (from bottom to top in each panel) are: 6.8 μHz (as in Fig. 3.6), 5.0 μHz, and 3.4 μHz. All parameters show an increase as the frequency separation decreases. The 3.4 μHz simulations corresponds to having one non-radial mode per radial mode positioned halfway between each radial mode.

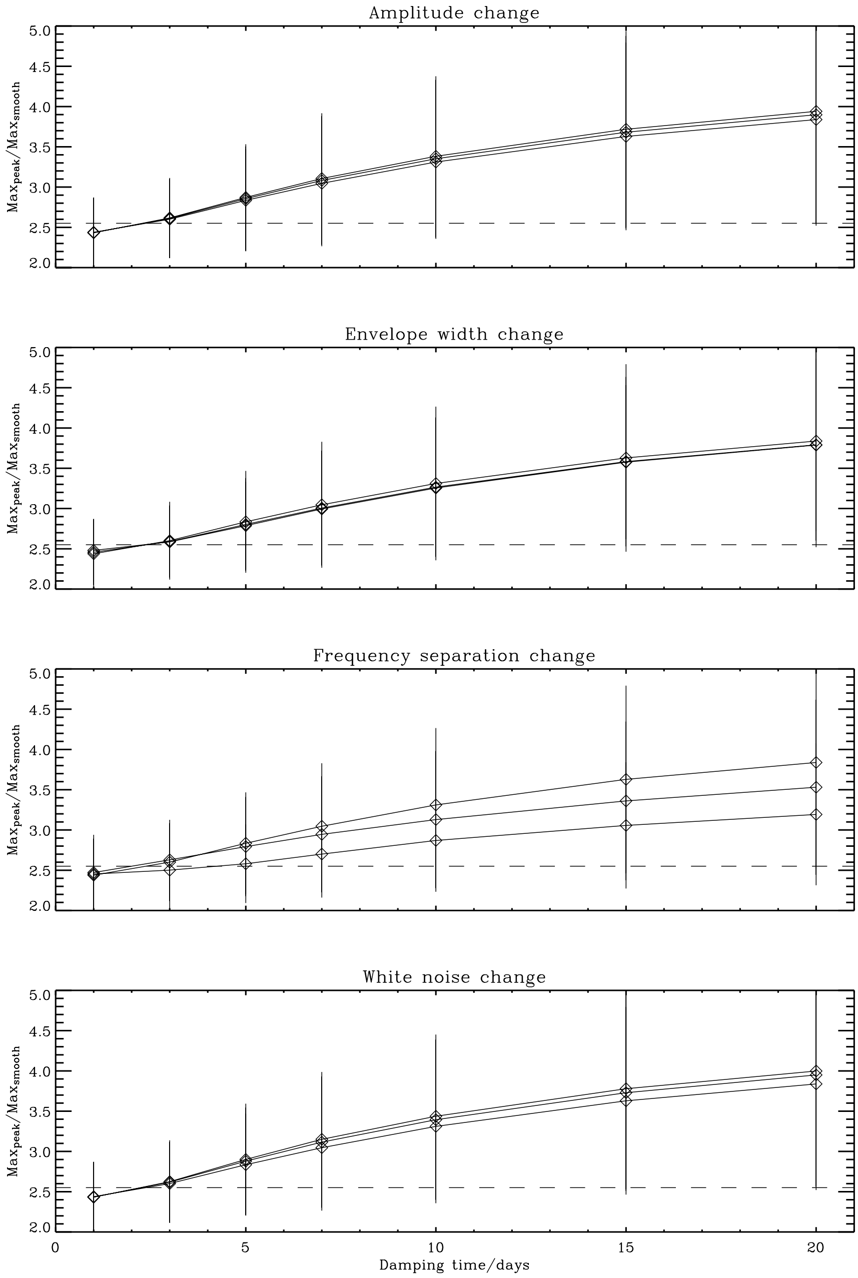

Figure 3.11: The ratio $\mathrm{Max_{peak}}/\mathrm{Max_{smooth}}$ as a function of damping time. The four panels show the sensitivity of $\mathrm{Max_{peak}}/\mathrm{Max_{smooth}}$ to changes to the different input parameters. The values of the input parameters are the same as shown in the former figures in Sect. 3.5.

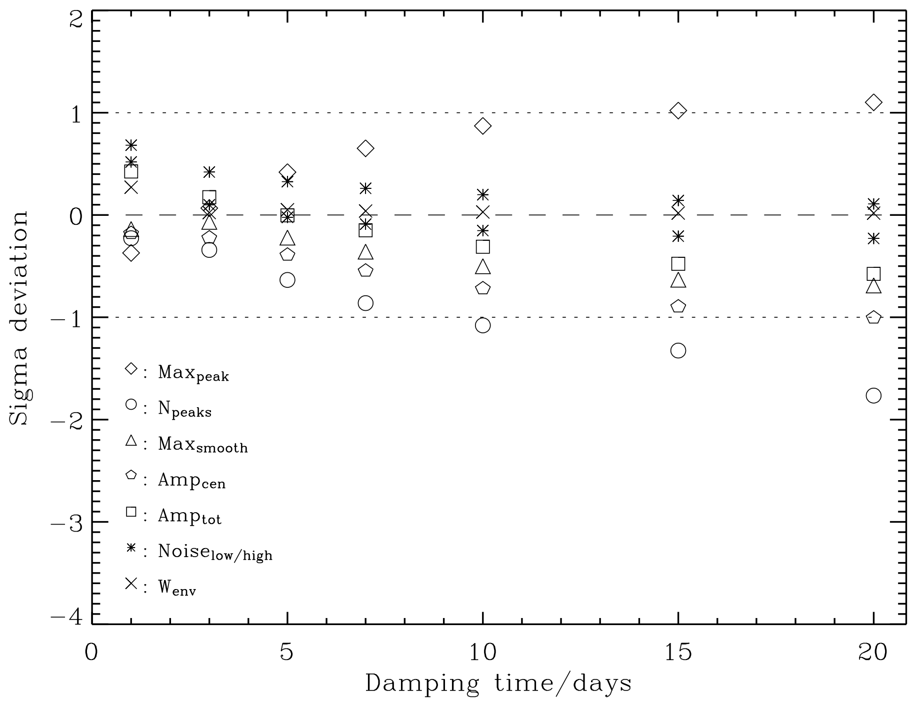

Figure 3.12: The deviation between observations and simulations relative to the rms scatter of the simulations (sigma deviation) of all eight measured parameters as a function of input damping time. The input parameters (optimised for $d \sim$ 2–3 days) are: $\mathrm{Amp_{scale}} = 2.0\,\mathrm{m/s}$, $x = 0.7$ ($\mathrm{FWHM_{in}} = 81.6\,\mu\mathrm{Hz}$), $\mathrm{Noise_{white}} = 0.10\,\mathrm{m/s}$, $\mathrm{Noise_{slope}} = 1.5$, $\mathrm{Noise_{scale}} = 3.0$, and 18 input frequencies with a mean frequency separation of $6.8\,\mu$Hz.

the damping time. This ratio therefore provides a robust measure of the damping time, although it is not very precise (due to scatter). From Fig. 3.11 we see that the most likely damping time, given the observations, is $d \simeq 2$ days. In Fig. 3.12 we show the results of simulations with a set of input parameters optimised for $d \sim$ 2–3 days while having the envelope fixed at $\mathrm{FWHM_{in}} = 81.6\ \mu$Hz (see Sect. 3.5.4). All eight parameters are plotted in a single plot by showing the difference between observations and simulations relative to the rms scatter in the simulations. We find the most likely amplitude of ξ Hya to be $\mathrm{Amp_{scale}} \sim 2.0\,\mathrm{m/s}$.

When we optimised the input parameters for a damping time of ~ 15 days, we got roughly the same result as shown in Fig. 3.12. Changing the amplitude or the number of frequencies does not change $\mathrm{Max_{peak}}$ and $\mathrm{N_{peaks}}$ without also affecting the other parameters and worsening the fit (see Figs. 3.8 and 3.10). The problem with a damping time of ~ 15 days or longer is that we cannot produce enough high peaks while keeping the other measures of power down at the observed level.

It is possible to include a few extra modes (in addition to the 18 modes with mean frequency separation $6.8\,\mu$Hz) in the simulations and still have an acceptable fit with the observations because the change in the measured parameters is small, relative to the scatter, provided we also reduce the input amplitude slightly (see Figs. 3.8 and 3.10).

3.6 Discussion and conclusion

We have, in the previous sections, described a method for generating realistic simulations of stochastically excited oscillations, including an arbitrary noise function and an arbitrary window function. Using time series produced by our simulator we showed how the damping time, amplitude, and other mode properties of the oscillations could be determined by comparing the overall structure of observed and simulated amplitude spectra. The method was applied to the single-site time series of radial velocity measurement of the red giant star ξ Hya (Stello, 2002; Frandsen et al., 2002).

Due to the stochastic nature of the simulated solar-like oscillations, we see large variations in the amplitude spectra when the length of the time series is not significantly ($\gtrsim$ 10 times) longer than the damping time. Hence, a large scatter is induced for some of the measured parameters that describe the characteristics of the amplitude spectra (see Fig. 3.6). In the case of ξ Hya, we are therefore not able to exclude the damping time of $\sim$ 15–20 days calculated by Houdek & Gough (2002). However, based on this single dataset, a shorter damping time of only a few days seems much more likely (see Fig. 3.12 *diamonds* and *circles*). A clear rejection of a damping time of 15 days or longer would require a reduction of the scatter seen in, e.g., Fig. 3.11 by at least a factor of two, and hence, using single-site observations, a time series of $\sim$ 150 days (assuming that the measured parameters from the observations are unchanged). The optimum fit to the observations, assuming purely radial modes, gave a maximum amplitude $\sim$ 2.0 m/s, in good agreement with the calculations by Houdek & Gough (2002), and damping time $\sim$ 2–3 days. Also, due to scatter, it was not possible to exclude the presence of a few extra modes beside the 18 modes with mean frequency separation 6.8 μHz. Since the theoretical calculations of the mode inertia (Teixeira et al., 2003) show that the radial modes should be excited to larger amplitudes than the higher degree modes, we conclude that our simulations strongly suggest that the ξ Hya amplitude spectrum is dominated by radial modes, but with a possible presence of a few higher order modes.

Below we itemise the limitations of the current investigation and discuss their consequences:

- Our approximation of using a damping time that does not vary with frequency underestimates the damping time for low frequency modes (by creating more peaks) while overestimating the damping time at the high frequency end (producing fewer peaks) relative to the theoretical damping rate (Houdek & Gough, 2002, their Fig.1). Hence, due to these opposing effects, this should have little effect on our results.

- We included non-radial modes by assuming that they were excited to the same amplitudes as the radial modes in the same frequency range. A comprehensive treatment of the non-radial modes should include both the relative mode inertia, based on a pulsation model, and the spatial response of the observations due to projection effects for modes of different degree. The technique presented in this paper to measure mode life time is probably not sensitive enough to make worthwhile a more comprehensive treatment of the non-radial modes.

- We tested for any significant effect from the adopted deviation of the frequencies from equal spacing by testing both the scatter of $0.2\,\mu$Hz seen in the pulsation model (as in the examples shown in Sect. 3.5) and the larger scatter ($0.6\,\mu$Hz) seen when the observed frequencies were ordered to match the radial modes (see Stello, 2002). In these two cases, the eight measured parameters were found to be nearly unchanged, with a deviation of less than 0.1σ, which is the precision with which we know the mean values based on 100 independent simulations.

  Furthermore, we tested a very irregular frequency distribution by using the 13 observed peaks with S/N$\geq$ 3.5 (see Stello, 2002) as input frequencies, neglecting possible contamination from alias peaks and noise. The results are similar to those shown in Sect. 3.5.

  We conclude that the regularity in the input frequencies is not important for obtaining our current result.

- The observed velocities of ξ Hya were reduced using one reference point per night, which produced a high-pass filtering of the time series (Frandsen et al., 2002). It would presumably require somewhat different values of the input parameters to match the unfiltered amplitude spectrum. We expect this would mostly affect the input noise and amplitude, by underestimating them, and to a lesser extent the damping time.

- We chose to use the smoothed observed amplitude spectrum as the frequency envelope because it represents the actual observations. We expect that a Gaussian profile could be used for simplicity with little effect on the results.

- We used two successive relatively narrow boxcars to smooth the amplitude spectrum in order to obtain $\mathrm{Max}_{\mathrm{smooth}}$. This method preserved the large-scale structure while removing variations on small scales. Increasing the boxcar widths by a factor of 2 or 3 did not produce any significant change in the difference between $\mathrm{Max}_{\mathrm{smooth}}$ of simulations and observations.

- To test the robustness of our method we applied it to measurements in velocity of α Cen A (Butler et al., 2004). Based on a plot similar to Fig. 3.11, we obtain a damping time of $\sim$ 0–5 days. A complete analysis, as shown for ξ Hya, has not been applied to α Cen A. Since α Cen A is very similar to the Sun, one would expect the damping time to be only a few days. Our result is consistent with both the solar value (3–4 days) and the value of 1–2 days for α Cen A found by Bedding et al. (2004).

In general, we see from our simulations that when comparing the estimated amplitude (either from scaling or theoretical calculations) with observations, the amplitude associated with a star from a single dataset can vary significantly, especially for stars with mode life times that are long compared to the length of the time series (see Fig. 3.6).

In a future paper, a more detailed frequency analysis of ξ Hya will be presented, including an analysis of the scatter of frequencies about a uniform distribution, which would test the damping time results given in this paper (see Chapter 4).

Chapter 4

A new method for measuring the mode lifetime

The content of this chapter was published in Astronomy & Astrophysics in 2006 by Dennis Stello in collaboration with Hans Kjeldsen, Tim Bedding and Derek Buzasi (Stello et al., A&A, 448, 709). I generated and analysed the data and developed the method for measuring the mode lifetime of stochastically excited and damped oscillations. I was supervised by Hans Kjeldsen and Tim Bedding.

4.1 Abstract

We introduce a new method to measure frequency separations and mode lifetimes of stochastically excited and damped oscillations, so-called solar-like oscillations. Our method shows that velocity data of the red giant star ξ Hya (Frandsen et al., 2002) support a large frequency separation between modes of roughly 7 μHz. We also conclude that the data are consistent with a mode lifetime of 2 days, which is so short relative to its pulsation period that none of the observed frequencies are unambiguous. Hence, we argue that the maximum asteroseismic output that can be obtained from these data is an average large frequency separation, the oscillation amplitude and the average mode lifetime. However, the significant discrepancy between the theoretical calculations of the mode lifetime (Houdek & Gough, 2002) and our result based on the observations of ξ Hya, implies that red giant stars can help us better understand the damping and driving mechanisms of solar-like p-modes by convection.

4.2 Introduction

The mode lifetime of solar-like oscillations is an important parameter. The interpretation of the measured oscillation frequencies (and their scatter) relies very much on knowing the mode lifetime, but currently we know very little about how this property depends on the stellar parameters (mass, age and chemical composition). The theoretical estimates of mode lifetimes are based on a simplified description of the convective environment in which the damping and excitation of the modes takes place. Measurements of the mode lifetime, τ, in different stars will be very helpful for a more thorough treatment of convection in stellar modeling. In this paper the mode lifetime refers to the time for the amplitude to decrease by a factor of e.

The number of measurements of the mode lifetime, or damping time, is still very limited. Observations of main-sequence stars imply mode lifetimes of a few days in the Sun (Libbrecht, 1988; Chaplin et al., 1997), α Cen A (Bedding et al., 2004) and α Cen B (Kjeldsen et al., 2005). As pointed out by Bedding et al. (2005b), independent observational studies on the star Procyon do not agree on the measured frequencies, a disagreement that could be the result of a short mode lifetime. The power spectrum of the K giant Arcturus reported by Retter et al. (2003) could also be explained as a short mode lifetime ($\tau = 2$ days) of a single mode. If the mode lifetime does not increase with oscillation period, this would limit the prospects of asteroseismology on evolved stars that have periods of several hours or longer, because of poor coherence of the oscillations. Only when we look at M giants – the semi-regular variables – do we see evidence for longer lifetimes, ranging from years to decades (Christensen-Dalsgaard et al., 2001; Bedding et al., 2003, 2005a).

The theoretical predictions of mode lifetimes for unevolved stars like the Sun (Houdek et al., 1999) and α Cen A (Samadi et al., 2004) are in a fairly good agreement with the observed values. However, for the more evolved red giant star ξ Hya,

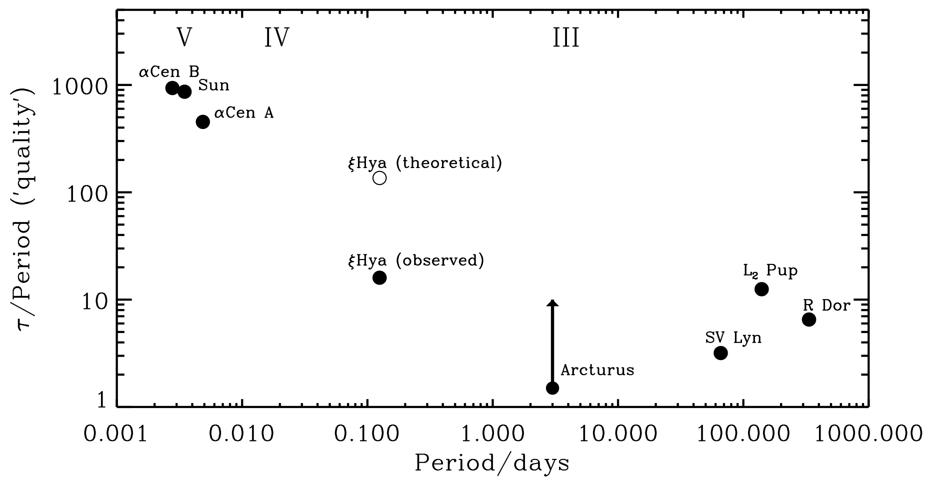

Figure 4.1: The oscillation 'quality' factor vs. period for selected stars. Filled symbols are measured, while the empty symbol shows the theoretical value. The arrow indicates a lower limit. Luminosity classes are indicated at the top. The measured values are from: α Cen B, Kjeldsen et al. (2005); Sun, Chaplin et al. (1997); α Cen A, Kjeldsen et al. (2005); ξ Hya (theoretical), Houdek & Gough (2002); ξ Hya (observed), Paper I (see Chapter 3); Arcturus, Retter et al. (2003); L_2 Pup, Bedding et al. (2005a); SV Lyn and R Dor, Dind (2004).

there seems to be a significant discrepancy between theory ($\tau \sim$ 15–20 days; Houdek & Gough, 2002) and observation ($\tau \sim$ 2–3 days; Stello et al., 2004, hereafter Paper I; see Chapter 3). In Paper I we also measured the oscillation amplitude to be roughly 2 ms^{-1}, which was in good agreement with the theoretical value (Houdek & Gough, 2002).

In Fig. 4.1 we plot the measured ratios between the mode lifetime and period (the oscillation 'quality' factor) as a function of period for selected stars, including the theoretical value for ξ Hya. Roughly speaking, the 'quality' factor is the number of oscillation cycles with constant phase, and the higher this number, the better we can determine the frequency. Note that the relation between the mode lifetime τ and the the FWHM Γ (in cyclic frequency) of the corresponding resonant peak is $\Gamma = 1/(\pi\tau)$.

In this paper we further investigate the mode lifetime of ξ Hya and examine whether it limits the possible astrophysical output. We introduce a new method that measures repeated frequency patterns (e.g. the large frequency separation, $\Delta\nu_0$) and the mode lifetime of solar-like p-mode oscillations. We furthermore analyse the stellar power spectrum to establish the most likely mode lifetime, by comparing the cumulative power distribution of the observations with simulations. Finally, the ambiguity of the measured frequencies is quantified.

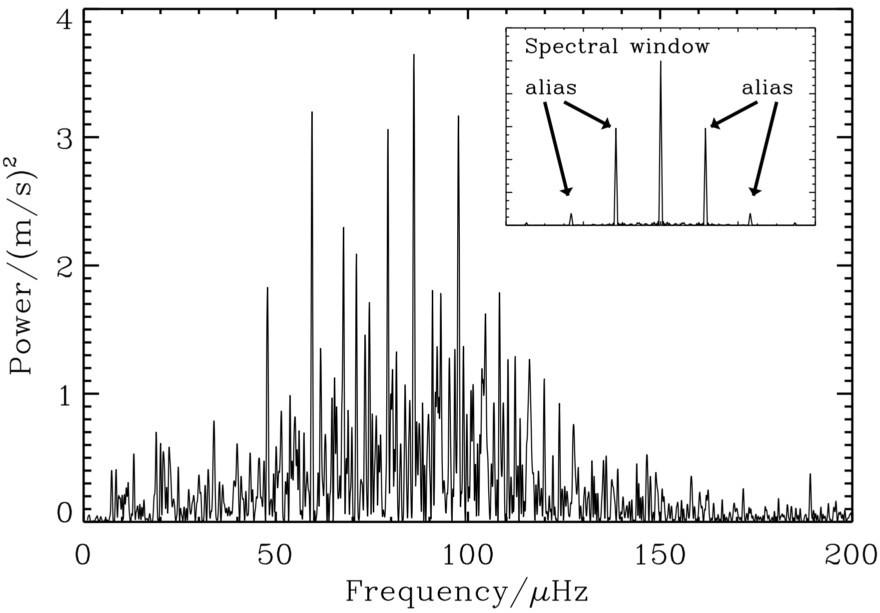

Figure 4.2: Power spectrum of ξ Hya. The frequency axis of the spectral window in the inset is scaled to match that of the main plot.

4.3 The ξ Hya data set and previous results

We use the same data set as in Paper I (see Chapter 3), which comprises 433 measurements of radial velocity covering almost 30 days of single-site observations using the CORALIE spectrograph at La Silla (ESO, Chile). The average noise per measurement is $\sigma_{\text{measure}} = 2.33\,\text{ms}^{-1}$, and the data provide a clear detection of excess power in the Fourier spectrum at roughly $90\,\mu$Hz (period $\sim$ 3 hours) with many peaks of S/N>3 (see Fig. 4.2). For further details about the observations see Frandsen et al. (2002). Note that during the reduction the data was high-pass filtered (Frandsen et al., 2002), but we have shown with simulations that this does not affect the power spectrum above $20\,\mu$Hz. Using the autocorrelation of the power spectrum Frandsen et al. (2002) found a frequency spacing of $6.8\,\mu$Hz, which is in good agreement with the large frequency separation, $\Delta\nu_0$, from a pulsation model of the star (Christensen-Dalsgaard, 2004). For further analysis on the stellar parameters of ξ Hya see e.g. Stello (2002); Frandsen et al. (2002); Teixeira et al. (2003); Paper I (see Chapter 3); Thévenin et al. (2005).

In Table 4.1 we give the frequencies used in the current investigation. We used the conventional method of iterative sine-wave fitting ('prewhitening') to measure the 10 frequencies listed in Table 4.1 (see Appendix 4.7.1). The uncertainties are calculated according to Montgomery & O'Donoghue (1999) (see also Kjeldsen, 2003). We note that these frequencies are not exactly the same as those quoted by Frandsen et al.

Table 4.1: Measured frequencies and amplitudes for ξ Hya

ID	Frequency μHz	Amplitude ms^{-1}	S/N	Frandsen et al. 2002
ν_1	85.91(3)[a]	1.89(24)[a]	6.3	85.96(3)
ν_2	59.43(3)	1.75	5.8	59.43(3)
ν_3	79.13(3)	1.65	5.5	79.13(3)
ν_4	95.21(4)	1.33	4.4	95.28(4)
ν_5	108.20(4)	1.24	4.1	108.22(4)
ν_6	101.32(4)	1.17	3.9	101.16(4)
ν_7	98.76(4)	1.12	3.7	98.77(5)
ν_8	112.29(5)	1.11	3.7	–.–
ν_9	105.14(5)	1.01	3.4	105.13(5)
ν_{10}	73.38(5)	1.02	3.4	–.–

[a] The errors are derived from: $\sigma_f = \sqrt{6}/(T_{\mathrm{obs}} \cdot \mathrm{S/N} \cdot \pi^{3/2})$, and $\sigma_{\mathrm{amp}} = \sqrt{2/\pi}\langle\mu_{\mathrm{amp}}\rangle$, where $\langle\mu_{\mathrm{amp}}\rangle = \sigma_{\mathrm{measure}}\sqrt{\pi/N_{\mathrm{obs}}}$, and $N_{\mathrm{obs}} = 433$ (see text).

(2002), who used a different method to measure the frequencies. This discrepancy is not surprising because the alias peaks (Fig. 4.2) are likely to introduce small frequency differences, depending on the method used to extract the frequencies. The uncertainties indicated in Table 4.1 are based on the signal-to-noise (S/N) and do not take into account the scatter of the frequencies arising from a short mode lifetime. This extra frequency scatter is the main subject of this paper.

4.4 The method

4.4.1 Background and definitions

From theoretical calculations we expect the oscillations in red giant stars to be dominated by radial modes (Christensen-Dalsgaard, 2004; Guenther et al., 2000; Dziembowski et al., 2001), which is also supported by the observations of ξ Hya (Paper I; see Chapter 3) and other red giants (Buzasi et al., 2000; Kiss & Bedding, 2003; Retter et al., 2003). We therefore assume that the frequencies, ν_n, of ξ Hya will show a simple comb pattern in the power spectrum with only radial modes. This can be described by the linear relation

$$\nu_n \simeq \Delta\nu_0 n + X_0 \,, \tag{4.1}$$

where $\Delta\nu_0$ is the separation between mode frequencies of successive order n and X_0 is an offset.

The finite lifetimes of the oscillation modes will introduce deviations of the measured frequencies from the true mode frequencies and hence from the regular comb pattern (Anderson et al., 1990; Bedding et al., 2004). In Fig. 4.3 we illustrate this by showing, schematically, the comb pattern of 'true' mode frequencies (dashed lines; Eq. 4.1) and the measured frequencies (solid peaks). The deviations, indicated with $X(\nu_i)$ (Eq. 4.2), are independent because each mode is excited independently.

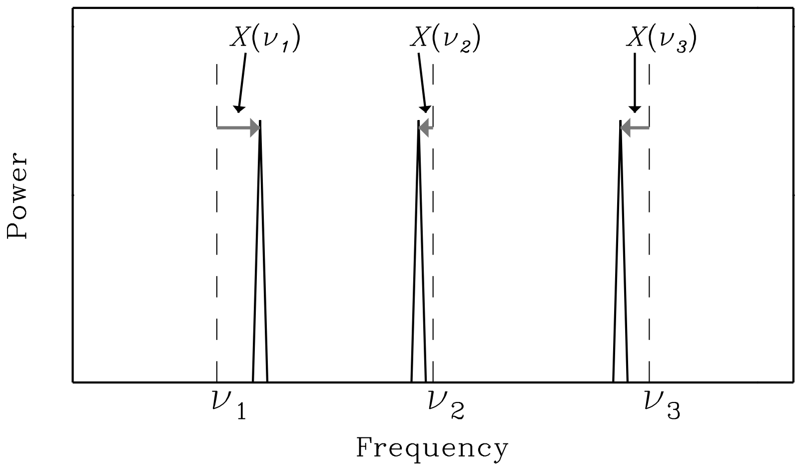

Figure 4.3: Schematic illustration of the frequency scatter due to a finite mode lifetime. Dashed lines are the true mode frequencies (Eq. 4.1), and solid peaks are measured frequencies.

Shorter mode lifetimes will give larger deviations. Following Bedding et al. (2004) and Kjeldsen et al. (2005), we estimate the mode lifetime from the scatter of the measured frequencies about a regular pattern. Our method differs by using a comb pattern for the reference frequencies, and by not requiring us to assign the mode order or degree to the measured frequencies. This is an advantage when the power spectrum is crowded due to aliasing and noise, as in this case, but the drawback is lower sensitivity to the mode lifetime.

The first step is to find the comb pattern that best matches our measured frequencies, $\nu \equiv [\nu_1, \ldots, \nu_{\mathrm{N}}]$. We do this by minimising the rms difference between the measured frequencies and those given by Eq. 4.1, with $\Delta\nu_0$ and X_0 as free parameters. The individual deviations are

$$X(\nu_i) \equiv (\nu_i - X_0) \bmod \Delta\nu_0 \,, \tag{4.2}$$

where we use a modulo operator that returns values between $-\frac{1}{2}\Delta\nu_0$ and $\frac{1}{2}\Delta\nu_0$. The rms scatter of X is then

$$\sigma_X(\nu; \Delta\nu_0, X_0) = \frac{\sqrt{2}}{\Delta\nu_0}\sqrt{\frac{1}{N}\sum_{i=1}^{N} X(\nu_i)^2} \,. \tag{4.3}$$

Here, $N = 10$ is the number of frequencies. The normalisation factor, $\sqrt{2}/\Delta\nu_0$, is included to make σ_X independent of $\Delta\nu_0$ for randomly distributed frequencies. We find the minimum of σ_X, $\min(\sigma_X)$, using the Amoeba minimisation method (Press et al., 1992), and calibrate it against simulations with known mode lifetime, as described in the next section. As a by-product, we also get estimates for $\Delta\nu_0$ and X_0.

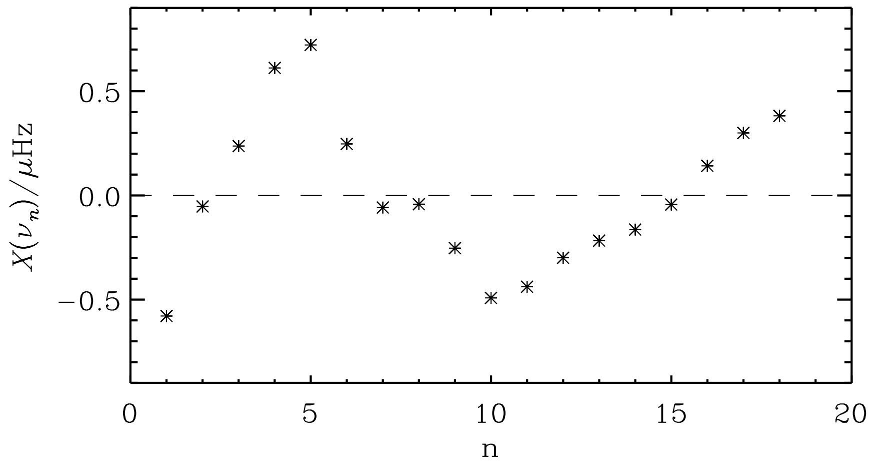

Figure 4.4: Deviation of input frequencies from a comb pattern (Eq. 4.2).

4.4.2 Simulations and calibration

We simulated the ξ Hya time series using the method described in Paper I (see Chapter 3). The oscillation mode lifetime was an adjustable parameter, assumed to be independent of frequency, while the other inputs for the simulator were fixed and chosen to reproduce the observations (see Paper I, Fig. 12; see Chapter 3 Fig. 3.12). To make the simulations as realistic as possible, the input frequencies were the radial modes from a pulsation model of ξ Hya (Teixeira et al., 2003; Christensen-Dalsgaard, 2004). Since our model assumes the frequencies to be strictly regular (Eq. 4.3), the intrinsic deviation of the input frequencies from a comb pattern (see Fig. 4.4) will contribute to σ_X. However, as described in Sect. 4.4.3, this contribution turns out to be negligible and therefore does not affect our measurement of the mode lifetime in ξ Hya.

For different values of the mode lifetime, we simulated 100 time series with different random number seeds. For each we measured 10 frequencies ($\nu_1, \ldots, \nu_{10}$) using iterative sine-wave fitting (see Appendix 4.7.1) and then minimised σ_X. This provided 100 values of $\min(\sigma_X)$ for each mode lifetime, which can be compared with the observations. In Figs. 4.5 and 4.6 we illustrate the method, and Figs. 4.7 and 4.8 show the results. Fig. 4.5 shows $X(\nu_i)$ of all 1000 frequencies (10 frequencies from each of 100 simulated time series) for two mode lifetimes, (a) $\tau = 17$ days, and (b) $\tau = 2$ days. The difference in mode lifetime is clearly reflected in the difference in the scatter of $X(\nu_i)$. We note that the distribution of $X(\nu_i)$ (right panels) is affected by the presence of false detections of alias peaks from neighbouring modes at roughly $X(\nu_i) \sim 2\,\mu$Hz and $-2\,\mu$Hz (see Fig. 4.5a).

In Fig. 4.6 we show $\sigma_X(\nu; \Delta\nu_0, X_0)$ for the case of $\tau = 17$ days. To smooth the plotted surface we show the average of all 100 simulations. However, dur-

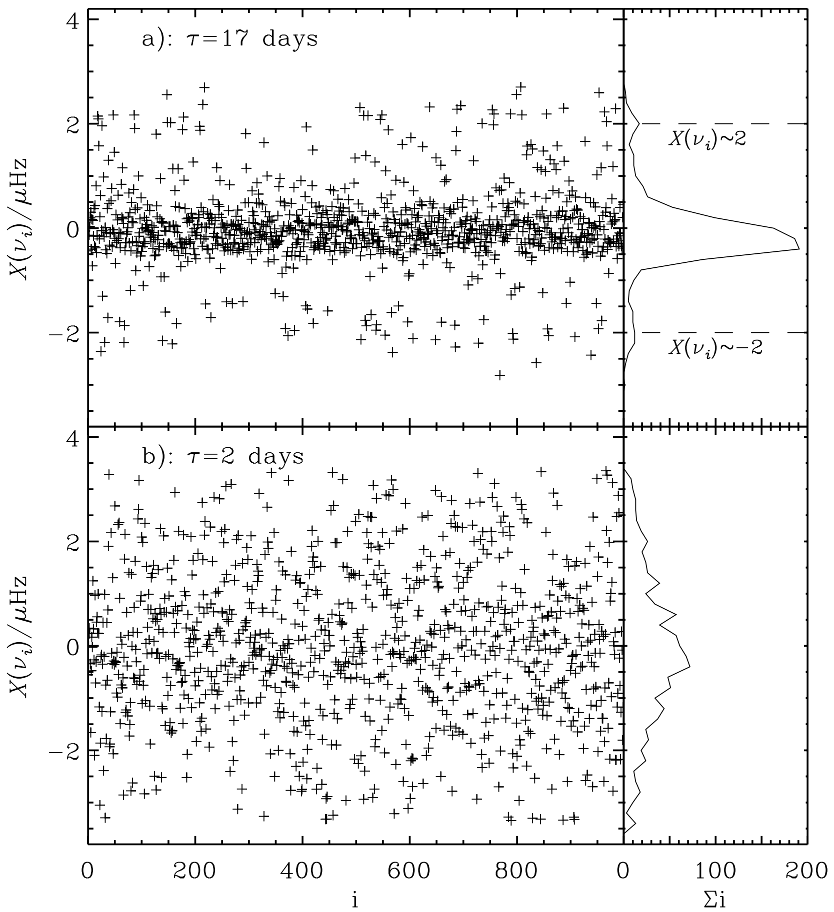

Figure 4.5: The deviation from a comb pattern (Eq. 4.2) for 10 measured frequencies from each of 100 simulated time series. The two horizontal bands (at $X(\nu_i) \sim 2\,\mu$Hz and $-2\,\mu$Hz, most evident in panel (a)) below and above the central band are signatures of the alias peaks that are present in our spectral window (see Fig. 4.2). To the right, the distributions are shown for each panel.

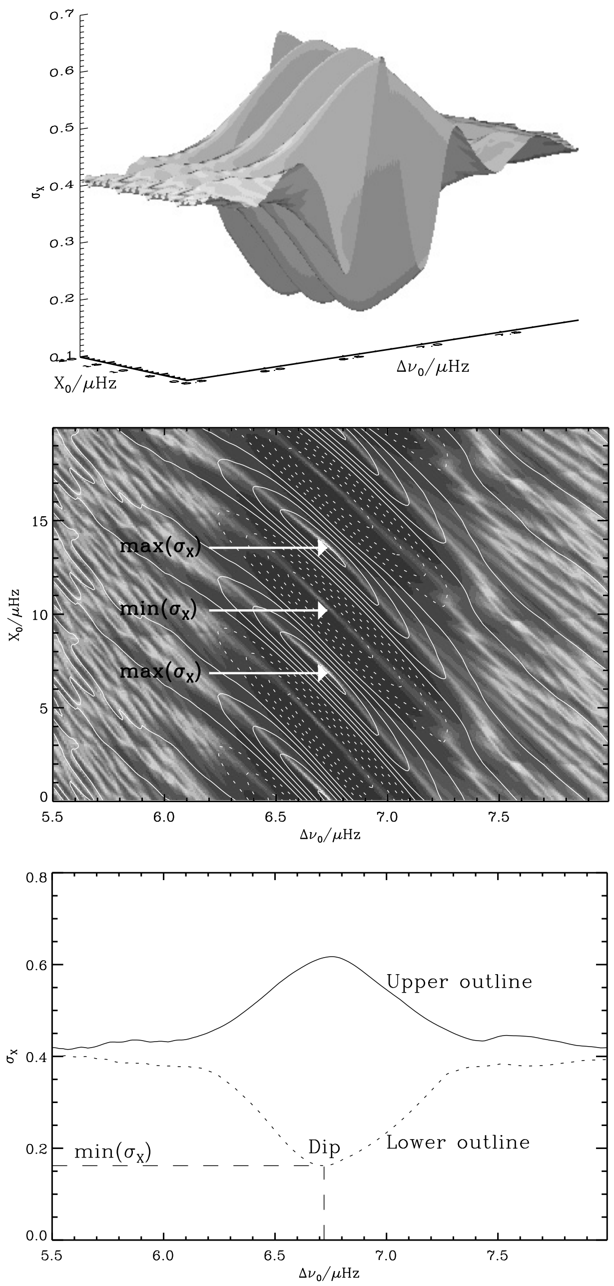

Figure 4.6: **Top panel:** 3D surface of σ_X, (averaged from 100 simulations with $\tau = 17$ days) as a function of the free parameters X_0 (plot range 0,20) and $\Delta\nu_0$ (plot range 5.5,8.0). **Middle panel:** The surface of σ_X viewed from above, where contours are plotted to guide the eye. Solid lines indicate contours above the mean level, while the dotted lines are those below. **Bottom panel:** The outline of the 3D surface viewed edge on in the X_0-direction. The two output parameters of the minimisation process, $\min(\sigma_X)$ and the corresponding $\Delta\nu_0$, are indicated by dashed lines.

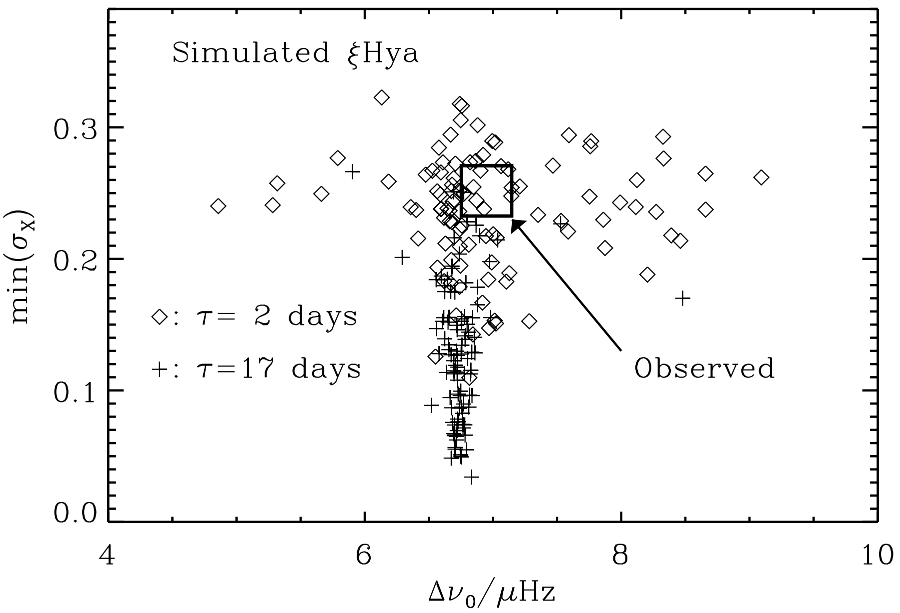

Figure 4.7: Output from our method applied on 100 simulations of ξ Hya with mode lifetime 2 days (diamonds), and 17 days (plus symbols). The square shows the observational point, and the size of the symbol indicates the uncertainty according to the chosen CLEAN algorithm (see Sect. 4.4.3).

ing the minimisation of σ_X, each simulations was treated separately. Note that $\sigma_X(\nu; \Delta\nu_0, X_0) = \sigma_X\ (\nu; \Delta\nu_0, X_0 + n\Delta\nu_0)$, where n is an integer, and that σ_X has maxima and minima for roughly the same $\Delta\nu_0$ that are separated by $\frac{1}{2}\Delta\nu_0$ on the X_0-axis.

The output parameters $\min(\sigma_X)$ and $\Delta\nu_0$ are plotted in Fig. 4.7. We see clearly that a smaller $\min(\sigma_X)$ (more prominent comb pattern) gives a more accurate $\Delta\nu_0$ determination. In the case of short mode lifetime, the frequency pattern is generally not very pronounced (high $\min(\sigma_X)$) mainly due to the false detections from alias peaks.

Due to the stochastic variations in the simulated time series, the value of $\min(\sigma_X)$ (Fig. 4.7) shows a large intrinsic scatter from one simulation to the next. This tells us the precision with which we can determine the mode lifetime, τ, from a single data set. For each τ, we compared the observed $\min(\sigma_X)$ with the distribution from 100 independent simulations. This gives a measure of whether the observed value is consistent with τ.

Figure 4.8 shows the distributions of $\min(\sigma_X)$ for simulations as histogram-plots, for different mode lifetimes (τ = 17 days, 5 days, 2 days, and 6 hours). The dashed line indicates the observed value. For a mode lifetime of 17 days (corresponding to the damping rate in cyclic frequency, plotted by Houdek & Gough 2002, of 0.1 μHz)

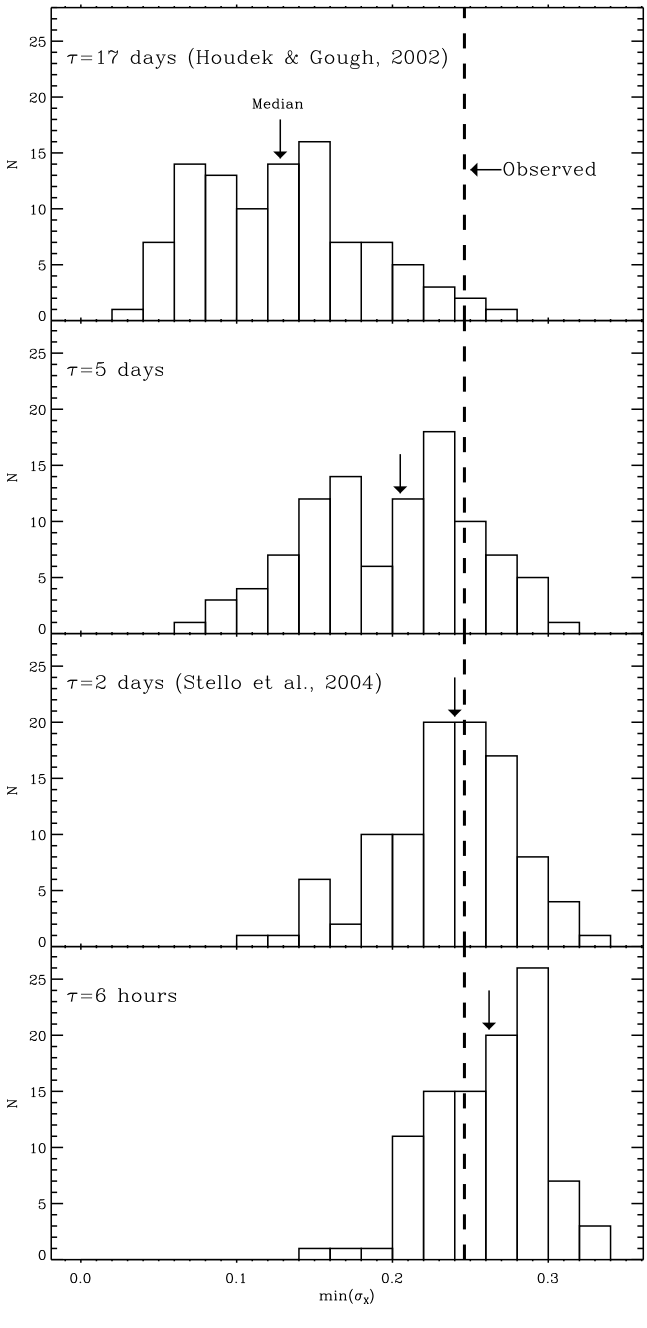

Figure 4.8: Distribution of the minimised scatter, σ_X, based on 10 frequencies from each of 100 simulations with different mode lifetimes: 17 days, 5 days, 2 days, and 6 hours. The dashed line indicates the value from the observations, and the vertical arrows show the median.

only a few out of 100 trials have a value for $\min(\sigma_X)$ as high as the observations. The exact number depends on the exact choice of analysis method (see Sect. 4.4.3). We find the best match with observations for mode lifetimes of about 2 days, in good agreement with Paper I (see Chapter 3). However, we note that there is also a reasonable match for all mode lifetimes less than a day, as their distributions all look very similar to the bottom panel. Randomly distributed peaks also show similar distributions to $\tau = 6$ hours. Hence, if the mode lifetime of ξ Hya is only a fraction of a day it would definitely destroy any prospects for asteroseismology on this star. We have confirmed this with simulations that do not include any comb patterns by simulating a single mode with a mode lifetime of 2 hours, similar noise, excess power hump, and with the same total power as the above simulations.

4.4.3 Robustness of method

An important step for a correct interpretation of the results shown in Fig. 4.8 is to test the robustness of our method. We tested the dependence of the two relevant output parameters $\Delta\nu_0$ and $\min(\sigma_X)$ on the following:

1. the initial guesses of $\Delta\nu_0$ and X_0 in the minimisation process of σ_X,
2. the number of frequencies used to calculate σ_X,
3. whether weighting of frequencies is used when calculating σ_X,
4. the frequency separation of input frequencies,
5. the intrinsic scatter of input frequencies,
6. the method for measuring frequencies.

We discuss each of these in turn in Appendix 4.7.2, but in summary, none of the listed points (1–6) have a significant effect on the results shown in Fig. 4.8.

4.5 Power and frequency analysis

To further investigate the mode lifetime for ξ Hya, we compared the observed cumulative distribution of the power spectrum from 1–190 μHz with that from simulations (Fig. 4.9). Note that the simulator is normalised so that on average it reproduces the observed power regardless of the mode lifetime (Paper I, Eq. 7; see Chapter 3 Eq. 3.7). For each level in power, we calculated the fraction of the power spectrum that is above that level (similar to Fig. 2 in Delache & Scherrer 1983; see also Brown et al. 1991; Bedding et al. 2005b; Bruntt et al. 2005). We see only few time series of $\tau = 17$ days that have a power distribution similar to that observed and on average the difference is significant, while the distributions for $\tau = 2$ days resemble the observations much better. We note that there is a large intrinsic variation seen in the power distributions for $\tau = 17$ days.

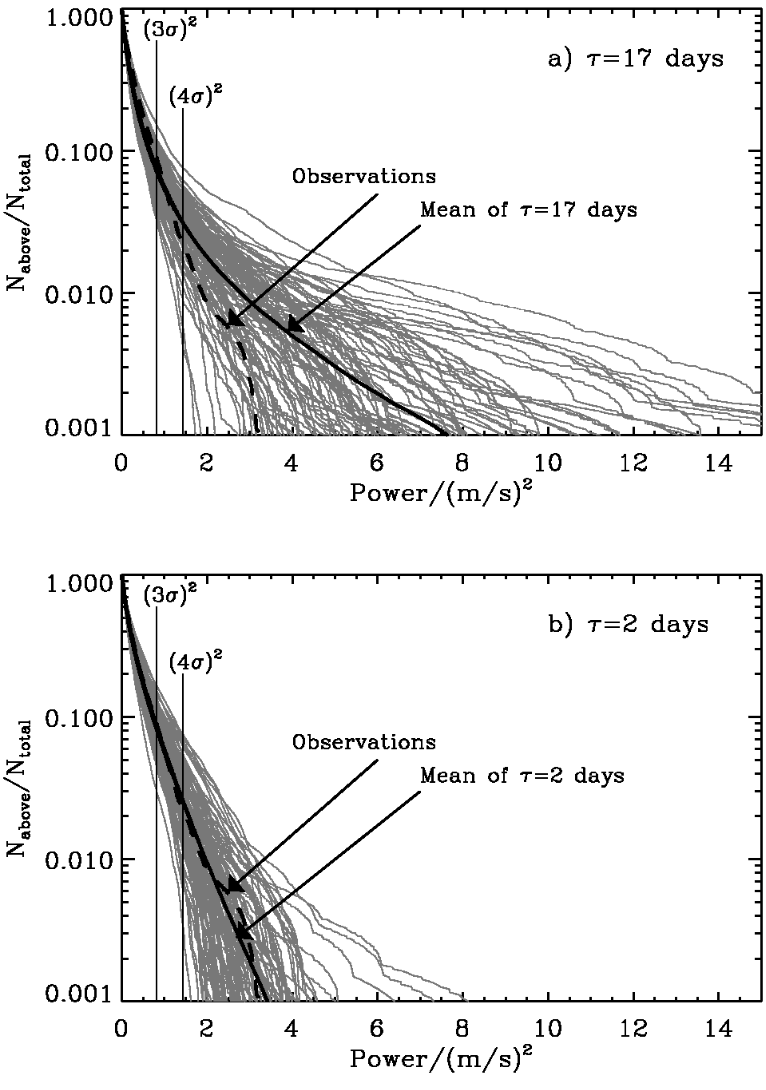

Figure 4.9: **Panel (a):** Cumulative distribution of power spectra from 100 simulations with $\tau = 17$ days (grey lines). The average distribution is shown with a black line. The dashed line indicates the distribution from the observations. **Panel (b):** Similar to panel (a), but with $\tau = 2$ days. The noise level in the observed power spectrum is indicated.

We also investigated the reliability of the observed frequencies (Table 4.1), using the simulations described in Sect. 4.4.2. The measured frequencies, together with the input frequencies and noise level are plotted in Fig. 4.10. Apart from the broadening of the mode frequencies due to damping, we also see false detections of alias peaks. This is most easily seen in panel (a) where the damping is less (a few examples of false detections are indicated). Our test shows that frequencies are not unambiguous if S/N$\lesssim$7–8, even for mode lifetimes of 17 days. For short mode lifetimes it looks rather hopeless to measure the individual mode frequencies with useful accuracy. The observed frequencies are all with S/N<6.3 and hence cannot be claimed to be unambiguous. Hence the frequencies in Table 4.1 (see also Fig. 4.10 bottom panel) should not be used for a direct comparison with individual frequencies from a pulsation model. The lack of a clear comb pattern similar to Fig. 4.10 (top panel) in the observed frequencies also supports a short mode lifetime.

4.6 Discussion and future prospects

Our best match for the mode lifetime of ξ Hya ($\tau \sim 2$ days) is in good agreement with our estimate in Paper I (see Chapter 3) but disagrees with theory (Houdek & Gough, 2002). This discrepancy indicates that red giants could be used to better understand the mechanisms of the driving and damping of oscillations in a convective environment. The short mode lifetime of ξ Hya also suggests a narrow range of mode lifetimes for a large range of stars, from the main sequence to the red giants, and hence a steep decline in the 'quality' factor (Fig. 4.1). The transition from the short mode lifetime regime to the much longer lifetimes of the semi-regular variables still needs to be investigated. It is likely to involve some kind of interaction between pure stochastic excitation and excitation by the κ mechanism, which is responsible for the oscillations we see in Mira stars (Bedding, 2003).

A difficulty in using the current observations of ξ Hya for asteroseismology arises from the severe crowding in the power spectrum. We now discuss possible origins of the crowding and some aspects of this issue.

We do not expect crowding from high amplitude non-radial modes in the power spectrum although low amplitude modes cannot be excluded (Christensen-Dalsgaard, 2004, Paper I; see Chapter 3). Additional simulations are needed to quantify the effect on the lifetime estimate from low amplitude non-radial modes, but we expect it to be small.

The crowding in the power spectrum comes partly from the single-site spectral window, which emphasises the importance of using more continuous data sets from multi-site campaigns or space missions. To illustrate this, we construct the combined time series from a hypothetical two-site observing campaign on ξ Hya where the observing window from each site is identical to that of the present data set obtained with the CORALIE spectrograph. The other site is assumed to be a twin at the complementary longitude (12 hour time shift), and the two individual data sets have identical sampling and noise. We simulated the stellar signal using $\tau = 2$ days,

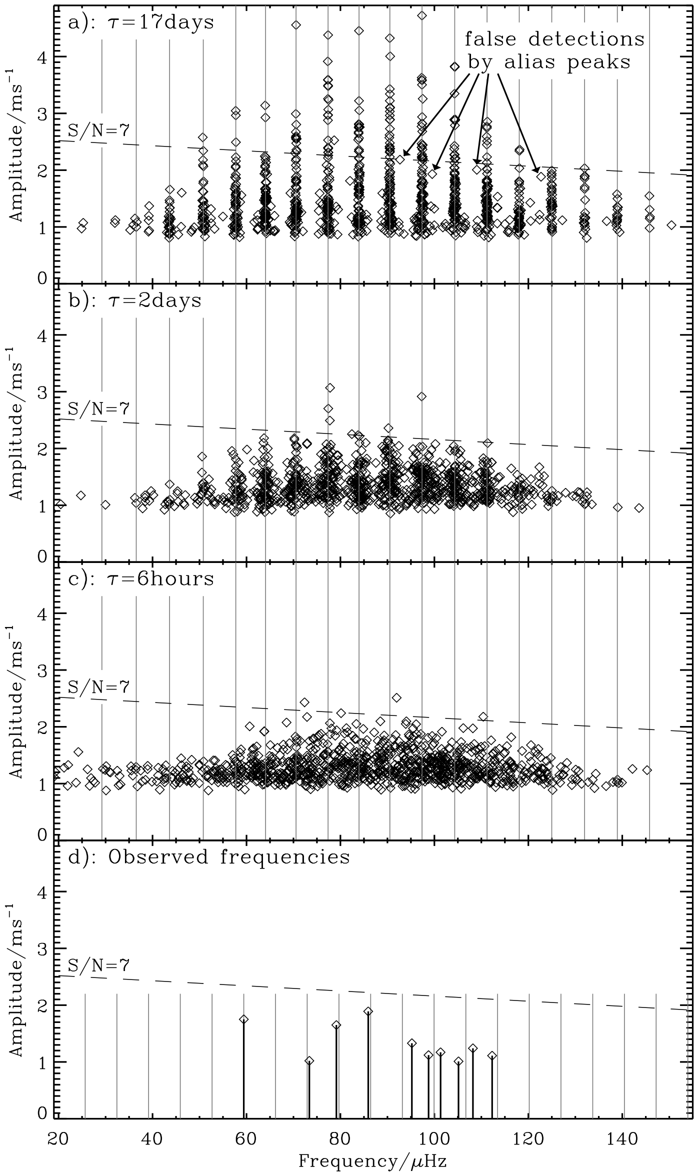

Figure 4.10: Each panel shows 1000 measured frequencies and their amplitudes (10 from each of 100 simulations). Dashed lines indicate 7 times the input noise, and the solid grey lines are the input frequencies. **Panel (a):** Mode lifetime = 17 days. **Panel (b):** Mode lifetime = 2 days. **Panel (c):** Mode lifetime = 6 hours. **Panel (d):** Observed frequencies and the best matching comb pattern (grey lines).

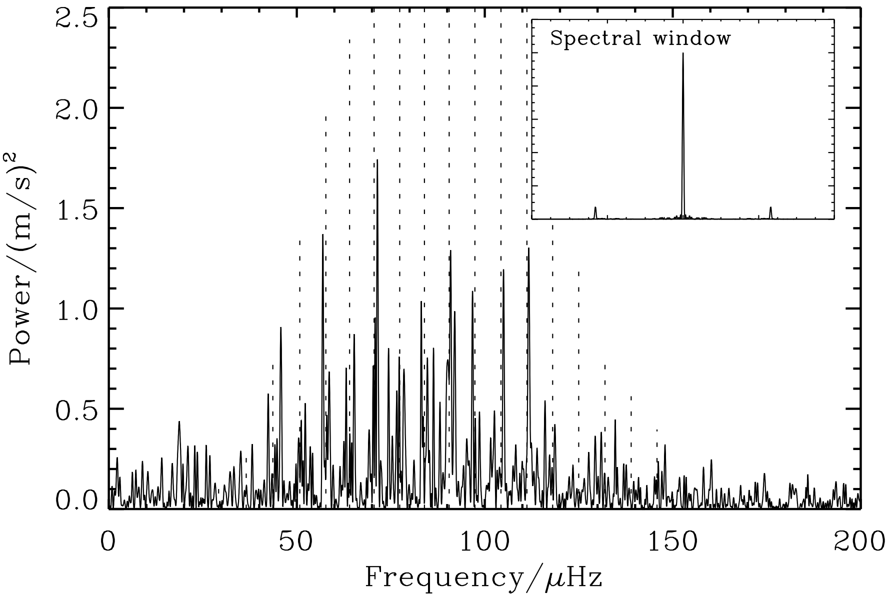

Figure 4.11: Power spectrum of simulated time series of ξ Hya ($\tau = 2$ days) using a window function from a two-site campaign where the sites are separated by 12 hours in longitude (see text). Dotted lines indicate the input frequencies.

with other parameters the same as for Fig. 12 in Paper I (see Chapter 3; Fig. 3.12). A power spectrum of such a two-site time series is shown in Fig. 4.11. Each mode profile is seen much more clearly, though slightly blended due to the short mode lifetime. Obviously, more can be obtained from such a spectrum than from our present data set (Fig. 4.2), but a thorough analysis of similar simulations should be done to determine the prospects for doing asteroseismology on ξ Hya.

As more high-quality asteroseismic data become available, simulations will continue to be an important tool for interpreting the data. However, one has to be careful about what can be deduced from simulations. Even though we may think, from an ideal perspective, that some parameters do not affect our measurements, this may turn out not to be true. A realistic noise source, the right window function, number- and scatter of frequencies, their amplitude and mode lifetime are all parameters that have to be considered when simulating oscillation data. Our comparison of the results from simplified simulations with more comprehensive simulations shows clearly that using simplified simulations can lead to erroneous conclusions. As an example, we measured an increase by a factor of two of $\min(\sigma_X)$ between simulations including only 1 and 18 input frequencies. This demonstrates that it is important to use realistic (non-simplified) simulations to relate frequency scatter to the mode lifetime.

A complete application of our method on other stars (e.g. α Cen A, ν Ind, η Boo, and the Sun) will be published in a forthcoming paper.

4.7 Conclusions

We introduced a new method that uses only the scatter of the measured frequencies from a comb pattern to measure the mode lifetime of the red giant ξ Hya. This method takes into account false detections of noise and alias peaks. We find that the most likely mode lifetime is about 2 days, and we show that the theoretical prediction of 17 days (Houdek & Gough, 2002) is unlikely to be the true value.

Due to the high level of crowding in the power spectrum, the signature from the p-modes is too weak to determine the large separation to very high accuracy. However, our measurement supports the separation of 6.8 μHz found by Frandsen et al. (2002).

We conclude that the only quantities we can reliably obtain from the power spectrum of ξ Hya are the mode amplitude, mean mode lifetime, and the average large frequency separation.

Our simulations show that none of the measured frequencies from the ξ Hya data set (Frandsen et al., 2002) can be regarded as unambiguous. Hence we suggest the measured frequencies given in Table 4.1 are not used for direct mode-matching with a pulsation model to constrain the stellar model. Only in the case of a greatly improved window function could this be possible.

Appendix

The following sections were published as appendices in the electronic version of the journal.

4.7.1 CLEAN test

The method described in Sect. 4.4 required extraction of many frequencies. We therefore tested two different sine-wave fitting or CLEANing methods, simple CLEAN and CLEAN by simultaneous fitting. We call them CLEAN1 and CLEAN2, respectively. The tests were done on our simulated time series to gain better understanding of the results from CLEANing and to determine which method was most favorable in our case. Both methods subtract one frequency at a time (the one with highest amplitude), but CLEAN2 recalculates the parameters (amplitude, phases, and frequencies) of the previously subtracted peaks while fixing the frequency of the latest extracted peak. In this way, the fit of the sinusoids to the time series is done simultaneously for all peaks. CLEAN1, however, does not recalculate the parameters of previously subtracted peaks. The time used by CLEAN2 is a factor of $1.5(N_{\rm extract}+1)$ longer than for CLEAN1, where $N_{\rm extract}$ is the number of extracted frequencies.

We made simulations similar to those described in Sect. 4.4.2 but with 17 equally spaced frequencies and no noise added. From each set of 100 time series with a given mode lifetime, 10 frequencies were extracted providing 1000 frequencies which we compared with the input frequencies. For coherent oscillations CLEAN2 is doing a perfect job while CLEAN1 detected 1% false peaks. If only true detections are considered, the scatter of the extracted frequencies relative to the input is roughly equal to the frequency resolution ($1/T_{\rm obs}$) for CLEAN2, while the CLEAN1 results scatter twice as much.

For non-coherent oscillations, the number of false detections increases for both methods and the relative success rates of the two methods become equally good (or bad), for mode lifetimes in the order of the observational window or shorter. In this regime, the scatter of the extracted frequencies gets dominated by the mode damping and is independent of the CLEANing method. For mode lifetimes below 5 days, the scatter of the frequencies is so pronounced relative to the spacing between modes and the alias peaks that they overlap and it cannot be determined whether an extracted frequency is false or not (see e.g. Fig. 4.5b).

The amplitude of a detected frequency found by both CLEANing methods generally differ by maximum $\pm 30\%$ but can for a few cases differ by 70%, being most severe for shorter mode lifetimes. There is a general trend that CLEAN2 ascribes lower amplitudes to the peaks of highest amplitude in a spectrum, and higher amplitudes to low amplitude peaks relative to CLEAN1. This is a result of the recalculation of the oscillation parameters in CLEAN2. The detected amplitude difference was not considered as crucial as we were interested in using the frequencies only. Since there is observational evidence that the mode lifetime of ξ Hya is below 5 days (Paper I; see Chapter 3), where the two methods perform equally well, we choose CLEAN1 due to its faster algorithm (by a factor of 17 in our case where $N_{\rm extract} = 10$).

4.7.2 Robustness tests

In this appendix we discuss each of the points (1–6) listed in Sect. 4.4.3 in turn:

(1) In the minimisation process, the initial guesses of $\Delta\nu_0$ and X_0 could give quite different outputs for $\Delta\nu_0$ on a data set with a shallow dip in σ_X (i.e weak comb pattern). For data with a deep dip in σ_X (i.e. strong comb pattern), $\Delta\nu_0$ is unaffected. We found that $\min(\sigma_X)$ was well determined if the initial guess of $\Delta\nu_0$ was within $\sim 1\,\mu$Hz of the true value. As a representative example we see $\pm 1.5\,\mu$Hz change in $\Delta\nu_0$ and only $\pm 0.008\,\mu$Hz change in $\min(\sigma_X)$ for the set of observed frequencies, which produced a shallow dip in $\min(\sigma_X)$. Our final setup (plotted in Fig. 4.8) was to fix the initial guess of $\Delta\nu_0$ at $6.8\,\mu$Hz, which we believe is within $1\,\mu$Hz of the true value, and to use 7 different X_0 values (separated $1\,\mu$Hz apart). We then chose the solution with the lowest minimum found from these 7 trials.

(2) We investigated the changes in the output parameters ($\min(\sigma_X)$, $\Delta\nu_0$), from varying the number of measured frequencies from 5 to 10. The average $\Delta\nu_0$ is unaffected by the number of frequencies, but more frequencies give a more accurate $\Delta\nu_0$ determination. For the observed frequencies $\Delta\nu_0$ changes by $\pm 0.5\,\mu$Hz in the tested regime (from 5 to 10 frequencies). Furthermore we observed higher values of $\min(\sigma_X)$, thus weaker comb patterns, with increasing number of frequencies, but

the relative difference between the $\min(\sigma_X)$ distributions from simulations and the observational data point did not change significantly.

We decided to use 10 frequencies since we trusted our $\min(\sigma_X)$ distributions more when the $\Delta\nu_0$ determinations were closer to the true value. Measuring more than 10 frequencies showed no clear advantage, for this particular data set.

(3) Assigning weights to each frequency according to its S/N makes the absolute value of $\min(\sigma_X)$ slightly less sensitive to the number of measured frequencies used to calculate $\min(\sigma_X)$, which is expected. Due to the higher weight given to the central part of the damping profile for each mode (Anderson et al., 1990), the frequency separation is also slightly better determined using weights. However, $\min(\sigma_X)$ will scatter slightly more, making it more difficult to distinguish $\min(\sigma_X)$ distributions from different mode lifetimes. This is probably a result of assigning lower weight to the tails of the damping profile. We chose not to use weights, to obtain the best possible result on the mode lifetime.

(4) Changing the large separation of the input frequencies did not produce any change in $\min(\sigma_X)$ for the tested range (6.8–7.2 μHz), but only changed the output $\Delta\nu_0$ accordingly. Hence, it is not crucial for our results on the mode lifetime to know the true frequency separation to a very high accuracy.

(5) We also changed the deviation, $X(\nu_i)$, from a comb pattern of the input frequencies. We used input frequencies that had a deviation twice as large as in the pulsation model (see Fig. 4.4), and also a frequency set that followed a perfectly regular comb. No significant change of the $\min(\sigma_X)$ distributions (Fig. 4.8) was observed. We believe this is because $\min(\sigma_X)$ is dominated by damping for the mode lifetimes we investigated.

(6) Finally, we investigated whether the choice of frequency extraction method affects $\min(\sigma_X)$ and $\Delta\nu_0$. Using three different algorithms on the observations provided 3 different sets of measured frequencies, and hence 3 different $\min(\sigma_X)$ values that ranged from 0.23–0.28. The corresponding output $\Delta\nu_0$ ranged from 6.7–7.2 μHz. We note, that the $\min(\sigma_X)$ distributions seen in Fig. 4.8 did not change significantly.

Chapter 5

M67: Observations and noise optimisation

The content of this chapter will be published in Monthly Notices of the Royal Astronomical Society in 2006 by Dennis Stello in collaboration with Torben Arentoft, Tim Bedding, Yacine Bouzid, Hans Bruntt, Zoltán Csubry, Thomas Dall, Zoe Dind, Søren Frandsen, Ronald Gilliland, Andrew Jacob, Henrik Jensen, Yong Beom Kang, Seung-Lee Kim, László Kiss, Hans Kjeldsen, Jae-Rim Koo, Jeong-Ae Lee, Chung-Uk Lee, János Nuspl, Chris Sterken and Róbert Szabó (Stello et al., MNRAS, 2006, accepted; astro-ph/0609340).

I initiated and led the entire campaign. I wrote four of the applications for telescope time and contributed to the others. I also wrote a 20 page comprehensive observing guide for all observers based on the framework of the observing guide written by Ron Gilliland and Tim Brown for their campaign in 1993. The guide can be found on the campaign's Web site (http://bigcat.phys.au.dk/∼srf/M67/). Søren Frandsen has setup the initial skin of the Web site, and I created and updated all the content. A substantial part of running this campaign was the daily updates of the Web site and communicating with all observers during observation. The daily observing summaries from each observer and other details can be found on the Web site. The observations were a collective effort by Torben Arentoft, Yacine Bouzid, Hans Bruntt, Zoltan Csubry, Zoe Dind, Ronald Gilliland, Andrew Jacob, Henrik Jensen, Yong Beom Kang, Seung-Lee Kim, Jae-Rim Koo, Jeong-Ae Lee, Chung-Uk Lee, Janos Nuspl, Chris Sterken, Robert Szabo and myself. I observed 10 nights at Siding Spring, and further details of who observed where can be seen in the caption of Table 5.1. I carried out all the data reductions and analysis except the basic CCD calibrations and extraction of time-series photometry from the SAAO data set, which was done by Torben Arentoft. I was supervised by Hans Kjeldsen and Tim Bedding, and Torben Arentoft introduced me to the MOMF photometry package which I used to extract the time series from the CCD images.

The first preliminary results from this campaign was published in proceedings of the SOHO 14/GONG 2004 Workshop (see List of publications on page 123). A

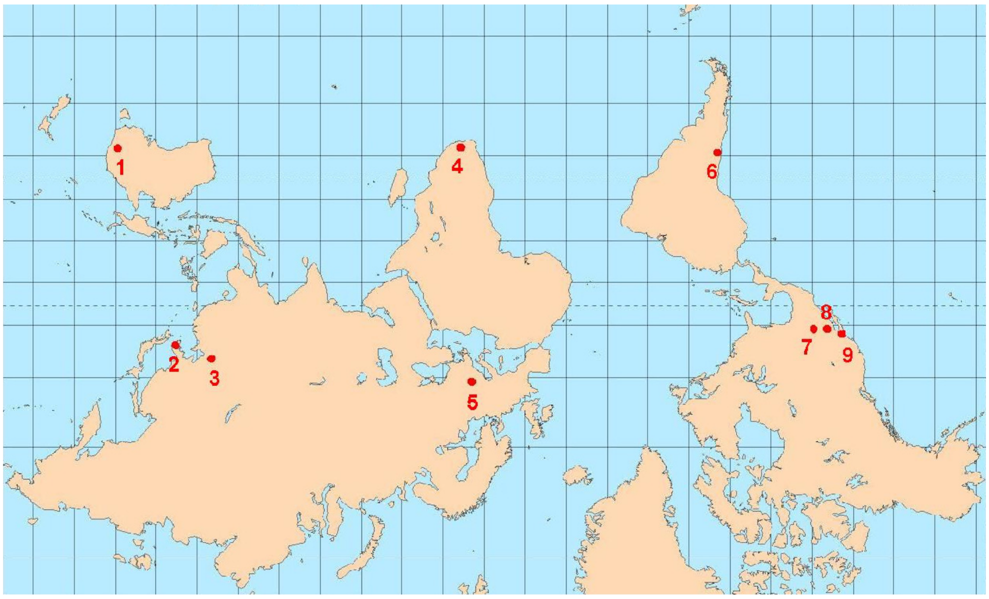

Figure 5.1: Participating telescope sites. 1: Siding Spring Observatory; 2: Sobaeksan Optical Astronomy Observatory; 3; Beijing Observatory; 4: South Africa Astronomical Observatory; 5: Konkoly Observatory; 6: La Silla; 7: Mt. Lemmon Optical Astronomy Observatory; 8: Kitt Peak National Observatory; 9: Mt. Laguna Observatory.

figure from that proceedings paper, which shows the locations of the participating telescope sites, is included here (see Fig. 5.1) for completeness, because no similar figure has been published in the following peer-reviewed papers (see Chapters 5 and 6). We note that Beijing Observatory did not provide any data, and is therefore not included in the following discussions.

Although δ Scuti stars were not the main targets of the M67 campaign (which are presented in Chapters 5 and 6), the data sample provided time series that were superior compared to previous studies. Hence we had the opportunity to do analysis of the δ Scuti stars of the cluster much more detailed than ever before. A paper specifically addressing δ Scuti pulsations in the blue straggler stars in M67 will be published by Bruntt, Stello, Suarez et al. (2006 in prep.; see List of publications on page 123).

5.1 Abstract

We report on an ambitious multi-site campaign aimed at detecting stellar variability, particularly solar-like oscillations, in the red giant stars in the open cluster M67 (NGC 2682). During the six-week observing run, which comprised 164 telescope nights, we used nine 0.6-m to 2.1-m class telescopes located around the world to obtain uninterrupted time-series photometry. We outline here the data acquisition and reduction, with emphasis on the optimisation of the signal-to-noise of the low amplitude (50–500 μmag) solar-like oscillations. This includes a new and efficient method for obtaining the linearity profile of the CCD response at ultra high precision (~ 10 parts per million). The noise in the final time series is 0.50 mmag per minute integration for the best site, while the noise in the Fourier spectrum of all sites combined is 20 μmag. In addition to the red giant stars, this data set proves to be very valuable for studying high-amplitude variable stars such as eclipsing binaries, W UMa systems and δ Scuti stars.

5.2 Introduction

Asteroseismology of stellar clusters is potentially a powerful tool. The assumption of a common age, distance, and chemical composition provides stringent constraints on each cluster member, which significantly improves the asteroseismic output (Gough & Novotny, 1993). Hence, detecting oscillations in cluster stars in a range of evolutionary states holds promise of providing new tests of stellar evolution theory. Driven by this great potential, several studies have been aimed at detecting solar-like oscillations in the open cluster M67 (Gilliland & Brown, 1988; Gilliland et al., 1991; Gilliland & Brown, 1992a; Gilliland et al., 1993) and in the globular cluster M4 (Frandsen et al., 2006, in prep.). The most ambitious campaign was reported by Gilliland et al. (1993), who used seven 2.5-m to 5-m class telescopes during one week in a global photometric network to target 11 turn-off stars in M67. Despite these efforts, they did not claim unambiguous detection of oscillations. However, one of their conclusions was that oscillations should be detectable in the more evolved red giant stars due to higher expected oscillation amplitudes. However, the oscillation periods of up to several hours and expected frequency separations of a few 10^{-6} Hertz would require a time base of roughly one month on these stars. Recent month-long studies using single- or dual-site high-precision radial velocity measurements ($\sigma \sim 2$ m/s) on bright field stars have clearly demonstrated that solar-like oscillations are present in red giant stars (Frandsen et al., 2002; Barban et al., 2004; De Ridder et al., 2006). However, due to non-continuous coverage these data suffered badly from aliasing in the Fourier spectrum, which complicated the detailed frequency analysis. Multi-site or space observations are therefore required (Stello et al., 2006c, see Chapter 4). Such observations will hopefully soon become available for red giant stars in the field from the COROT and Kepler missions. However, after the cancellation of the ESA Eddington mission, no current or planned space project

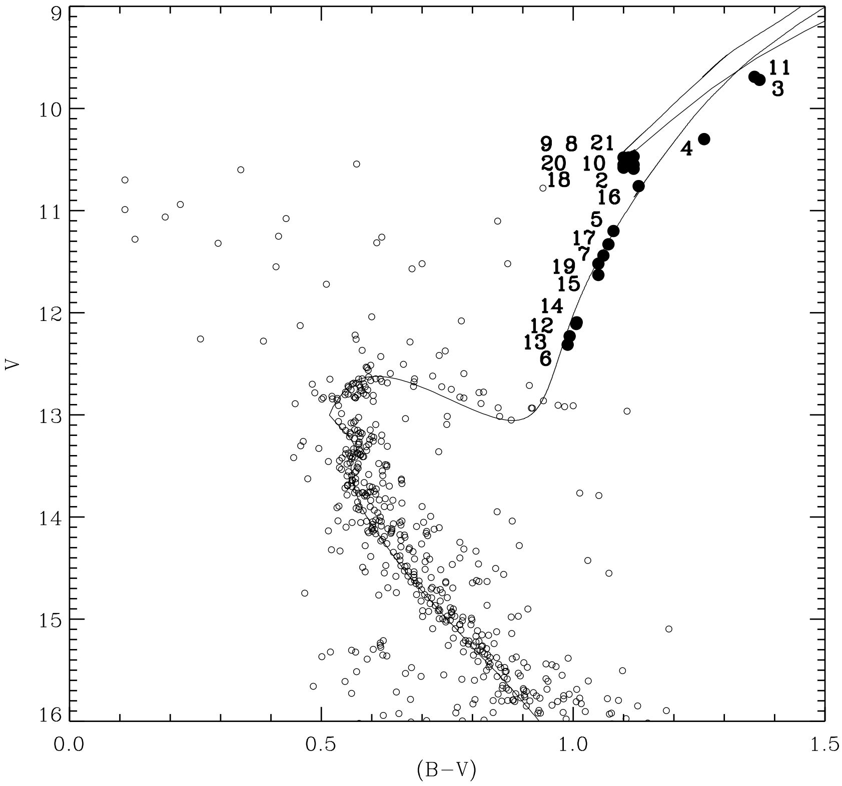

Figure 5.2: Colour-magnitude diagram of the open cluster M67 (photometry by Montgomery et al. (1993)). The red giant target stars are indicated with filled symbols. The numbers correspond to those indicated in Fig. 5.4. The solid line is an isochrone ($(m - M) = 9.7$ mag, Age $= 4.0$ Gyr, $Z = 0.0198$ and $Y = 0.2734$) from the BaSTI database (Pietrinferni et al., 2004).

will measure stellar oscillations in cluster stars. Using high-precision spectrographs from ground to measure radial velocities in red giants is not possible due to the lack of a global network that can achieve high-precision velocities on an ensemble of relatively faint cluster stars. Hence, the only feasible approach is ground-based photometry.

In this investigation we again target M67 using multi-site photometric observations. Unlike the previous studies on this cluster, our primary targets are the red giant stars (see Fig. 5.2). Extrapolating the L/M scaling relation (Kjeldsen & Bedding, 1995) predicts the amplitude of these stars to be in the range 50–500μmag. Although very low, these amplitudes are significantly higher than for the turn-off stars targeted by, e.g., Gilliland et al. (1993). In addition to the red giants, more than 300 stars were observed during the campaign. Many are high-amplitude variables such as W UMa systems, δ Scuti stars and eclipsing binaries, some of which are already known. This campaign provides a unique data set to investigate these stars as well (Bruntt et al., in prep.).

With emphasis on the low-amplitude red giant stars, the main purpose of this paper is to describe the optimisation of time-series data towards achieving the highest possible signal-to-noise in the Fourier spectrum (in amplitude). Further discussion on the extraction of p-modes from the Fourier spectra of these stars will be presented by Stello et al. (2006a). (see Chapter 6).

5.3 Observations

We observed the open cluster M67 from 6 January to 17 February 2004 using nine telescopes (0.6-m to 2.1-m class) in a global multi-site network. The sites were distributed in longitude to allow continuous time-series photometry during the six-week observing program. We were allocated 164 nights of telescope time which, due to bad weather, yielded about 100 clear nights (see Fig. 5.3 and Table 5.1). In the first 18 days we observed 34% of the time and in the following three weeks the coverage was 80%. For the entire campaign (43 days) the coverage was 56%.

The participating telescopes and detectors had different properties and the data sets are therefore rather diverse in terms of field-of-view (FOV), cadence and noise properties. A summary of the observations and the instrument characteristics for each site is given in Table 5.1. We indicate the smallest and largest FOV in Fig. 5.4. The red giant stars are indicated as well.

Observations at each telescope were planned to optimise the signal-to-noise for solar-like oscillations in the red giant stars. We did that by calculating both the noise and the expected oscillation amplitudes (the signal) in different photometric filters. The amplitudes were estimated from Kjeldsen & Bedding (1995, their Eq. 5) and the noise was estimated by photon counting statistics. These calculations showed that the Johnson B and V filters were favourable, but an on-site test was required to establish which of these was superior at each telescope. The observers therefore chose filters based on an initial test at the beginning of the first night. All sites except Kitt Peak chose the V filter. No phase change is seen in the solar oscillations between observations obtained in different filters over the range 400–700 nm (Jiménez et al., 1999). We therefore expect the same adiabatic behaviour for high-order solar-like oscillations in other stars as well. Hence, combining data based on different filters can be done after a simple rescaling of the amplitude, and corresponding adjustment of the weights to preserve the signal-to-noise.

To obtain a noise level which was essentially limited by scintillation and photon noise, it was important to avoid drift on the CCD of the stellar field. The aim was to have each star confined within a few pixels. Not all sites had autoguiding systems and as a result we found very different drift characteristics from site to site (see Fig. 5.5). The images were defocused to obtain a higher duty cycle but we avoided crowding.

The exposure time at each site was adjusted to have star No. 4 just below the saturation limit, which provided a safety margin for the large group of clump stars that were 0.3 mag fainter (see Fig. 5.2). However, the two brighter stars (No. 3 and

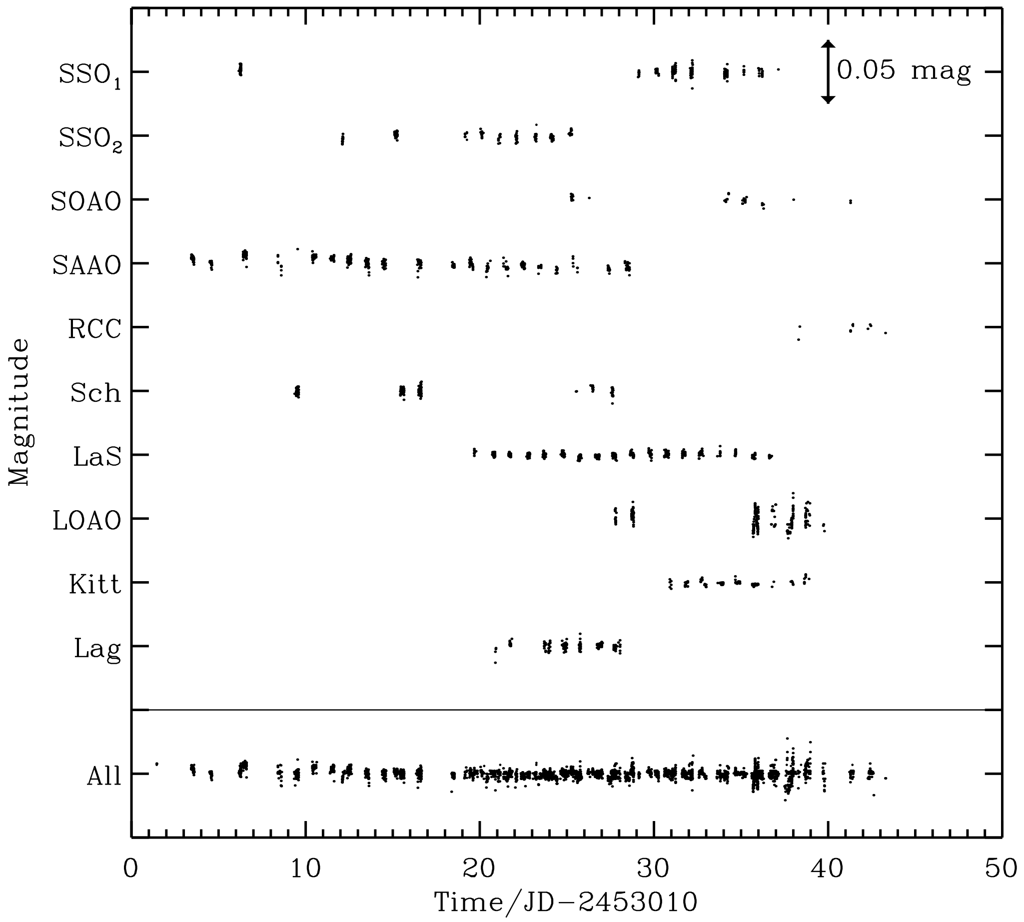

Figure 5.3: Time series of star No. 10 for all sites (after removing outliers and correcting for colour-dependent extinction; see Sect. 5.6.2). The site abbreviations are explained in Table 5.1.

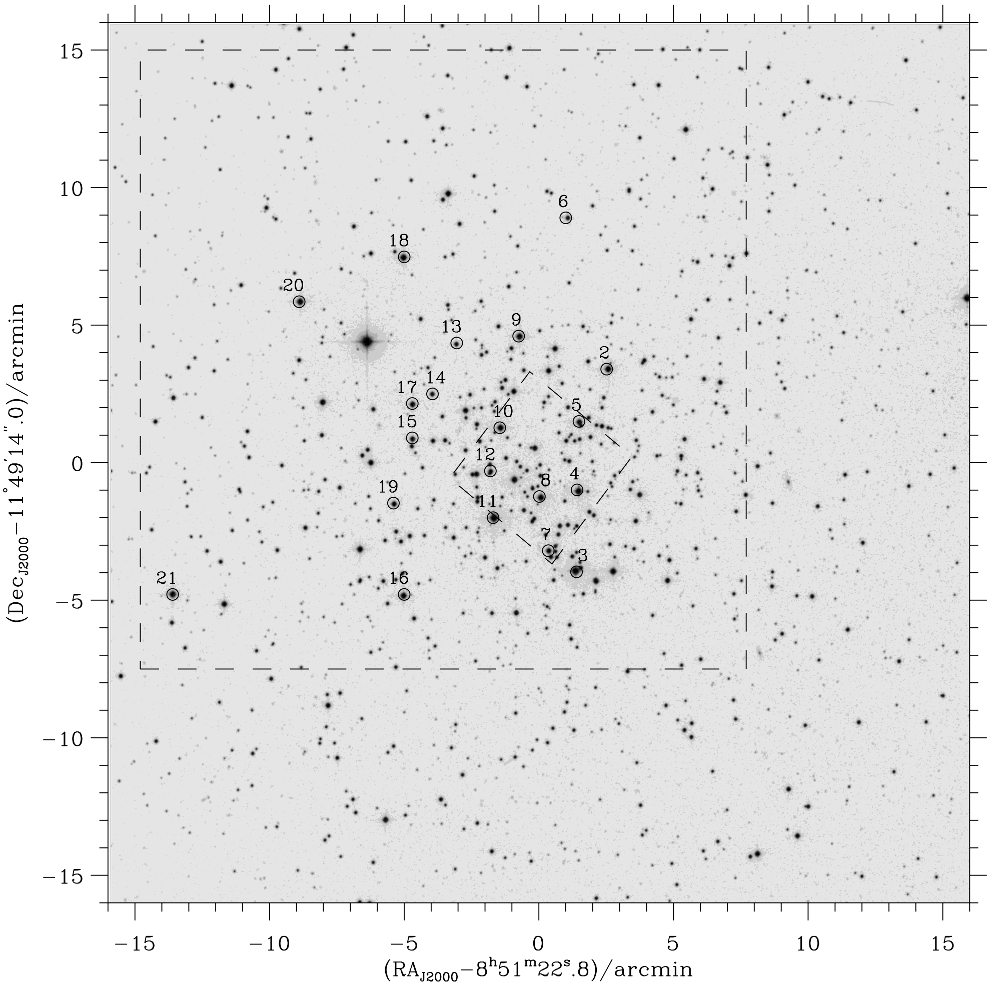

Figure 5.4: M67 field-of-view (FOV). SAAO with the smallest FOV and LOAO with the largest are indicated with dashed squares. The red giant stars are marked with circles. Source: STScI Digitized Sky Survey.

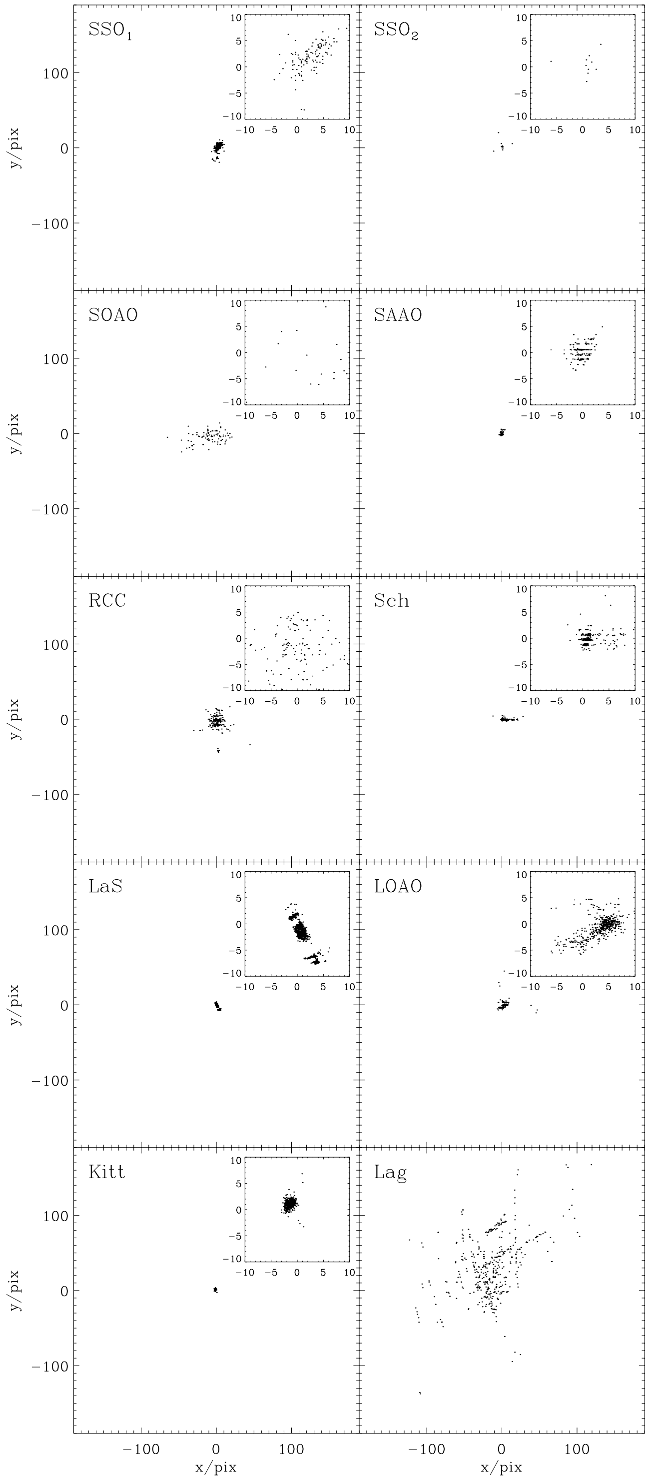

Figure 5.5: The position on the CCD of star No. 10 relative to a reference frame. The insets show the inner 20 by 20 pixels. Although autoguiding is good at LaS, instrument rotation introduced drift during the observing run for stars far from the rotation axis.

Table 5.1: Summary of observations.

Site[a]	Aperture & filter	FOV arc-min	Image scale ″/pix	Obs. time /hours	N_{exp}	Median cadence /sec	Exp. time /sec	Duty cycle /%	night alloc.	night good
SSO_1	1.0m V	14.0	0.38	43.0	2205	62	30	48	16	9
SSO_2	1.0m V	14.0	0.60	51.0	1157	144	30	21	17	10
SOAO	0.6m V	20.5	0.60	33.6	467	240	120	50	17	7
SAAO	1.0m V	6.0	0.31	112.9	2595	149	80	54	28	22
RCC	1.0m V	7.0	0.29	23.6	722	89	70	79	14	5
Sch	0.6m V	17.0	1.10	31.3	1584	53	35	66	16	6
LaS	1.5m V	13.5	0.39	109.0	3945	90	24	27	22	18
LOAO	1.0m V	22.5	0.66	41.8	2886	46	12	26	14	7
Kitt	2.1m B	10.0	0.30	75.5	1563	172	52	30	11	9
Lag	1.0m V	14.0	0.41	46.4	1320	114	20	18	9	7
Total				561.1	18444				164	100

[a] Site abbreviations and observers are:
SSO_1 (Wide Field Imager at Siding Spring Observatory, Australia, Z.E.D., D.S., A.P.J. and L.L.K.);
SSO_2 (Imager at Siding Spring, A.P.J., J.N. and D.S.);
SOAO (Sobaeksan Optical Astronomy Observatory, Korea, S.-L.K., J.-A.L. and C.-U.L.);
SAAO (South Africa Astronomical Observatory, T.A. and H.R.J.);
RCC (Ritchey-Chrétien-Coudé at Piszkéstető, Konkoly Observatory, Hungary, J.N.);
Sch (Schmidt at Piszkéstető, Z.C. and R.S.);
LaS (La Silla Observatory, Chile, H.B., T.H.D.);
LOAO (Mt. Lemmon Optical Astronomy Observatory, Arizona, Y.B.K. and J.-R.K.);
Kitt (Kitt Peak National Observatory, Arizona, R.L.G.);
Lag (Mt. Laguna Observatory, California, C.S. and M.Y.B.).

11) were therefore often saturated. Due to their expected long oscillation periods (Stello et al., 2006a, see Chapter 6), on time scales similar to typical instrumental drift, the results on these stars were likely to provide only limited scientific output. Keeping these two stars above the saturation limit resulted in lower noise for the stars at the base of the red giant branch (stars 6, 13, 12, 14) which were more likely to produce useful results.

5.4 Calibration

We calibrated each CCD image using four steps:

1. overscan subtraction (not all CCDs had an overscan region),
2. subtraction of bias (the bias levels were stable enough to use a single master bias image for each CCD),
3. correction for non-linearity (see Sect. 5.4.1),
4. flat-fielding to correct for pixel-to-pixel variations in the quantum efficiency (we used one master flat field for each CCD; for Kitt Peak and the RCC this was based on dome flats, while we used sky flats for all other sites).

We found that the dark current was negligible compared to the read-out-noise for all sites and it was therefore ignored. These four steps were standard except the non-linearity correction, which is described in more detail in the following section.

5.4.1 CCD linearity calibrations

In this project a few target stars were relatively close to the CCD saturation limit, at flux levels for which the non-linear response of the CCD gain could be significant. It is important to correct for these gain variations to attain the high photometric precision required by this project.

Linearity at high flux levels was investigated for all CCDs using a "classical" linearity test. We used an approach similar to that described by Gilliland et al. (1993). The method measures relative variations in the CCD amplifier gain, rather than absolute calibration in terms of e^{-}/ADU. Flat-field images were taken sequentially with increasing exposure time, interleaved with reference images; e.g. 3 s, 10 s, 3 s, 10 s,$\cdots$, 3 s, then followed by 3 s, 20 s, 3 s, 20 s,$\cdots$, 3 s, until the final series, in which the longer exposures were almost saturated. The reference images allowed instabilities of the light source to be measured and removed. In some cases, however, the flat-field lamp varied on time scales too short to be sampled and a correction could therefore not be made. The mean counts in the flat-field image, scaled according to the exposure time, were plotted versus the mean counts. Images with the same exposure time were grouped to form a single point, with an uncertainty equal to the group rms. In Fig. 5.6 we show the results of the linearity tests for all CCDs. Saturation occurred at 65536 ADU except for the Schmidt, where it was at 16384 ADU. From Fig. 5.6 (upper right panel) we see that non-linearity can introduce variability in the stellar time series up to several percent in non-photometric conditions (variable atmospheric transparency). Using ensemble photometry (Sect. 5.5) will, however, reduce this effect if the ensemble stars are roughly of equal colour and luminosity. We decided to correct for non-linearity for all sites except the Schmidt, which did not show measurable non-linear effects, and Laguna, where we only had measurements of the gain variations up to approximately 30000 ADU, which was significantly lower than the intensity levels of most target stars. For LOAO, the data did not justify a description of the gain variation to be higher than a first-order polynomial fit, although a few points could indicate that higher-order features were present. The linearity calibration of the data from La Silla was based on a method described in the following section, hence no fit was applied to the data shown in Fig. 5.6.

We obtained calibration images at La Silla for a new and more elegant method for determining the linearity properties. This method provides a much more precise determination of the CCD gain variations, which we will compare with the classical method in the next section.

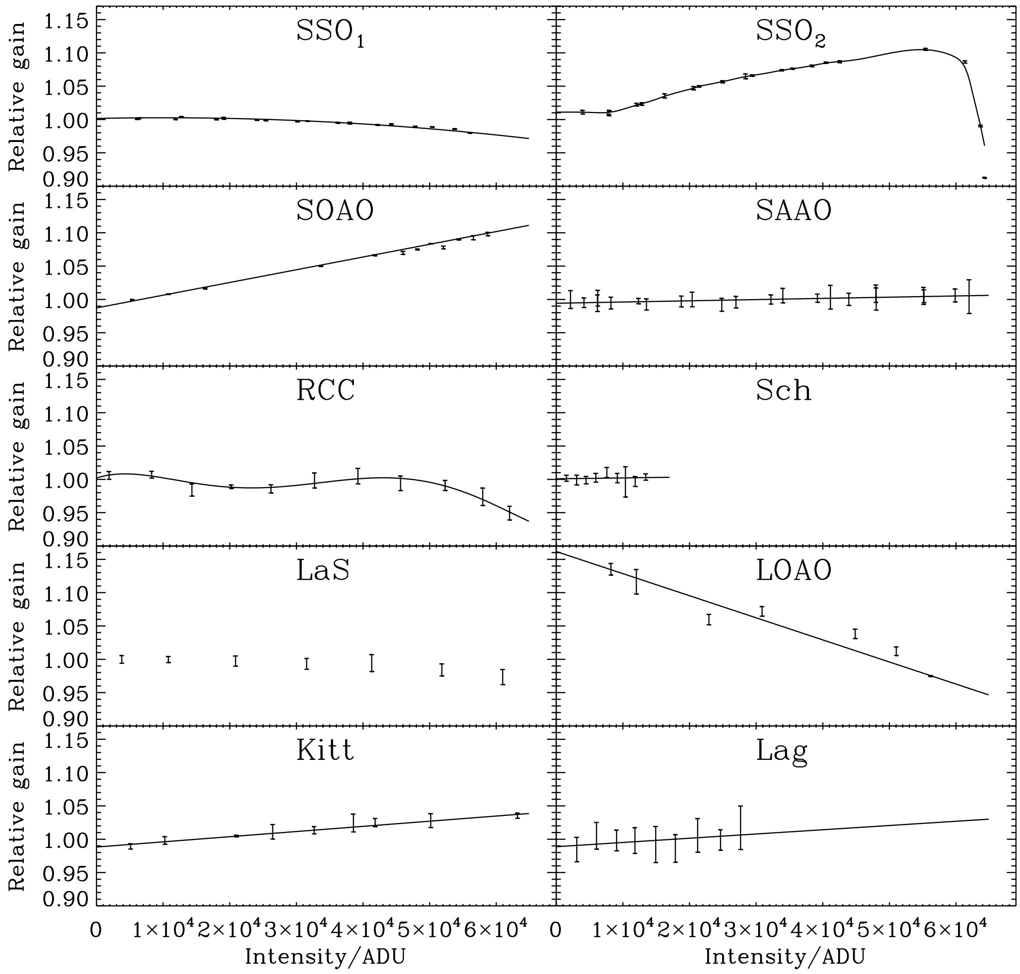

Figure 5.6: Classical linearity tests for all CCDs. For SSO_1, SSO_2 and SAAO two separate tests have been merged. Error bars are plotted as 3×rms to make them visible. The solid lines are polynomial fits used to correct the data for non-linearity.

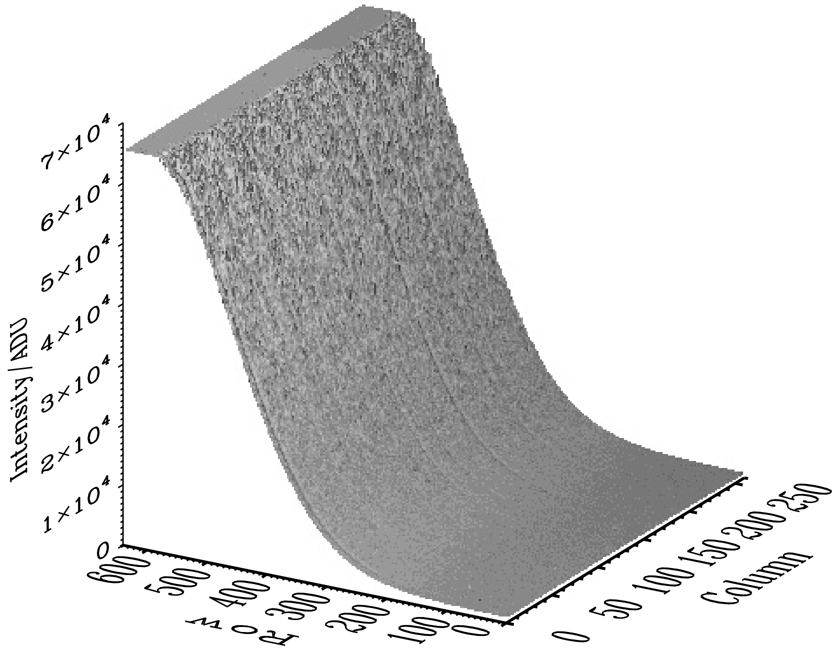

Figure 5.7: Linearity flat field of the longest exposure, 410 s (see text). The flat plateau at high row numbers is due to the digital saturation of the CCD.

Ultra-high-precision method

The basic concept of the method described in this section was first outlined by Baldry (1999) and Knudsen (2000), and was developed into a fully applicable method by Stello (2002). Like the classical method, this method measures relative variations in the CCD amplifier gain using flat-field images of different exposure times, but it differs by using flat fields that have a strong gradient e.g. by using a grism. Each flat field showed a large smooth variation in light level from approximately the bias level to a significant fraction of the saturation limit, with the longest exposure reaching saturation (see Fig. 5.7). The advantage of this method is that the effect from instabilities in the light source used to obtain the flat fields is very small, because we are sampling a large range (in the longest exposures the entire range) of the CCD gain response in a single exposure. The resulting measurement precision of the gain variations is several orders of magnitude better than the classical method. Further, this method requires relatively few images to achieve high precision, making it very efficient.

We obtained spectral flats using the DFOSC spectrograph on the Danish 1.54-m telescope (La Silla). Light variation in one direction across the CCD was achieved using a grism to disperse the light from the slit illuminated by an internal telescope calibration lamp (Fig. 5.7). A series of images were acquired in the following way: 3×30 s, 3×130 s, 3×30 s, 3×250 s, 3×30 s, 3×370 s, 3×30 s, 3×390 s, 3×30 s, 3×410 s, 3×30 s. The control exposures of 30 s enabled long-term drift in the flat

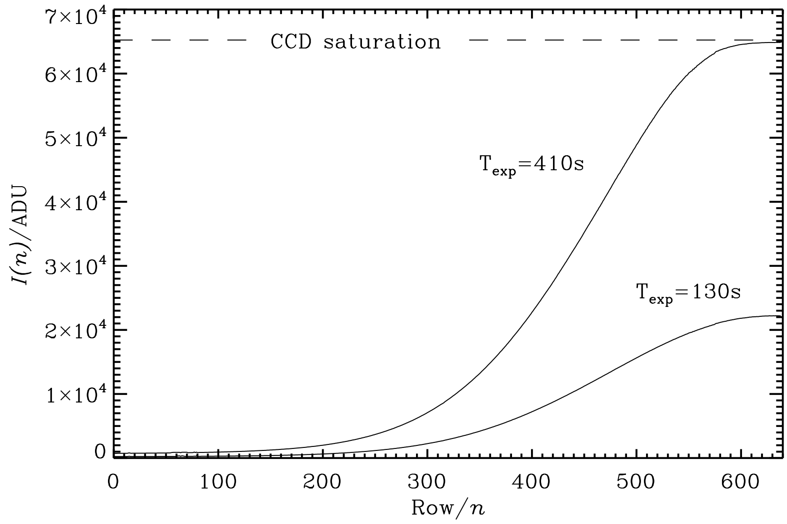

Figure 5.8: Two intensity curves of different exposure times, 410 s and 130 s (see text). The flat part of the 410 s exposure at high row number is due to saturation of the CCD.

field-lamp to be removed. Although this improves the precision, it is not critical. After subtraction of overscan and bias, we corrected for the long-term drift of the flat-field lamp and made an average (master) flat field for each exposure time. We then collapsed each master flat field by averaging in one direction to obtain one dimensional *intensity curves*, as shown in Fig. 5.8.

Due to non-linear effects in the CCD, the intensity we measure in the nth row is:

$$I(n) \quad = \quad T_{\rm exp} \cdot S(n) \cdot g(I(n)), \tag{5.1}$$

where $T_{\rm exp}$ is the effective exposure time in seconds (after correcting for dead-time of the shutter and short-term fluctuations in the light source), $g(I(n))$ is the CCD amplifier gain as a function of the measured intensity and S defines the shape of the intensity curves, hence $S(n)$ expresses the intensity in the nth row from a 1-s exposure. Although the actual gain variations are a function of the received flux, we assume the CCD amplifier has a well-defined output signal for every input signal.

From two intensity curves with different exposure times, say 410 s and 130 s, we constructed the relative curve

$$\frac{I_{\rm 410s}(n)}{I_{\rm 130s}(n)} = \frac{410\,{\rm s}}{130\,{\rm s}} \cdot \frac{g(I_{\rm 410s}(n))}{g(I_{\rm 130s}(n))}, \tag{5.2}$$

where we have corrected for shutter dead-time and verified that the shape S was stable. In Fig. 5.9 (top panel) we show the curve $I_{\rm 410s}(n)/I_{\rm 130s}(n)$ versus $I_{\rm 410s}(n)$, which we call a *gain-ratio curve*. At each intensity, I_1, this curve shows the gain

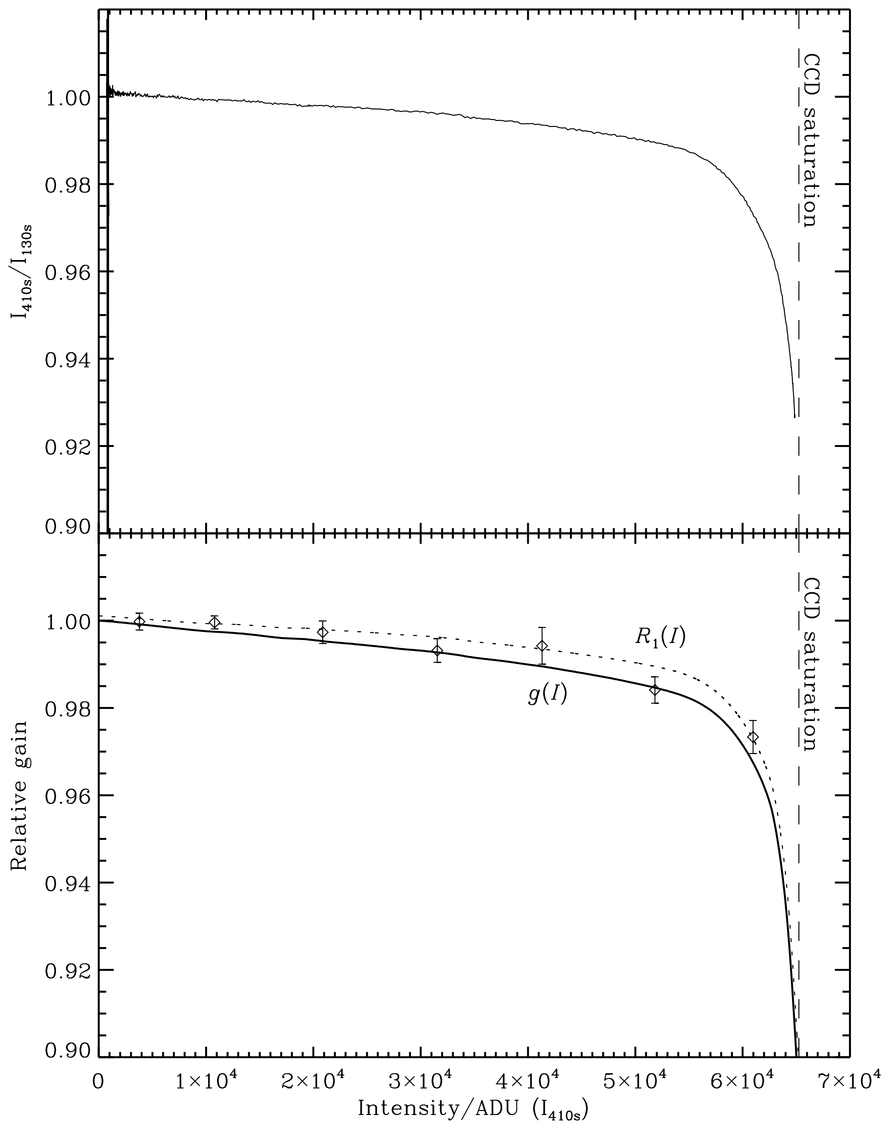

Figure 5.9: **Top panel:** Gain-ratio curve based on two intensity curves of different exposure time (410 s and 130 s). **Bottom panel:** Inversion from smoothed gain-ratio curve $R_1(I)$ (dotted) to final gain-curve $g(I)$ (solid). For comparison, the measurements from the classical method (Fig. 5.6, LaS) and their error bars (1× rms) are indicated. The uncertainty on $g(I)$ is of the order 10 ppm. The smoothing of $R_1(I)$ introduces a systematic error in $g(I)$ of roughly 1% near the saturation limit because the curve is steep.

ratio, $g(I_1)/g(I_2)$, where $I_2 = I_1 \cdot 130\,\mathrm{s}/410\,\mathrm{s}$. Thus, finding $g(I)$ for any intensity level requires inversion of the gain-ratio curve in an iterative process.

We started out using a smoothed version of the measured gain-ratio curve, which we denoted $R_1(I)$, as a first estimate for the actual underlying gain curve $g(I)$ (see Fig. 5.9, bottom panel). Then, assuming $g_1(I) = R_1(I)$, we computed a new gain-ratio curve, $R_2(I) = g_1(I)/g_1(I \cdot 130\,\mathrm{s}/410\,\mathrm{s})$ for all I. The new estimate for the gain was then corrected by the relative deviation between R_1 and R_2 according to $g_2(I) = \frac{R_1}{R_2} g_1(I)$, etc. This iterative process stopped when R_i matched the measured R_1 and the corresponding $g_i(I)$ was the desired gain curve. Before smoothing the measured gain-ratio curve (Fig. 5.9, top panel) we removed the noise at low intensities (0–1000 ADU) by replacing it with a linear fit to the data points from 1000 to 10000 ADU. In the example shown, the gain-ratio curve is very similar to the final gain curve. However, this is not a feature of the method, but is due to the gain characteristics of the particular CCD amplifier.

To ensure that all features in the gain were detected, we examined gain-ratio curves based on different exposure-time ratios. If a feature, say a bump in the CCD gain, is periodic for increasing intensity and hence repeated at all pairs of intensities (I_1, I_2) related as $I_2 = I_1 \cdot 410\,\mathrm{s}/130\,\mathrm{s}$, it will not show up in the gain-ratio curve based on 410 s and 130 s exposures (or any combination with the same exposure-time ratio). Our gain curves based on flat fields with different exposure-time ratios, all showed an excellent match within the errors.

In Fig. 5.9 (bottom panel) we compare our new method with results from the classical method for La Silla (Fig. 5.6). The two methods are in agreement with each other, but the series of flat-field images for our new method is significantly faster to obtain, provides the relative gain for all intensities and has a precision more than 100 times better. However, it requires temporally stable but spatially variable illumination of the CCD (e.g. spectral flat fields) which is not possible at every telescope.

5.5 Ensemble photometry

The goal of this project is to measure relative light variations with very high precision. Hence, our approach is to obtain differential photometry taking advantage of the ensemble of stars in the FOV. Using an ensemble allows the effects from atmospheric variations, common to all stars, to be removed from the time series. The number of stars in the ensemble ranged from 116 (in the small FOV of SAAO) to 358 (for LOAO). We used the MOMF photometry package (Kjeldsen & Frandsen, 1992) to extract the photometry from the reduced images. It calculates differential photometric time series by subtracting a reference time series which is a weighted average based on all ensemble stars. The weight given to each star is $1/\mathrm{rms}^3$, which ensures that stars with a high rms in their time series, such as faint stars and high-amplitude variables, are strongly suppressed. MOMF was developed especially to produce time-series photometry from large numbers of images (in particular defocused images) of semi-crowded fields, similar to those obtained in this campaign. It combines PSF and aperture photometry. We chose 10 stars, not necessarily the same for each site, to define the shape of the point-spread-function (PSF). These were all non-crowded bright stars, i.e. mostly red giant stars and a few bluer stars of the same luminosity (see Fig. 5.2). MOMF allows multiple apertures and calculates the total rms, $\sigma_{\rm total}$, and the internal rms, $\sigma_{\rm internal}$, of the time series based on each aperture. The first is just the rms of the time series while the latter is calculated as

$$\sigma^2_{\rm internal} = \frac{1}{2(N-1)} \sum_{i=1}^{N-1} (m_i - m_{i+1})^2 \,, \tag{5.3}$$

where N is the number of points in the time series and m_i is the magnitude of the ith point in the series. For each site and each star we chose the aperture with the lowest $\sigma_{\rm total}$ in the time series.

5.6 Improving the photometry

5.6.1 Iterative sigma clipping

To improve the overall quality of the data we first removed outliers. We calculated the point-to-point deviation of each data point, i, relative to its neighbouring points as

$$d_i = m_i - 0.5 \cdot (m_{i+1} + m_{i-1}) \,, \tag{5.4}$$

where m is the magnitude. We then removed data points, m_i, for which $d_i > 3.0\sigma_i$, where σ_i is the rms of d within a 3-hour interval around data point i. This was done in an iterative loop until no more points were removed, which converged after a few iterations. We illustrate the underlying statistics of this process in Fig. 5.10, which shows that the cumulative distribution of d/σ has a significant non-white tail of deviating data points. Choosing the threshold is a trade-off between removing outliers and keeping statistically valid points. The threshold was chosen so that roughly 85% of the removed points were real outliers and 15% were valid points. We tested our sigma clipping method on generated random noise to verify that it was not too drastic in terms of removing extreme points from pure Gaussian noise. It removed less than 0.2%, corresponding to about 35 points of the time series from the entire campaign. This should be compared to the approximately 250 data points removed in total from the real time series for each star. Results of the sigma clipping on the real data were further verified by visual inspection of diagrams similar to what is shown in Fig. 5.11.

5.6.2 Colour extinction

The data from Kitt Peak, which were the only ones obtained in the Johnson B filter, showed clear residual trends. This arises from an uncorrected wavelength dependence in the extinction (see Fig. 5.11). These trends were visible in the red

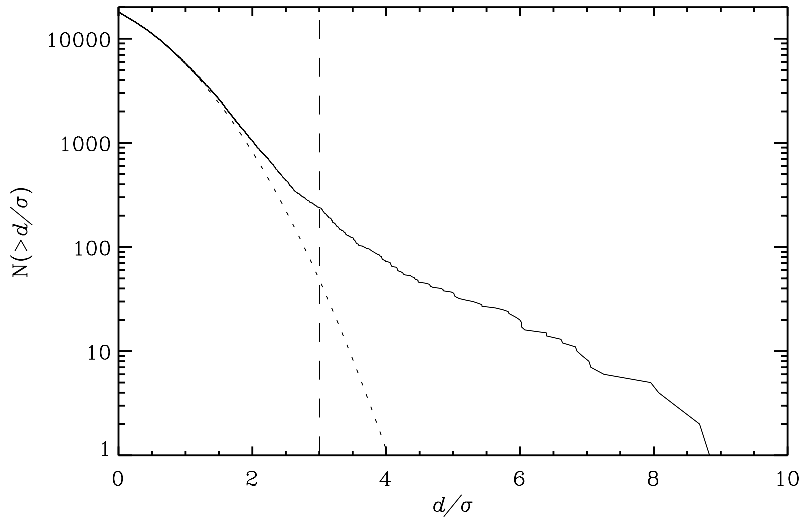

Figure 5.10: Cumulative distribution of d/σ (solid line) for the entire data set of star No. 10. The dotted line is an analytical Gaussian distribution for comparison, and the dashed line indicates the threshold for our sigma clipping process.

giant stars because the reference time series calculated by MOMF was dominated by bluer stars. Decorrelating the differential photometry against airmass still left a lot of variation in the time series. Including more parameters, such as sky background, in the decorrelation process would affect the expected stellar signals significantly, which we verified with simulations. Subtracting a smoothed version of the individual time series was also too harsh on the stellar signal. Instead we tried using only the red giant stars themselves in the ensemble. For some targets this provided good results but for most it did not. Adding the much fainter main-sequence stars of similar colour to increase the sample size did not improve the results. We finally chose to correct the colour term from the MOMF differential photometry in a similar way to Gilliland & Brown (1988). For each image we fitted a linear relation to the target stars:

$$m_k - \langle m_k \rangle = a_0 + a_1 \cdot (B - V)_k, \tag{5.5}$$

where m_k is the magnitude of star k, $(B-V)_k$ is its colour and $\langle m_k \rangle$ is the average of the time series. To correct star j, we subtracted a fit that did not include the star itself

$$m_{\mathrm{corr},j} = m_j - \langle m_j \rangle - (a_0 + a_1 \cdot (B - V)_j). \tag{5.6}$$

This was to prevent stellar signal being removed by the process, which we have confirmed with simulations. There were 12 red giant target stars with low noise levels, hence 11 stars were used in each fit, with a typical range of 1.00–1.25 mag in $B - V$ colour. In Fig. 5.11 (bottom right) we show the time series of one night of star No. 10 before and after correction of the colour term. The other sites showed

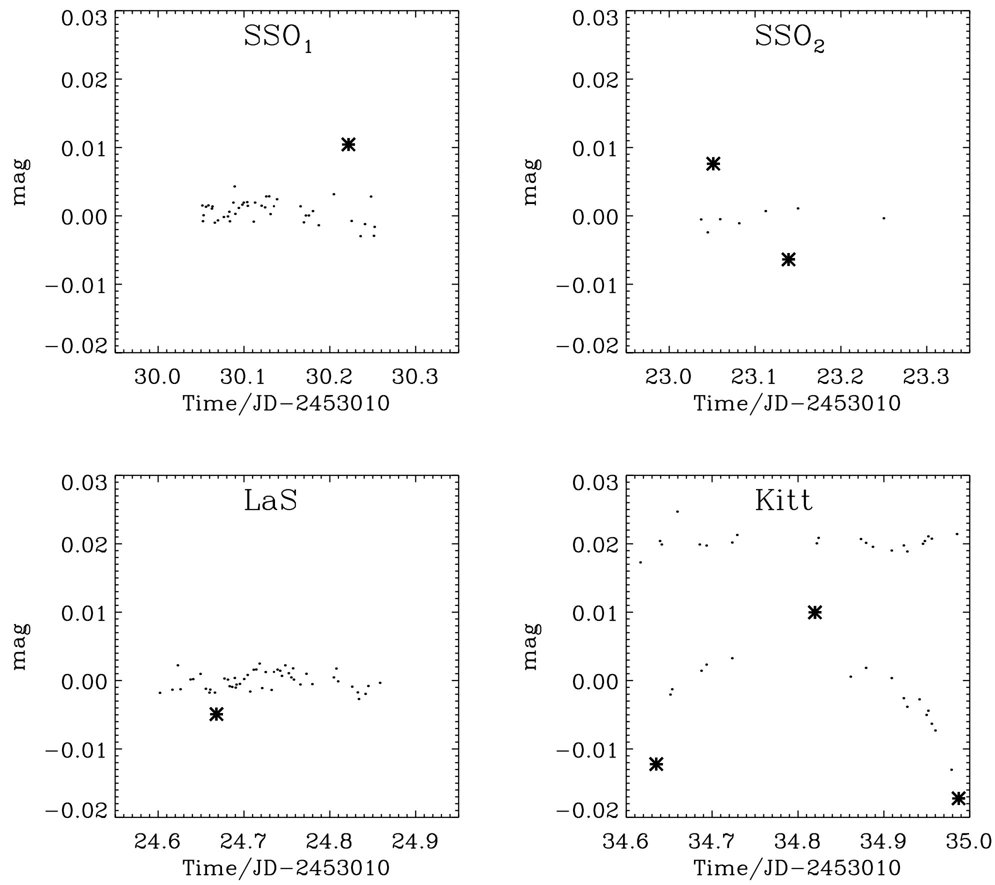

Figure 5.11: Photometric time series of star No. 10 for single nights from four sites. Outliers found by iterative sigma clipping are indicated with asterisks. The strong trend in the Kitt Peak data (curved time series) is due to colour-dependent extinction not removed by the ensemble normalisation of MOMF. The corrected time series, has been shifted upwards by 0.02 mag for clarity (see Sect. 5.6.2).

weak effects from extinction, but these trends were not consistent from star to star or night by night, and the noise levels in the Fourier spectra did not improve if we performed the same correction as in the case of Kitt Peak. We therefore decided not to correct for residual extinction in the differential photometry at any other site.

5.6.3 Weight calculation

To be able to detect solar-like oscillations in the red giant stars, it is crucial that we obtain noise levels as low as possible in the frequency range where the oscillations are expected to appear in the Fourier spectra of the time series. It is known that weighting time series of inhomogeneous data can significantly improve the final signal-to-noise level (Handler, 2003). The important thing is that the final weights represent the true variance of the noise on time scales similar to the stellar signal one wants to detect. We will use a weighting scheme similar to that used by Butler et al. (2004) and Kjeldsen et al. (2005) to minimise the noise in amplitude, which includes the following two steps:

1. Calculate weights from the point-to-point variance ($w_i = 1/\sigma_i^2$).
2. Adjust the weights to obtain agreement between the noise at the relevant frequencies in the Fourier spectrum and the weights as being represented by $w_i = 1/\sigma_i^2$.

(1) The point-to-point variance was not supplied by the photometric reduction package and these values had to be estimated from the local variance of the time series. We estimated the local scatter σ_i ($=\sqrt{\text{variance}}$) for each data point i as the rms of the d array (Eq. 5.4) using a moving boxcar. The width of the boxcar (5 hours) was chosen to minimise the noise (in amplitude) in the weighted Fourier spectrum. The spectrum was calculated as a weighted discrete Fourier Transform following the description of Frandsen et al. (1995). Having first removed outliers, we prevented good data from being down-weighted by bad neighbouring points during this process.

(2) We then adjusted the weights night by night to be consistent with the noise level (in amplitude), σ_{amp}, between 300–900 μHz in the Fourier spectrum, requiring that $\sigma_{\text{amp}}^2 \sum_{i=1}^{N} \sigma_i^{-2} = \pi$ (Eq. 3 in Butler et al., 2004). The idea is that noise in this frequency range would have components that affect the noise at slightly lower frequency as well where we expect the stellar signal to be for the red giant stars. Choosing a frequency range within the expected range of the stellar signal would effectively down-weight stellar signal, which is not desired.

In Fig. 5.12 we plot our final estimates of σ_i, including the adjustment multipliers for each night shown in the insets. The maximum adjustment was a factor of ~ 2. For some sites, the noise in the final Fourier spectra in the range 300–900 μHz decreased by up to 20% after adjusting weights on a night-by-night basis, but in most cases it was a 5–10% decrease. We see that σ_i vary significantly during the observing run at many sites. For example, the range at Kitt Peak is 0.54–3.61 mmag (see Fig. 5.12).

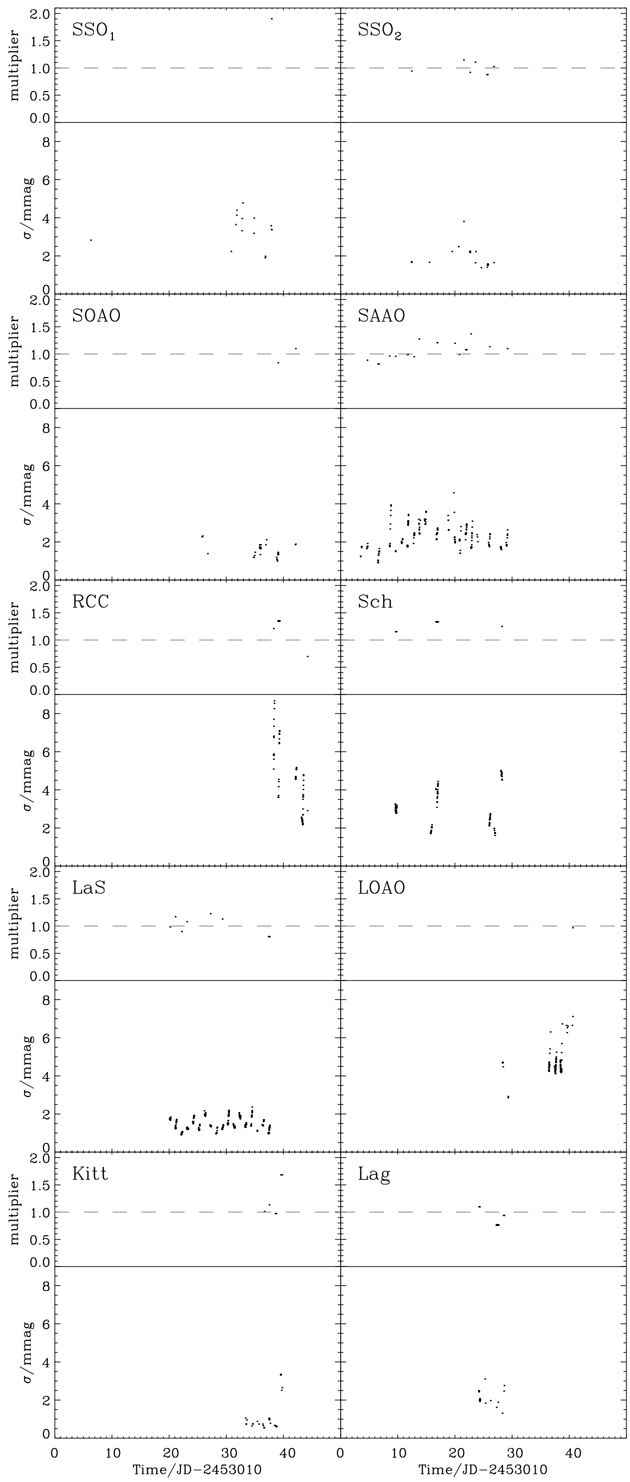

Figure 5.12: Scatter for each site for star No. 10. The insets show the multiplication factor used to adjust σ_i for each night (see Sect. 5.6.3). The horizontal axes are the same as in the main panels.

5.7 Error budget

To establish whether the noise in the final time series was at the irreducible lower limit dominated by photon noise and atmospheric scintillation, we estimated each noise component and compared with the measured noise in the time series in a similar way as in previous investigations by Gilliland & Brown (1988, 1992a) and Gilliland et al. (1993).

Our total error budget comprised scintillation and counting statistics within the aperture; the latter included stellar light, sky background, level in the flat field, and CCD read-out-noise. The contribution from scintillation was estimated as

$$\sigma_{\mathrm{scint}} = 0.09 D^{-2/3} \chi^{3/2} \exp(-h/8000\,\mathrm{m}) T_{\mathrm{exp}}^{-1/2} , \tag{5.7}$$

(Kjeldsen & Frandsen, 1992, their Eq. 3) using the factor of proportionality from Young (1967), D the telescope diameter in centimetres, χ the airmass, h the elevation of the telescope in metres and T_{exp} the exposure time in seconds per image. For the counting statistics we used the expression from Kjeldsen & Frandsen (1992, their Eq. 31):

$$\sigma_{\mathrm{count}}^2 = \frac{2 \ln 2}{W^2 \pi e_{\mathrm{ff}}} + \frac{1}{e_{\mathrm{star}}} + \pi r_{\mathrm{AP}}^2 \frac{e_{\mathrm{sky}} + \sigma_{\mathrm{RON}}^2}{e_{\mathrm{star}}^2} , \tag{5.8}$$

where W is the full-width-at-half-maximum of the stellar PSF in pixels, e_{ff} is the number of electrons per pixel in the flat field, e_{star} is the number of electrons from the star within the aperture, r_{AP} is the radius in pixels of the aperture, e_{sky} is the number of electrons per pixel in the sky background and σ_{RON} is the CCD read-out-noise (per pixel) in electrons. Combining σ_{scint} and σ_{count} finally gives the estimated scatter

$$\sigma_{\mathrm{est}} = (\sigma_{\mathrm{scint}}^2 + \sigma_{\mathrm{count}}^2)^{1/2} . \tag{5.9}$$

The estimated scatter was dominated by scintillation for the brighter stars and by photon noise for the fainter stars. The magnitude at which the noise changed from being scintillation-dominated to photon-noise-dominated was in the range $V =$ 10.5–12.0 mag but different from site to site. At a few sites the contribution to the counting statistics from the flat field was similar to the scintillation and hence significant for the brighter stars. In general, the read-out-noise and sky background could be neglected.

In Table 5.2 we give the measured internal scatter (Eq. 5.3) for each red giant star based on the full time series, which shows the overall quality of the data from star to star and from site to site. In general, star No. 10 had the lowest noise except for SAAO and LOAO. To compare with the estimated scatter (Eq. 5.9) we have, for each star and each site, measured the internal scatter (Eq. 5.3) for the best night, and the results are shown in Fig. 5.13. There are other sources of noise not included in our error budget, which can explain why some stars fall significantly above the line of proportionality. Saturation of the CCD will increase the noise significantly. For several sites, stars No. 3, 4 and 11 were affected by saturation, which explains their higher noise levels. Close neighbouring stars can introduce higher noise in the

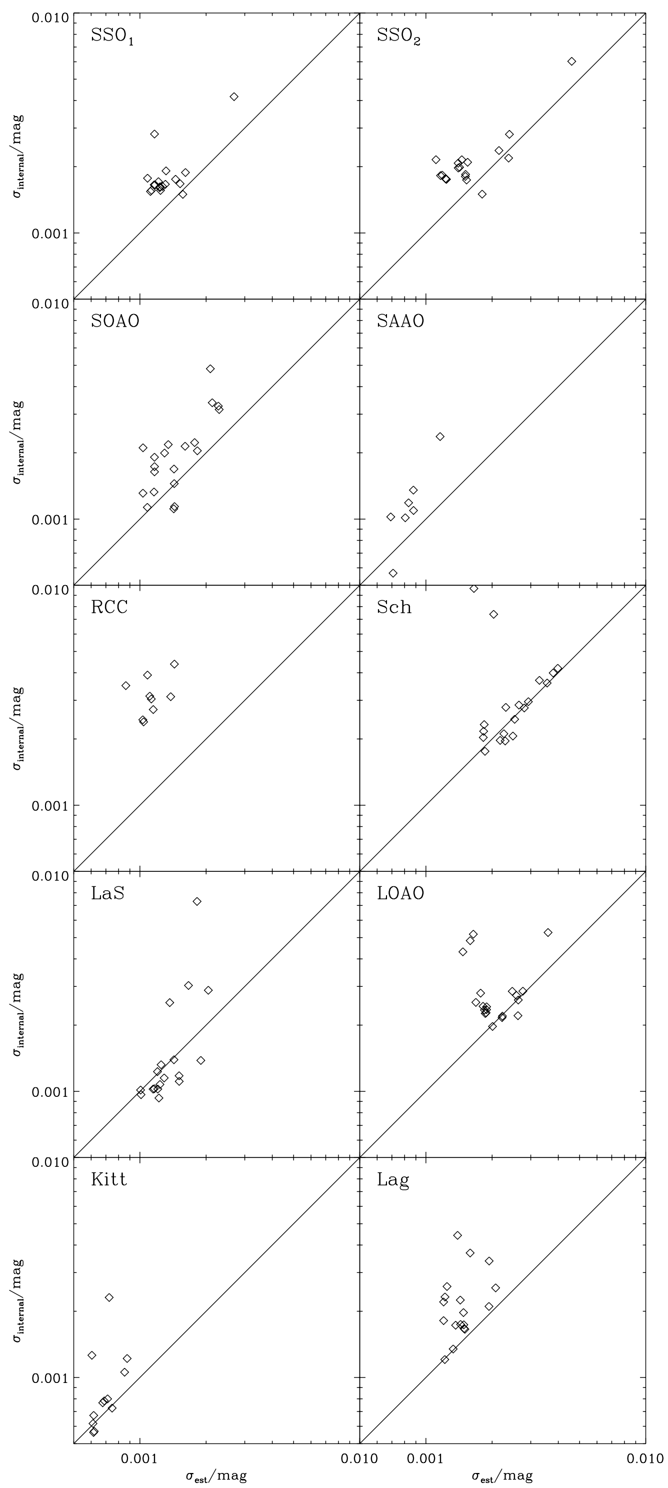

Figure 5.13: Measured scatter versus estimated scatter for the red giant stars. The measured scatter is $\sigma_{\rm internal}$ (Eq. 5.3) of the relative photometry based on the best night for each star. The estimated scatter is calculated from Eq. 5.9, which gives relative errors, and is scaled by a factor of 1.086 ppm/μmag to put it on the magnitude scale.

Table 5.2: Internal scatter σ_{internal} in mmag of the red giant stars (sorted by their luminosity). The internal scatter is based on the entire time series using Eq. 5.3 after ensemble normalisation, sigma clipping and, for Kitt Peak, correction for colour-dependent extinction (see Sect. 5.6). Star No. 10 has the lowest scatter at all sites except SAAO and LOAO.

No.	m_V	SSO_1	SSO_2	SOAO	SAAO	RCC	Sch	LaS	LOAO	Kitt	Lag
3	9.72	16.84	23.69	3.46	–	–	13.11	3.86	8.18	–	7.75
11	9.69	26.76	10.28	3.38	4.11	–	16.81	1.73	10.10	–	2.88
4	10.30	2.37	9.55	1.87	1.84	5.16	2.83	1.39	3.33	2.77	2.94
21	10.47	–	–	20.63	–	–	–	–	3.77	–	–
8	10.48	2.37	8.13	2.00	1.70	3.96	2.58	1.38	2.95	1.46	2.51
9	10.48	2.73	9.44	1.81	–	–	3.16	1.42	2.94	1.22	3.24
10	10.55	2.35	2.02	1.44	2.04	3.87	2.31	1.36	3.09	1.11	1.95
20	10.55	2.86	17.43	2.85	–	–	2.93	1.58	3.13	–	5.57
2	10.59	2.54	4.83	2.09	–	–	2.91	1.63	2.92	1.28	4.09
18	10.58	3.24	16.04	4.62	–	–	3.12	1.41	3.07	–	7.64
16	10.76	2.96	9.69	3.16	–	–	3.28	1.55	7.93	–	5.15
5	11.20	2.44	5.22	3.04	1.82	4.68	3.68	1.96	2.63	1.62	2.78
17	11.33	2.72	5.25	2.47	–	5.66	3.22	3.50	2.45	1.91	3.20
7	11.44	2.83	13.65	2.83	2.00	6.73	3.31	1.54	2.57	1.61	17.38
19	11.52	2.91	4.86	2.85	–	–	3.20	1.64	2.95	4.81	3.60
15	11.63	2.50	4.54	3.42	–	5.33	3.54	6.22	2.66	1.83	2.88
14	12.09	3.02	5.40	3.96	–	4.75	4.22	1.66	3.23	3.59	2.90
12	12.11	5.39	8.88	8.47	3.98	8.19	4.30	8.36	6.04	–	9.02
13	12.23	3.49	8.74	5.41	–	–	4.75	3.72	3.32	3.53	3.26
6	12.31	–	13.16	5.02	–	–	6.24	–	3.47	–	–

photometry. Star No. 12 has three close neighbouring stars and at most sites it suffers from excess noise. If a star is located close to a bad column on the CCD the noise will also increase, which we see in some cases.

In summary, for stars that are not affected by crowding, saturation or bad columns, we generally see noise levels limited by photon and scintillation noise on the best nights. At one site (RCC) the noise is larger than estimated by a factor of two, which is unexplained.

5.7.1 Noise comparison with previous campaigns

The first campaign aimed at detecting solar-like oscillations in M67 was carried out by Gilliland & Brown (1988), who used a 0.9-m telescope on two nights. Noise levels to ~ 1.5 mmag per minute integration were attained for non-saturated stars ($m_V \gtrsim 12$ mag). Later, Gilliland et al. (1991) observed M67 for two weeks from five sites using 0.6-m to 1.1-m class telescopes. The lowest rms in the time series of the non-saturated stars ($m_V \gtrsim 12.5$) was 0.88 mmag per minute integration after high-pass filtering the data. For comparison, our best 0.6-m site (SOAO) showed an internal scatter (comparable to the rms of high-pass filtered data) down to ~ 1.6 mmag per minute integration, and the best 1.0-m site (SAAO) showed ~ 1.2 mmag per minute integration. A final, but direct, comparison can be made between our Kitt Peak observations of the red giant No. 10 with those obtained by Gilliland & Brown (1992a) using the same telescope in a similar campaign. Star No. 10 (No. 7 in Gilliland et al., 1991) was one of their targets with the lowest noise, which was 0.43 mmag per minute integration after high-pass filtering and decorrelating the data. In comparison we obtained 0.50 mmag (based on the internal scatter, but without any high-pass filtering or decorrelation).

To summarise, we find noise levels as good as in previous studies based on similar size telescopes. However, this campaign has provided significantly longer time series (six weeks compared to a maximum of two weeks) with better coverage than earlier comparable campaigns, which implies lower noise levels in the final Fourier spectra.

5.7.2 Noise in the Fourier spectra

The noise levels in the Fourier spectra obtained by our weighting scheme were 20–30 μmag for the red giant stars that were not affected by excess noise from crowding, saturation or bad pixels. We therefore expect to be able to detect oscillations in the Fourier spectrum with S/N $\geqq 4$. However, the detection threshold depends very much on the mode lifetime, which is unknown for these stars (Stello et al., 2006c), and will require extensive simulations to quantify. This analysis will be published in a subsequent paper.

In Fig. 5.14 we show the Fourier spectrum of star No. 10, which is one of the best, to illustrate the noise level we have obtained. The noise level, indicated with the white line, is the average in the range 300-900 μHz. The detailed pulsation analysis of all red giants will be presented by Stello et al. (in prep.).

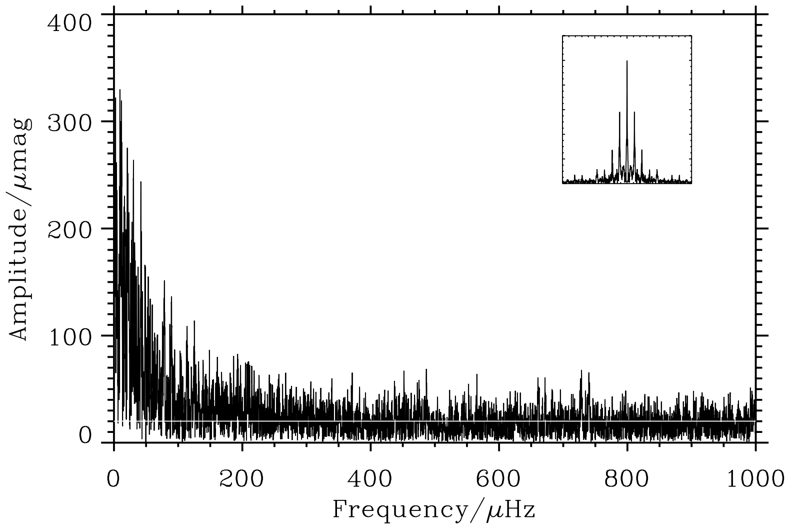

Figure 5.14: Fourier spectrum of star No. 10 (in amplitude). The white line indicates the noise level in the range 300–900 μHz. The inset shows the spectral window, which is on the same frequency scale as the main panel. Each data point has been weighted according to the weighting scheme described in Sect. 5.6.3.

5.8 Conclusions

We have collected 100 telescope nights of photometric multi-site data of the open stellar cluster M67 over a six-week period. The focus of this paper was the discussion of our approach towards achieving the highest signal-to-noise ratio for the very low amplitude (50–500 μmag) solar-like oscillations in the red giant stars. This included our careful reduction of the CCD images to obtain the lowest possible noise in the time-series data, and our weighting scheme to reduce the noise level in the Fourier spectrum.

We have obtained a point-to-point scatter in the time-series photometry down to about 1 mmag for most sites, while the largest participating telescope reached 0.5 mmag (Fig. 5.13). These values are similar to those from previous campaigns on M67 by Gilliland & Brown (1988), Gilliland et al. (1991) and Gilliland & Brown (1992b) which all used telescopes of similar size but for shorter time spans (maximum two weeks). Comparison of our best nights with known noise terms demonstrates that the attained point-to-point scatter is consistent with irreducible terms dominated by photon and scintillation noise for all sites but one (RCC), which shows extra noise of unknown origin (Fig. 5.13). With these scatter values, our weighting scheme provided a mean noise level in the Fourier spectra of approximately 20 μmag (in amplitude), which would allow us to detect solar-like oscillations in the red giant stars with S/N $\geqq 4$ assuming L/M-scaling.

Acknowledgments

This work was partly supported by the IAP P5/36 Interuniversity Attraction Poles Programme of the Belgian Federal Office of Scientific, Technical and Cultural Affairs. This paper uses observations made from the South African Astronomical Observatory (SAAO), Siding Spring Observatory (SSO) and the Danish 1.5m telescope at ESO, La Silla, Chile. This research was supported by the Danish Natural Science Research Council through its centre for Ground-Based Observational Astronomy, IJAF.

Chapter 6

M67: Oscillations in red giant stars

The content of this chapter has been submitted to Monthly Notices of the Royal Astronomical Society in 2006 by Dennis Stello in collaboration with Hans Bruntt, Hans Kjeldsen, Tim Bedding, Torben Arentoft, Ronald Gilliland, János Nuspl, Seung-Lee Kim, Yong Beom Kang, Jae-Rim Koo, Jeong-Ae Lee, Chris Sterken, Chung-Uk Lee, Henrik Jensen, Andrew Jacob, Róbert Szabó, Søren Frandsen, Zoltán Csubry, Zoe Dind, Yacine Bouzid, Thomas Dall and László Kiss. (Stello et al., MNRAS, 2006).

I conducted all the analysis. In addition Hans Bruntt has made an independent reduction of the data, which is included and clearly specified. For further details about the campaign please consult the first page of the previous chapter. I was supervised by Hans Kjeldsen, Tim Bedding.

6.1 Abstract

Measuring solar-like oscillations in an ensemble of related stars, such as in a stellar cluster, holds promise of testing stellar structure and evolution more stringently than just fitting parameters to single field stars. The most ambitious attempt to pursue these prospects was by Gilliland et al. (1993) who targeted 11 turn-off stars in the open cluster M67 (NGC 2682), but the oscillation amplitudes were too small ($< 20\,\mu$mag) to obtain unambiguous detections. Like Gilliland et al. (1993) we also aim at detecting solar-like oscillations in M67, but we target red giant stars with expected amplitudes in the range 50–500 μmag and periods of 1 to 8 hours. We analyse our recently published photometry measurements obtained during a six-week multi-site campaign using ten telescopes around the world. The Fourier spectra of the time series are compared with simulations and estimated properties of the stellar oscillations. Noise levels in the Fourier spectra to 27 μmag are obtained for single sites while the combined data reaches 19 μmag. In a few cases we see excess of power in the Fourier spectra. We further see a shift in frequency of power when the stars are analysed as an ensemble. The detected excess power is consistent with expectations from stellar signal. However, our results are limited by apparent high levels of non-white noise, which cannot be separated from the stellar signal. Conclusions are therefore tentative.

6.2 Introduction

The first clear detection of solar-like oscillations in a red giant star (ξ Hya; Frandsen et al., 2002; Stello, 2002) opened up a new part of the Hertzsprung-Russell diagram to be explored with asteroseismic techniques. Following that discovery, detailed analysis of ξ Hya has been performed (Teixeira et al., 2003; Stello et al., 2004, 2006c, see Chapters 3 and 4) and new discoveries of oscillations in similar stars have emerged (ε Oph and η Ser; Barban et al., 2004; De Ridder et al., 2006). These results are all based on radial velocity measurements of high precision ($\sigma \sim 2\,$m/s) but from non-continuous observations, which imposes large ambiguities on the results (Stello et al., 2006c; De Ridder et al., 2006, see Chapter 4). With oscillation periods of a few hours, these stars require a time base of roughly one month, which can only be obtained on small telescopes. But the current lack of high-precision spectrographs on small telescopes makes a multi-site campaign impossible.

However, using photometry makes it feasible to incorporated many 1–2m class telescopes in a multi-site campaign, and it furthermore provides the possibility to observe many stars, like in a cluster, simultaneously. Detecting oscillations in a series of cluster stars potentially increases the power of the asteroseismic measurements due to the extra constraints provided by the common parameters of the cluster stars (age and composition). Until recently, there has been no such ground-based photometric campaign aimed at detecting solar-like oscillations in red giant stars. A number of attempts have been made to detect oscillations in more Sun-like stars (hotter and less luminous) of the open cluster M67 (Gilliland & Brown, 1988; Gilliland et al., 1991; Gilliland & Brown, 1992a), with the most ambitious multi-site effort made by Gilliland et al. (1993). Despite noise levels down to 0.29 mmag per minute integration no unambiguous detections were claimed. In a recent paper Stello et al. (2006b hereafter Paper I; see Chapter 5), we reported observations from a large six-week multi-site campaign also aimed at M67. However, unlike the previous studies our campaign was optimised for the slightly brighter and longer period red giant stars (see Fig. 6.1), and also covered a much longer time span. The long oscillation periods mean that non-white noise such as drift is more crucial for this project than in the previous studies. The data set reported in Paper I (see Chapter 5) was based on very different sites, many with unknown long-term stability performances. A realistic estimate of the final non-white noise in the data could therefore not be obtained prior to observations.

In this paper our main emphasis is on the time-series analysis of the red giant stars (Sect. 6.5), based on the data described in Paper I (see Chapter 5). We report in Sect. 6.3 on an additional independent data reduction method to further obtain lower noise in the Fourier spectra. In Sect. 6.4 we estimate the oscillation characteristics and simulate in Sect. 6.6 the expected outcome for each target without the presence of non-white noise to facilitate the analysis of the observations. We give our conclusions in Sect. 6.7.

6.3 Observations and data reduction

The data are from a global multi-site observing campaign of nine 0.6-m to 2.1-m class telescopes from 6 January to 17 February 2004 (Paper I; see Chapter 5). The photometric time series of those stars within the field-of-view of all telescopes comprises roughly 18000 data points.

After calibrating the CCD images we used the MOMF package (Kjeldsen & Frandsen, 1992), which calculated differential photometry time series of 20 red giants relative to a large ensemble of stars (from 116 to 358 stars, depending on telescope field-of-view). We performed the following three initial steps to improve the signal-to-noise in the final Fourier spectra of the time series: (1) sigma clipping, (2) correcting for colour extinction and (3) calculating weights for each data point. For further details see Paper I (see Chapter 5).

In addition to the time series produced by D.S., as described above, H.B. constructed a normalised time series following the approach of Honeycutt (1992). Normalisation offsets for each data point (CCD image) were based on the raw time series calculated by MOMF (without ensemble normalisation) of the red giant stars. For each target star, the relative photometry was calculated subtracting a reference time series (a combination of the individual time series of all red giants) that did not include the star itself. The weight w given to each star in the ensemble normalisation was calculated as $w = 1/(\sigma_{\rm ptp} + \sigma_{\rm min})$, where $\sigma_{\rm ptp}$ is the local point-to-point scatter and $\sigma_{\rm min} = 1$ mmag is a fixed minimum noise value to prevent a single star with

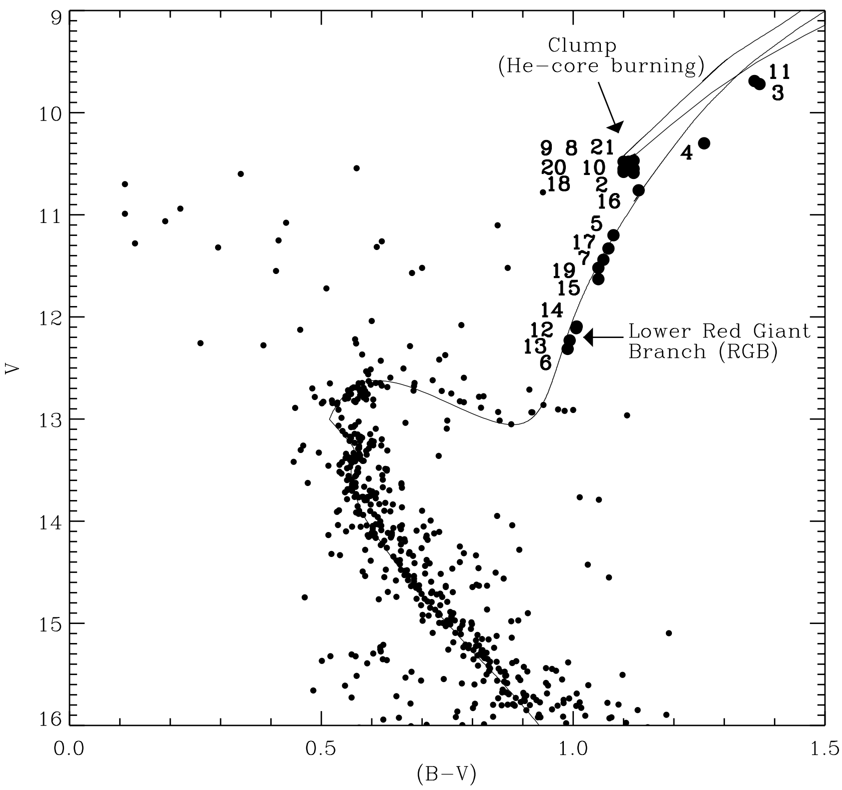

Figure 6.1: Colour-magnitude diagram of the open cluster M67 (photometry from Montgomery et al. (1993)). The target stars are indicated (identifier numbers corresponds to those given in Tables 6.1 and 6.2). The solid line is an isochrone ($(m - M) = 9.7$ mag, Age $= 4.0$ Gyr, $Z = 0.0198$ and $Y = 0.2734$) from the BaSTI database (Pietrinferni et al., 2004).

very low noise from dominating the ensemble normalisation. Using the relatively small homogeneous ensemble comprising only red giants has the advantage of better removing colour-dependent extinction, and hence providing a lower noise level in the Fourier spectrum at low frequencies. However, simulations showed that the reference time series will include stellar oscillations with amplitudes up to 30% of those we want to detect. The stars with the longest periods (hence largest amplitudes) will be the most affected.

In most stars, the two methods produced very similar noise levels in the time series, within 10%. However, on a few stars differences of up to 50% were seen. In the following, we chose the time series for each star and each site with the lowest noise in the Fourier spectrum in the interval 300–900 μHz, which is just outside the frequency range where the stars are expected to oscillate.

6.4 Expected signal

To better interpret our results, we have estimated the characteristics of solar-like oscillations expected in the red giant stars. We scaled the oscillation parameters of the Sun using known scaling relations to predict amplitude, central frequency of excess power and the large frequency separation. These predictions are used in Sects. 6.5 and 6.6 to compare with the observations.

The predicted amplitude in the Johnson V filter ($\lambda_{\rm cen} = 544\,$nm) was derived using the scaling relation by Kjeldsen & Bedding (1995) (using 1 ppm = 1.086 μmag):

$$(\delta L/L)_\lambda = \frac{L/L_\odot(5.1 \pm 0.3)\,\mu\mathrm{mag}}{(\lambda/550\,\mathrm{nm})(T_{\rm eff}/5777\,\mathrm{K})^2(M/M_\odot)}\,. \tag{6.1}$$

These amplitudes were used as a guide while planing the observations. However, recent theoretical studies indicate that the L/M-scaling may over-estimate the amplitude for main-sequence stars and that $(L/M)^{0.7}$-scaling might provide a more realistic prediction (Samadi et al., 2005), which we will take into account in evaluating of our results. We note that extrapolating amplitudes for red giant stars based on these scaling relations is very uncertain, and has so far not been thoroughly tested by calculations of theoretical pulsation models or observations of these stars.

The characteristic frequency domain within which a star is oscillating was estimated as the central frequency of the excess power, which was obtained by scaling the acoustic cut-off frequency of the Sun (Brown et al., 1991)

$$\begin{aligned}\nu_{\max} &= \frac{M/\mathrm{M}_\odot}{(R/\mathrm{R}_\odot)^2\sqrt{T_{\rm eff}/5777\,\mathrm{K}}} \times 3050\,\mu\mathrm{Hz} \\ &= \frac{M/\mathrm{M}_\odot}{L/L_\odot\,(T_{\rm eff}/5777\,\mathrm{K})^{3.5}} \times 3050\,\mu\mathrm{Hz}\,, \end{aligned} \tag{6.2}$$

using $L/L_\odot = (R/R_\odot)^2(T_{\rm eff}/5777\,\mathrm{K})^4$. This scaling relation gives very good agreement with the frequency range of the solar-like oscillations observed in main sequence stars and also in red giants (Bedding & Kjeldsen, 2003).

Finally, we predict the expected frequency spacing, $\Delta\nu_0$, between modes of the same degree in the power spectrum (Kjeldsen & Bedding, 1995)

$$\begin{aligned}
\Delta\nu_0 &= \frac{(M/\mathrm{M}_\odot)^{0.5}}{(R/\mathrm{R}_\odot)^{1.5}} \times (134.92 \pm 0.02)\,\mu\mathrm{Hz} \\
&= \frac{(M/\mathrm{M}_\odot)^{0.5}(T_{\mathrm{eff}}/5777\,\mathrm{K})^3}{(L/L_\odot)^{0.75}} \times (134.92 \pm 0.02)\,\mu\mathrm{Hz}\ .
\end{aligned} \tag{6.3}$$

To calculate these parameters we obtained rough estimates of the stellar mass, luminosity, and effective temperature, which are summarised in Table 6.1. For all stars we adopted a mass of $M = 1.35M_\odot$ corresponding to the mass at the base of the red giant branch for an isochrone with Age = 4.0 Gyr, $Z = 0.0198$ and $Y = 0.2734$ (BaSTI database; Pietrinferni et al., 2004), which matches the cluster colour-magnitude diagram (see Fig. 6.1). This is also in good agreement with the turn-off mass by VandenBerg & Stetson (2004). We derived L and T_{eff} using (V, $B-V$)-photometry of the cluster (Montgomery et al., 1993) and interpolation of the BaSeL grid (Lejeune et al., 1998). We adopted a typical surface gravity for all red giants of log$g$=2.5 (Allen, 1973), [Fe/H]=0.0 in agreement with Nissen et al. (1987), and $(m-M) = 9.7$ mag corresponding to $d = 870$ pc, which is within 5% of previous investigations (e.g Montgomery et al. (1993); VandenBerg & Stetson (2004)). We note that, because the temperature of our target stars are roughly the same, the expected amplitudes are proportional to $1/\nu_{\mathrm{max}}$

$$\left(\frac{\delta L}{L}\right)_\lambda = \frac{1}{\nu_{\mathrm{max}}}\left(\frac{T_{\mathrm{eff}}}{5777\,\mathrm{K}}\right)^{1.5}\frac{550\,\mathrm{nm}}{\lambda}(10.1 \pm 0.8)\,\mathrm{mmag}. \tag{6.4}$$

6.5 Time-series analysis

In Table 6.2 we give for each star the noise levels (in amplitude) in the Fourier spectra measured in two frequency intervals based on single-site data. The noise denoted $\sigma_{1000-3000\,\mu\mathrm{Hz}}$ represent the lowest noise level (white noise), while $\sigma_{300-900\,\mu\mathrm{Hz}}$ is the noise level just outside the expected frequency range of the oscillations. The best data were from La Silla and Kitt Peak, with mean noise levels of roughly 40 μmag for the best stars. The Kitt Peak data had a slightly lower point-to-point scatter but were more affected by extinction and hence showed more drift noise than La Silla. As we seek to optimise the signal-to-noise in the final Fourier spectra (in amplitude) based on the combined data from all sites, the parts from La Silla and Kitt Peak will dominate for most stars.

Due to nightly drifts in the data we saw very strong peaks at 1–4 cycles per day (corresponding to 11.57, 23.15, 34.72 and 46.30 μHz) in the Fourier spectra based on individual sites. Even when combined, the data still showed significant excess power due to these drifts. This was a serious problem because the most promising stars in the ensemble are expected to oscillate in the affected frequency range. We decided to remove ("clean") these specific frequencies using standard

Table 6.1: Properties of red giant target stars.

No	V^a	$B-V$	$L/L_\odot$	$T_{\rm eff}$	$\delta L/L$ μmag[b]		$\nu_{\rm max}$	$\Delta\nu_0$	Cross-ref[c]	P[d]
	mag	mag		K	(L/M)	$(L/M)^{0.7}$	μHz	μHz		%
3	9.720	1.370	250.6	3920	2080	343	3.7	0.7	S978/G8	53/95
11	9.690	1.360	243.5	3960	1980	331	3.9	0.8	S1250/G4	58/95
4	10.300	1.260	87.0	4330	592	142	15.1	2.2	S1016/G5	78/93
21	10.470	1.120	51.9	4727	296	88	34.4	4.2	S1592/	48/92
8	10.480	1.110	50.8	4750	287	86	35.8	4.3	S1010/G2	82/96
9	10.480	1.100	50.2	4772	281	84	36.8	4.4	S1084/	80/92
10	10.550	1.120	48.2	4727	275	83	37.0	4.4	S1279/G7	79/92
20	10.550	1.100	47.1	4772	264	81	39.2	4.6	S1479/	76/95
2	10.590	1.120	46.4	4727	265	81	38.4	4.6	S1074/	74/91
18	10.580	1.100	45.8	4772	256	79	40.3	4.7	S1316/	73/95
16	10.760	1.130	40.3	4703	232	74	43.5	5.0	S1221/	92/90
5	11.200	1.080	25.4	4815	140	52	74.8	7.6	S1054/G9	93/64
17	11.330	1.070	22.4	4835	122	47	86.0	8.4	S1288/	94/96
7	11.440	1.060	20.2	4854	109	44	96.9	9.2	S989/G12	95/95
19	11.520	1.050	18.7	4873	101	41	106.0	9.9	S1254/	94/95
15	11.630	1.050	16.9	4873	91	38	117.3	10.6	S1277/	95/95
14	12.094	1.007	11.2	4945	58	28	187.3	15.2	S1293/	96/93
12	12.110	1.006	11.0	4947	57	28	190.2	15.4	S1264a/G15	0/75
13	12.230	0.993	9.9	4966	51	26	213.2	16.8	S1305/	96/95
6	12.313	0.989	9.2	4971	48	24	230.2	17.8	S1103/	95/—

[a] Photometry from Montgomery et al. (1993).

[b] Estimated amplitudes based on both (L/M) and $(L/M)^{0.7}$ scaling. Note that 1 ppm = 1.086 μmag.

[c] IDs starting with an S are from Sanders (1977), while G are from Gilliland et al. (1991).

[d] Membership probabilities are from Zhao et al. (1993) and Sanders (1977) respectively.

All targets have high probabilities in Girard et al. (1989) (P > 95%).

iterative sine-wave fitting, on a site-by-site basis. Compared to a classic high-pass filter with a smoothly varying response function, this method has the advantage that it removes only a small amount of power and only in a very limited and well-defined frequency range, which was important because of the expected low frequencies of the oscillations in the stars. However, our approach still implies that any quantitative analysis of the stellar excess power and the search for regular spaced peaks cannot be done for stars oscillating in the frequency range 0–50 μHz, which includes the clump stars (No. 21, 8, 9, 10, 20, 2 and 18; see Fig. 6.1 and Table 6.1). The mean noise levels in the Fourier spectra at 300–900 μHz were reduced by 2–13% (in amplitude) as a result of this cleaning process. We did not decorrelate the time series against external parameters (e.g. airmass, sky background, position on CCD) because we regarded this as having dramatic and uncontrolled effects on the time series on time scales similar to the expected stellar oscillations.

After the initial cleaning of the dominant low frequency noise peaks, we calculated the Fourier spectra of the combined data to search for excess power. In Fig. 6.2 we show the spectra of the best twelve stars (noise below 50 mmag in the frequency range 300–900 μHz). Three other stars (No. 16, 19 and 20) fulfill this criteria but have been omitted due to significantly higher noise levels compared to stars of similar brightness. The solid white line in each panel of Fig. 6.2 is the smoothed spectrum, which was obtained by smoothing twice, with a boxcar width of 30 μHz followed by 10 μHz. The frequencies where we expect the stellar oscillations are indicated with the white downward-pointing arrow head, and the dotted horizontal line shows $(3\sigma_{300-900\,\mu\mathrm{Hz}})^2$. We note that the detection threshold for stochastically excited and damped oscillations in a frequency region where the noise is not white depends on both mode lifetime and the characteristics of the noise source. Both are unknown in the present case, making a quantitative statement about upper limits of the oscillation amplitudes difficult.

6.5.1 Location of excess power

We expect the oscillation modes to be located at lower frequencies for the more luminous stars (see Eq. 6.2 and Table 6.1). To search for general trends in the Fourier spectra, we grouped the stars according to luminosity. We formed three groups (but excluded star No. 4): the clump stars (5 stars), the stars between the clump and the lower RGB (4 stars), and the lower RGB stars (2 stars) (see Fig. 6.1). For each group we averaged their Fourier spectra and smoothed the final spectrum. Smoothing was done twice. First, with a wide boxcar (width=100 μHz) to smear out humps of power originating from the individual spectra to better illustrate the overall distribution of power within each group. We then used a second boxcar (width=10 μHz) to smooth small point-to-point variations in the final plot. The result, shown in Fig. 6.3, confirms the general trend of shifting power excess, in agreement with expectations (see arrows in Fig. 6.3).

Table 6.2: Mean noise level (in μmag) in Fourier spectrum for two frequency intervals (stars plotted in Fig. 6.2 are in boldface). Site abbreviations are: SSO_1 (Wide Field Imager at Siding Spring Observatory, Australia); SSO_2 (Imager at Siding Spring); SOAO (Sobaeksan Optical Astronomy Observatory, Korea); SAAO (South Africa Astronomical Observatory); RCC (Ritchey-Chrétien-Coudé at Piszkéstető, Konkoly Observatory, Hungary); Sch (Schmidt at Piszkéstető); LaS (La Silla Observatory, Chile); LOAO (Mt. Lemmon Optical Astronomy Observatory, Arizona); Kitt (Kitt Peak National Observatory, Arizona); Lag (Mt. Laguna Observatory, California).

No	SSO_1	SSO_2	SOAO	SAAO	RCC	Sch	LaS	LOAO	Kitt	Lag
					$\sigma_{1000-3000\,\mu\mathrm{Hz}}, \sigma_{300-900\,\mu\mathrm{Hz}}$					
3	291, 372	298, 311	400, 535	–, –	–, –	809, 1090	481, 585	349, 545	–, –	604, 746
11	2930, 3325	231, 235	334, 366	294, 417	–, –	1096, 1737	102, 120	476, 688	–, –	152, 196
4	99, 110	138, 134	147, 137	43, 48	248, 386	139, 144	39, 41	164, 268	62, 91	123, 173
21	–, –	229, 260	359, 394	–, –	–, –	227, 302	–, –	149, 153	–, –	–, –
8	101, 87	155, 155	117, 134	48, 52	171, 295	117, 111	37, 38	146, 229	47, 59	118, 152
9	94, 95	154, 174	129, 141	–, –	–, –	120, 130	40, 42	194, 315	27, 31	118, 157
10	82, 69	97, 122	119, 115	68, 78	164, 284	113, 124	37, 40	147, 217	34, 42	93, 124
20	86, 83	115, 119	152, 157	–, –	–, –	150, 196	39, 39	258, 465	–, –	191, 336
2	96, 101	135, 157	148, 151	–, –	–, –	138, 138	53, 52	150, 202	32, 38	125, 166
18	77, 78	122, 134	187, 176	–, –	–, –	120, 136	33, 36	247, 451	–, –	156, 280
16	92, 106	167, 164	259, 239	–, –	–, –	150, 150	46, 48	289, 312	–, –	184, 295
5	96, 87	160, 171	213, 222	45, 47	219, 324	165, 186	57, 59	108, 128	43, 51	114, 175
17	100, 103	126, 148	199, 194	–, –	255, 341	162, 168	101, 122	154, 303	36, 43	163, 225
7	108, 95	159, 178	250, 235	66, 81	319, 518	171, 170	46, 50	122, 160	39, 47	511, 810
19	113, 103	160, 180	219, 202	–, –	–, –	182, 180	55, 64	142, 235	138, 230	153, 191
15	109, 91	153, 145	237, 273	–, –	331, 453	175, 225	163, 198	101, 116	45, 53	131, 184
14	109, 94	178, 192	330, 340	–, –	414, 563	205, 237	50, 51	117, 129	63, 67	131, 185
12	231, 240	486, 567	719, 692	140, 156	471, 470	198, 227	276, 317	371, 587	–, –	224, 299
13	111, 104	187, 192	349, 336	–, –	–, –	224, 227	111, 128	96, 119	74, 85	148, 196
6	–, –	231, 260	351, 378	–, –	–, –	232, 289	–, –	161, 186	–, –	–, –

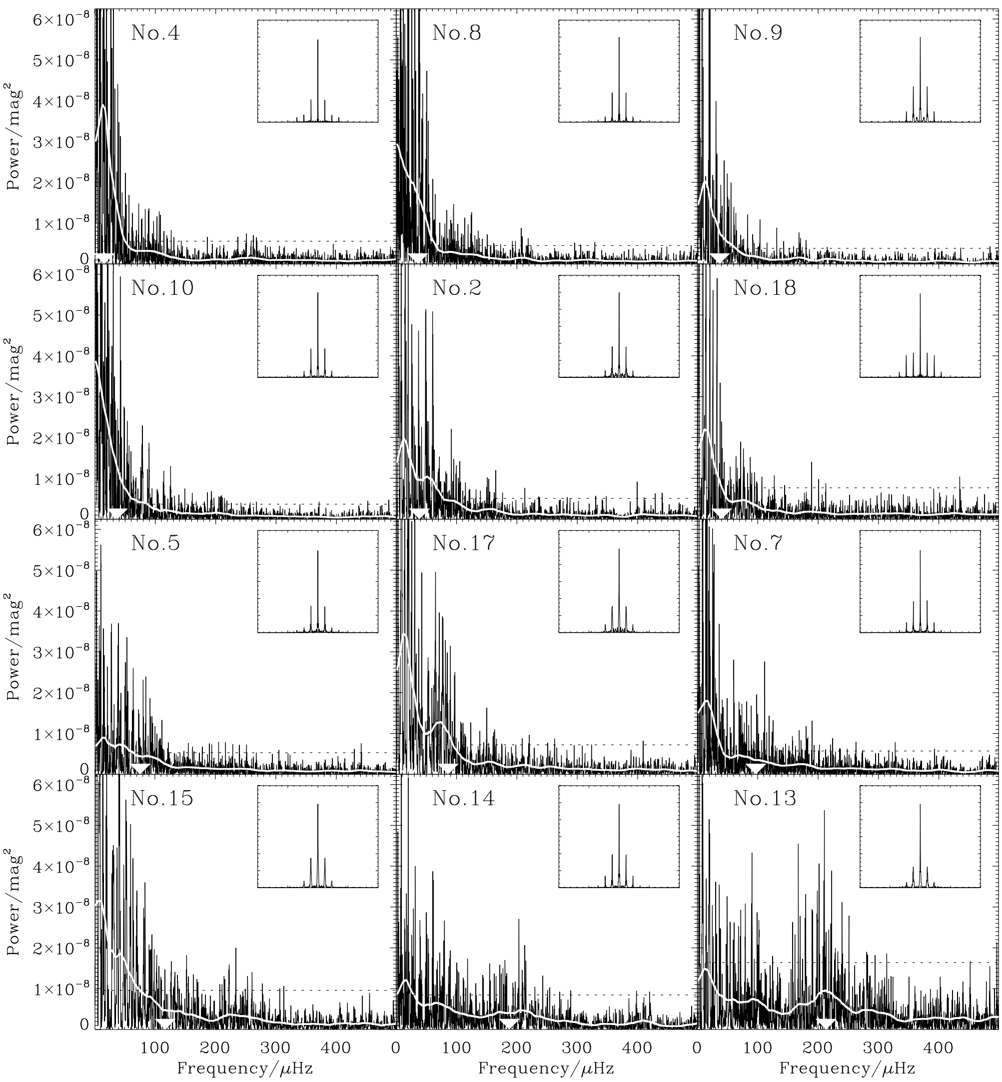

Figure 6.2: Fourier spectra of red giant stars (identifier shown in each panel). The solid white line is the smoothed spectrum, and the white arrow head indicates where we expect the stellar excess power (Table 6.1). The dotted horizontal line shows $(3\sigma_{300-900\,\mu\text{Hz}})^2$. The inset shows the spectral window on the same frequency scale as the main panel.

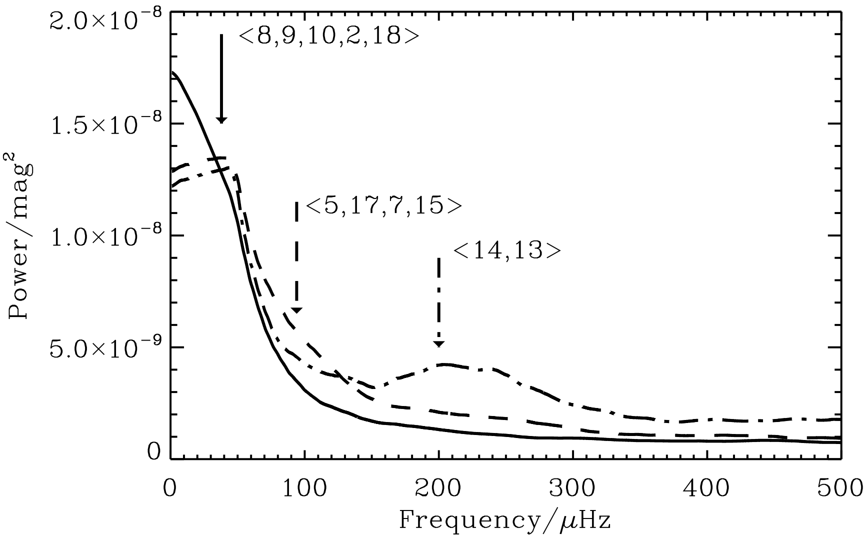

Figure 6.3: Average power distribution as a function of frequency for three groups of stars. The arrows show the mean position of the expected excess power for the stars (stellar IDs in brackets), which have been used to calculate the corresponding power distribution (see text for details).

We investigated whether the observed power shift could have been artificial produced by the reduction methods. (i) We inspected Fourier spectra and weights from each site and concluded that the power shift was not an artifact originating from high weights given to a few sites. (ii) We reanalysed the data without removing the peaks at 11.57, 23.15, 34.72 and 46.30 μHz, but saw the same trend, just with more power at low frequencies. (iii) Finally, we investigated whether our data reduction could introduce such a trend due to more pronounced drift noise for brighter and cooler stars. The best comparison stars for this purpose were the blue stragglers, which had similar brightness to the red giants and hence similar input parameters for the extraction of the photometry (for details see Kjeldsen & Frandsen, 1992 and Paper I; see Chapter 5). However, their colours were very different from the red giants and from star to star, and only a few blue stragglers were observed at most sites. The blue stragglers showed different levels of excess power at low frequencies from star to star, but no causal relation could be found.

In summary, we found no evidence for a non-stellar source that could explain the observed pattern of excess power. The observed behaviour is exactly as expected for oscillations. However, due to the lack of a good ensemble of reference stars, similar to the red giant sample, we could not exclude with certainty that the photometric data reduction might have caused the shift as a result of more drift noise for more luminous and cooler stars.

6.5.2 Amplitude of excess power

To search for further evidence of solar-like oscillations, we measured the amount of excess power above the background noise, with special focus on the stars with expected oscillations above 50 μHz, which were less likely to be affected by our initial clean process. The noise level in the power spectrum, as a function of frequency, $\sigma(\nu)$, was estimated using the following expression: $\sigma(\nu) = \frac{a}{\nu^{1.5}} + \sigma_{\rm wn}$ (in power). First, we measured the white noise, $\sigma_{\rm wn}$, as the mean level in the frequency range 300–900 μHz. Then, having fixed $\sigma_{\rm wn}$, we calculated a requiring that the integral of $\sigma(\nu)$ in the range 50–900 μHz should equal that of the power spectrum.

In a few cases, we see a hump of excess power above the fit at the expected frequency range of the stellar oscillations. Assuming this is real, we estimated the amplitude per mode based on the approach of Kjeldsen et al. (2005). These amplitude estimates are independent of the mode lifetime, but require an assumption of the number of modes that are excited. We have estimated the amplitudes for two scenarios: (1) only radial modes are excited and, (2) if there are three additional non-radial modes per radial mode, neglecting any difference in mode visibilities due to varying cancellations in full-disk observations. Power spectra (Fig. 6.2) were divided by the integrated power of the spectral window to obtain power density. The background noise was subtracted and the resulting power density was multiplied by the mean mode spacing ($\Delta\nu_0$ for only radial modes, and $\Delta\nu_0/4$ for both radial and non-radial modes). We then took the square root to convert to amplitude. The results are shown in Fig. 6.4.

No pulsation models have been published for these stars to investigate whether non-radial modes are expected. Calculations by Christensen-Dalsgaard (2004) and Dziembowski et al. (2001) on more massive and luminous stars suggest that only radial modes are excited to observable amplitudes in red giant stars. However, stars No. 13 and 14 are expected to oscillate at frequencies that are significantly higher than for typical red giant stars, and are similar to those of subgiants. Observations of the subgiants η Boo (Kjeldsen et al., 2003) and ν Ind (Carrier et al. in prep) clearly shows evidence of both radial and non-radial modes.

For star No. 17, the measured amplitude is in good agreement with L/M-scaling if we assume only radial modes are excited, while additional non-radial modes are required to match the prediction from $(L/M)^{0.7}$-scaling. However, the fit to the noise is quite uncertain at these low frequencies. The hump of power, although more pronounced after cleaning the four dominant low frequency peaks, was also present before cleaning and so cannot be explained by simple drift noise.

Star No. 14 shows excess power that is consistent with L/M-scaling only if both radial and non-radial modes are excited. The excess power seen in star No. 13 seems to be four times higher than predicted by L/M-scaling. Even if non-radial modes are excited we see twice the amount of power than predicted. We note that the noise might not be well represented by our fit (Fig. 6.4, right panels), and excess power relative to this fit could be due to more complicated drift noise in the data than anticipated.

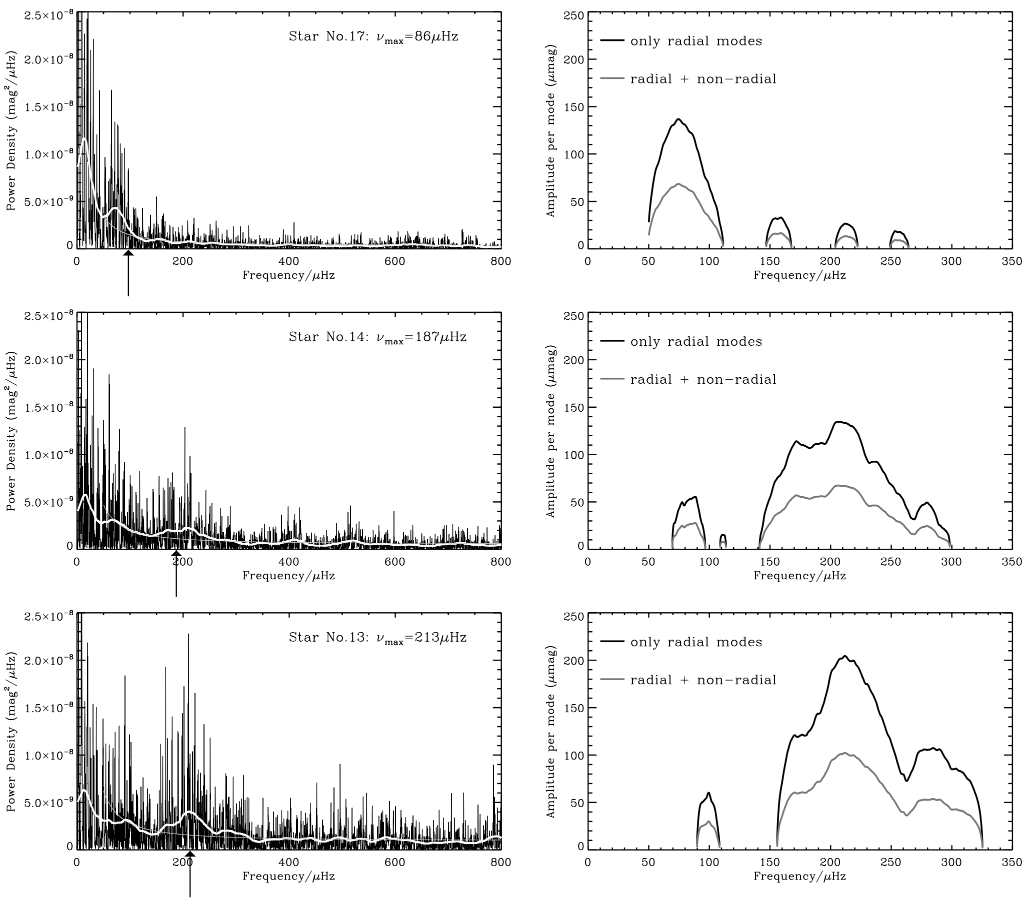

Figure 6.4: **Left panels:** Power density spectra of three selected red giant stars. The thick white solid line is the smoothed spectrum and the thin grey line is a fit to estimate the noise. The arrow indicates the expected value of $\nu_{\max}$. Power density was calculated from Fig. 6.2 by dividing with the integrated power of the spectral window. **Right panels:** Estimated amplitudes for each of the three stars were derived by subtracting the noise from the smoothed power density spectrum, multiplying with $\Delta\nu_0/n$ ($n = 1$ for radial modes only, $n = 4$ for radial plus non-radial modes) and taking the square root.

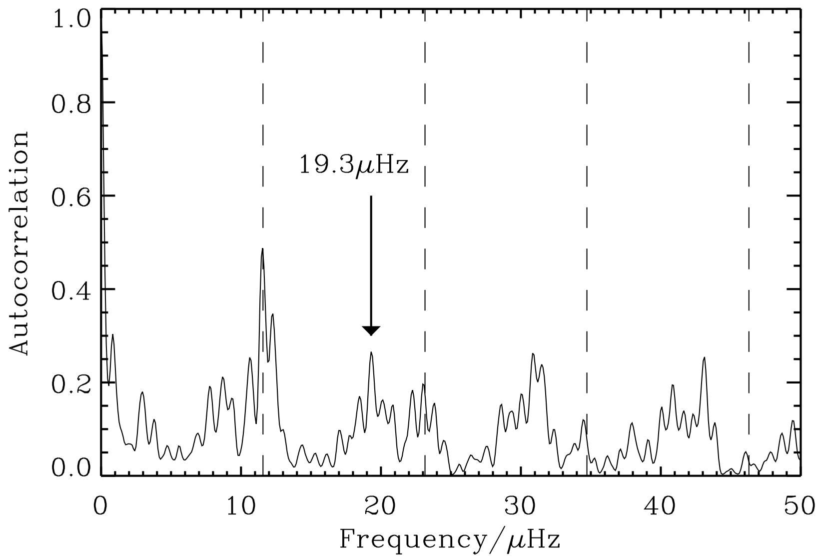

Figure 6.5: Autocorrelation of star No. 13 (see text). Dashed lines indicates integer multiples of one cycle per day (11.574 μHz).

The measured amplitudes of stars No. 17, 14 and 13 using this approach are in agreement with what we find if we try to match the observed Fourier spectra with simulations.

In summary, we see good evidence for oscillation power in three out of six stars, which are expected to oscillate with frequencies larger than 50 μHz. Stars expected to have longer periods were not investigated due to difficulties in determining the noise levels in their power spectra.

6.5.3 Autocorrelation of excess power

To search for a regular series of peaks, we calculated the autocorrelation of stars No. 17, 14 and 13 in the frequency range where we saw excess power. Star No. 17 showed only peaks in the autocorrelation at 1/2 cycle per day and 1 cycle per day, and every combination of these. The same qualitative autocorrelation was seen for all stars with expected oscillation frequencies below $\sim$ 50 μHz, and we conclude this is an effect from our initial cleaning of dominant noise peaks. The autocorrelation of star No. 14 reveals no clear frequency separation, showing only peaks corresponding to the daily aliases. In Fig. 6.5 we show the autocorrelation of the most promising target (No. 13). The autocorrelation was calculated in the frequency range 135–285 μHz setting all values in the Fourier spectrum lower than a threshold of $2\sigma_{300-900\,\mu\mathrm{Hz}}$ (in amplitude) equal to the threshold value. The most significant peak that is not a daily alias is located at 19.3 μHz, which is within 15% of the expected value (Table 6.1).

6.6 Simulations

To interpret the results shown in Sect. 6.5, we made a series of simulations of each target star using the method described by Stello et al. (2004) (see Chapter 3). We chose a regular series of input frequencies with a separation of $\Delta\nu_0$ (Table 6.1). Their relative amplitudes were determined by a Gaussian envelope with a height corresponding to the L/M-scaling values in Table 6.1 (note $L/M^{0.7}$-scaling predicts amplitudes that are roughly 0.3–0.5 times that). The envelope was centered at $\nu_{\rm max}$ (Table 6.1) with a width equal to $0.48\nu_{\rm max}$, which was calibrated to the observations of ξ Hya (Stello et al., 2004, see Chapter 3). The envelope reproduced by this approach is in good agreement with β Hyi and the Sun (Kjeldsen et al., 2005). The number of input frequencies was $7 \times 0.48\nu_{\rm max}/\Delta\nu_0$. Because the non-white noise is difficult to estimate precisely, we chose to include only white noise in the simulations, which we set equal to the mean level in the Fourier spectra at 300–900 μHz of the observed data. For each target star we ran simulations in two parallel runs, one with a mode lifetime of 20 days, in agreement with the theoretical calculations on the red giant ξ Hya (Houdek & Gough, 2002), and the other of 2 days in agreements with the observations of that star (Stello et al., 2006c, see Chapter 4).

We show here the results for the short mode lifetime (Fig. 6.6). The difference between the long and short mode lifetime is discussed below. It is important to stress that the detailed characteristics of the excess power in the Fourier spectra depend very much on the complicated interaction between the spectral window and the oscillation modes (their frequencies, amplitudes and lifetime), as well as the random number seed. For example, using the same random number seed, the clump stars (No. 8, 9, 10, 2 and 18), which had different spectral windows but only slightly different amplitudes and input frequencies, show very different power excesses (Fig. 6.6). For star No. 2 we show in Fig. 6.7 (left panels) five spectra based on different random number seeds. Again, we see a large variation in the result. The right panels show the corresponding spectra based on the long mode lifetime (=20 days). From this, we see that a long mode lifetime in general provides higher peaks, but the differences are comparable to the difference that arise from using a different seed.

Comparing observations and simulations (Figs. 6.2 and 6.6) indicates that a significant part of the excess power seen in the observations might be of stellar origin. The excess power in the observations can be associated with either humps of power (see No. 13 and 17 in Fig. 6.2) or a broad "shoulder" on top of the drift noise (see No. 8). It is clear from the simulations that observing excess power in one star does not imply that we necessarily would see a similar hump in a similar star (or even in the same star if observed at another epoch; Fig. 6.7). We note that the simulations shown in Fig. 6.6 only included radial modes. If the stars have non-radial modes these simulations underestimates the stellar excess power. This could be significant at least for the less evolved stars (No. 13 and 14). Very recently, Hekker et al. (2006, in prep.) reports that non-radial modes are present in two red giant stars (ε Oph and η Ser) that oscillates at approximately 60 μHz and

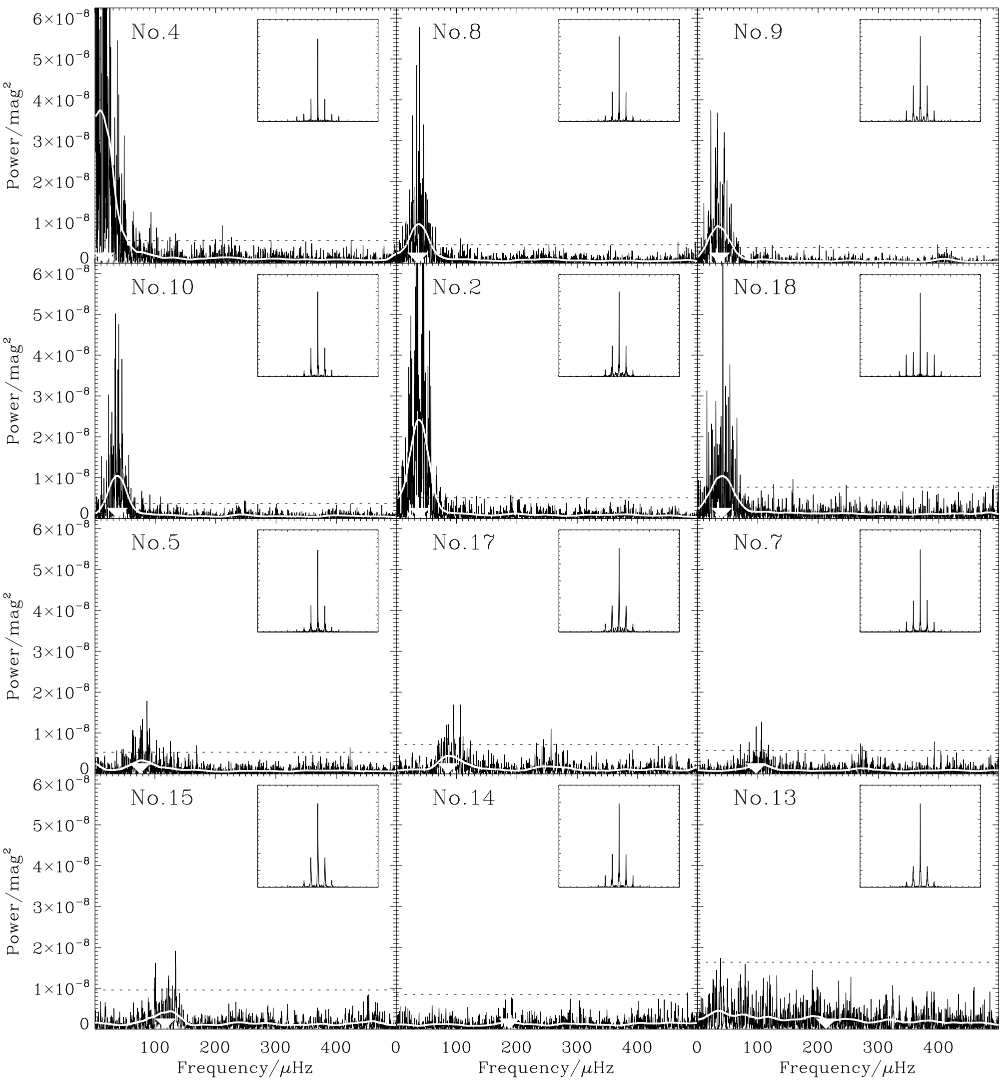

Figure 6.6: Fourier spectra of simulated red giant stars (identifier shown in each panel), with a mode lifetime of 2 days and amplitudes according to L/M-scaling (Eq. 6.1). The solid white line is the smoothed spectrum, and the white arrow head indicates where we expect the stellar excess power (Table 6.1). The inset shows the spectral window on the same frequency scale as the main panel. The dotted line is $(3\sigma_{300-900\,\mu\mathrm{Hz}})^2$.

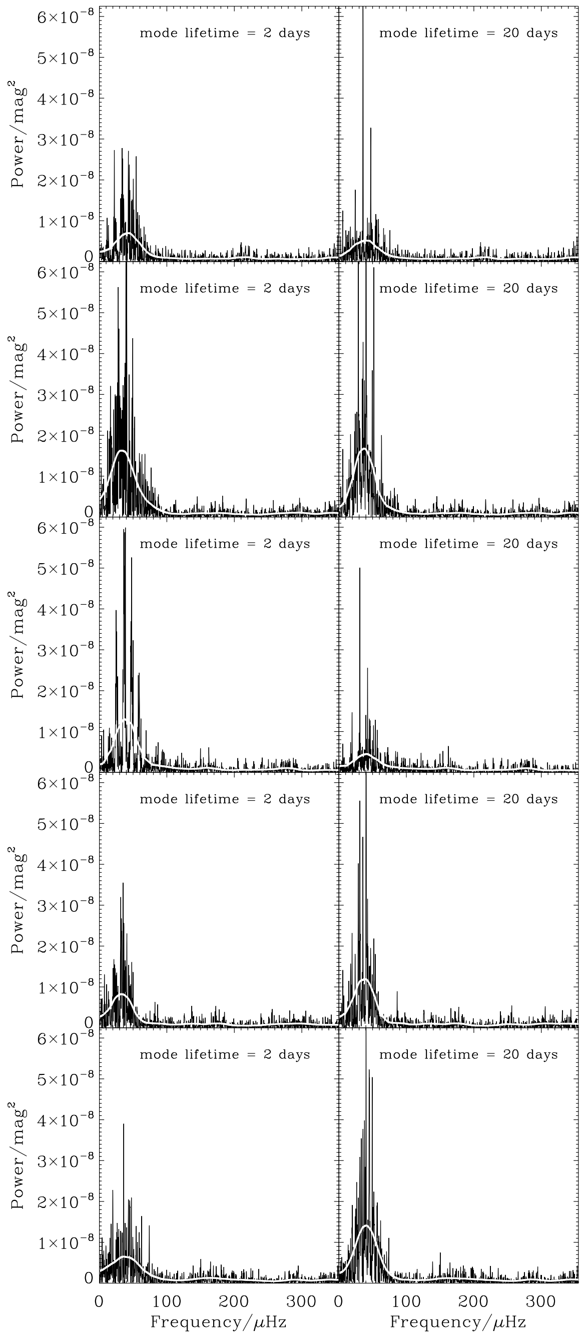

Figure 6.7: Fourier spectra of simulated data (star No. 2) for five different random number seeds. The solid white line is the smoothed spectrum.

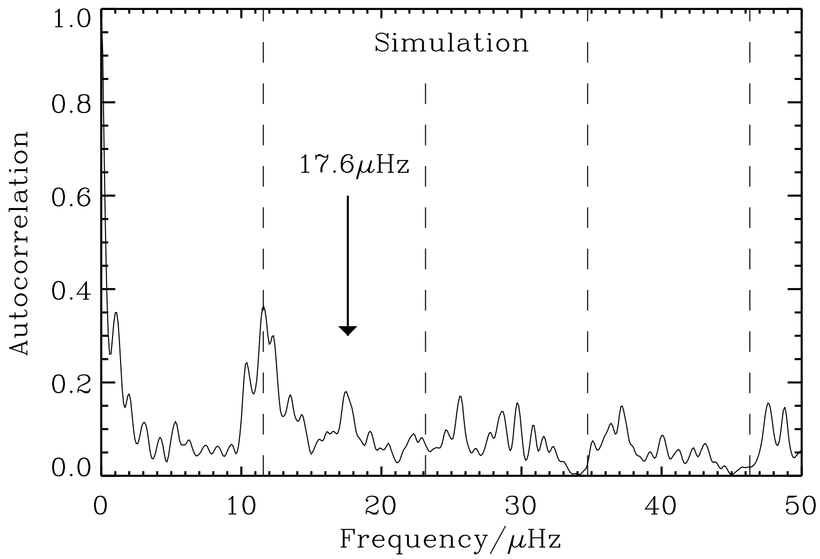

Figure 6.8: Autocorrelation of a simulation of star No. 13 (see text). Dashed lines indicates integer multiples of one cycle per day (11.574 μHz).

130 μHz, respectively, and hence are comparable to stars in our sample (see Fig. 1.9 on page 15). Here we also note that the scaling relation that was used to estimate the amplitudes is quite uncertain for red giant stars. Hence, we cannot exclude a stellar origin of the excess power we see in for example star No. 13, based on these simulations.

Finally, we calculated the autocorrelation of simulated data of star No. 13 that reproduced the observed excess power. This was done by setting the input amplitude of the simulations to 200 μmag and including only radial modes. This time we set the white noise equal to the value estimated at 200 μHz from our noise fit in Fig. 6.4. The autocorrelation was based on simulations with a short mode lifetime (= 2 days) because they produced Fourier spectra more like the observed. In total nine independent simulations were made. In roughly half the cases we saw a peak in the autocorrelation of the same significance as in the observations (Fig. 6.5). In Fig. 6.8 we show one of the examples which show a peak. However, these peaks were not at exactly the same frequency but appeared in an interval from approximately 16 μHz to 19 μHz. Some of these (as in Fig. 6.8) were close to halfway between 1 and 2 cycles per day (17.4 μHz), and might therefore be caused by aliasing. In the other cases the only clear peaks were those clearly originating from the daily aliases at 1, 2 and 3 cycles per day.

To investigate whether the peak seen at 19.3 μHz in the autocorrelation of the observations was caused by interaction between the spectral window and random peaks we repeated the simulations using randomly spaced frequencies. For each of the three sets of random frequencies we made nine independent simulations, and inspected the autocorrelation. The differences seen between each of the independent simulations within each set of frequencies were small compared to the difference between different sets. In most case we did not see a clear peak in the range 16–19 μHz, but a few times a clear peak halfway between 1 and 2 cycles per day (17.4 μHz) was seen. In some cases peaks as significant as the observed 19.3 μHz peak were seen at other frequencies. Hence, we conclude that the peak at 19.3 μHz in the observations could be caused by randomly distributed peaks.

6.7 Conclusions

We have analysed photometric time series of 20 red giant stars in the open cluster M67. The data, recently published in Paper I (see Chapter 5), were from a large multi-site campaign. In many stars we see apparently high levels of non-white noise, but its detailed temporal variation is unknown. In the Fourier spectrum this noise seems to be significant at frequencies below 100 μHz. This is unfortunate because the target stars in which we expected most clear detections are expected to be oscillating in the affected frequency range. We are therefore not able to disentangle the noise and stellar signal in the analysis. Hence, the data did not allow the clear detections that we had anticipated.

We do see evidence of excess power in the Fourier spectra, shifting to lower frequencies for more luminous stars, consistent with expectations. The stellar origin of this excess power is supported by simulations using L/M-scaling to predict mode amplitudes. We note that, the method used to extract the photometric time series could introduce more drift noise (hence more power at low frequencies) for the more luminous and cooler stars, which will simulate a shift of excess power.

In three stars that show a power excess located at the expected frequency, we further estimated the mode amplitude assuming the power originates from solar-like oscillations. These estimated amplitudes are more or less in agreement with what is predicted by scaling from the Sun (L/M-scaling).

These results support that we have seen evidence for solar-like oscillations in some of red giant stars in M67. Due to the difficulties in estimating the noise level at low frequencies our results are tentative, and we do not find basis for extracting individual frequencies. For the same reason we do not give upper limits of the oscillations in stars where no obvious power excess are seen. Theoretical modeling of the pulsations in these stars would greatly improve our capability to interpret our results.

If the observed power excesses are due to stellar oscillations this result shows great prospects for asteroseismology on clusters. However, with the unfortunate cancellation of the Eddington mission by ESA, we might have to wait many years for a dedicated space project specifically aiming at asteroseismology on stellar clusters. Alternatively, one could setup a ground-based network with high-resolution and high-sensitivity spectrographs that is able to detect oscillations in faint cluster stars, or a photometric multi-site campaign of larger telescopes (at least 2 meter) with stable instrumentation located at good sites aimed at red giants in clusters like M67. As clearly demonstrated by our results, the final level of the non-white noise (including drift) in the data will be absolutely crucial in any approach to detect solar-like oscillations in red giant stars. This largely favours space missions as atmospheric effects in ground-based data varies on time scales similar to the stellar oscillations. Although the Kepler and COROT missions will not target clusters, it is expected they will observe many red giants. Recent results from the MOST satellite on the red giant ε Oph (Barban et al. 2006 in prep.) clearly demonstrates that space missions have the potential to do very interesting science on red giant field stars.

Acknowledgments

This work was partly supported by the IAP P5/36 Interuniversity Attraction Poles Programme of the Belgian Federal Office of Scientific, Technical and Cultural Affairs. This paper uses observations made from the South African Astronomical Observatory (SAAO), Siding Spring Observatory (SSO) and the Danish 1.5m telescope at ESO, La Silla, Chile. This research was supported by the Danish Natural Science Research Council through its centre for Ground-Based Observational Astronomy, IJAF, and by the Australian Research Council.

Chapter 7

Thesis conclusions and future work

In this chapter I will give the final conclusions on the combined work presented in this thesis, and in that context provide prospects for what can, should and will be done in the future.

7.1 Conclusions

A large number of red giants were investigated to detect and characterise their oscillations. These investigations were based on data, comprising both photometric and spectroscopic time series, from three independent observing projects aimed at different target stars. One of the photometric data sets provided evidence for excess power consistent with expectation from solar-like oscillations (see Chapter 6). Clear evidence of solar-like oscillations were seen in the spectroscopy, which furthermore revealed new and interesting results on the oscillation characteristics (see Chapters 3 and 4). The main achievements and conclusions of this thesis are:

- We have generated simulations of stochastically excited and intrinsically damped oscillations (see Chapter 3). These were shown to be very useful to interpret observations of solar-like oscillations, and to develop new techniques of time-series analysis. The amplitude inferred using spectroscopic time-series observations and simulations of the red giant ξ Hya ($\sim 2\,\mathrm{m/s}$) agreed with the theoretical value by Houdek & Gough (2002). However, the simulations indicated that the mode lifetime was shorter than predicted by theory (see next point).

- We developed a new technique to measure the mode lifetime of solar-like oscillations. The results point towards a short mode lifetime (roughly 2 days) for the red giant ξ Hya, which contradicts the theoretical value (roughly 20 days) by Houdek & Gough (2002) (see Chapter 4, Fig. 4.8 page 61). This discrepancy could be due to the lack of a proper theory for convection in a pulsating environment, which might be important to better understand the driving and damping of solar-like oscillations in evolved stars where the convection is expected to be quite vigorous.

- Our simulations of solar-like oscillations in red giant stars showed that large variations are expected in the Fourier spectrum of a given star observed at different epochs (see Chapters 3 and 6, Figs. 3.6 and 6.7, pages 39 and 113). This is an important observation, which should be taken into account when evaluating observations of solar-like oscillations such as mode amplitude, frequency and lifetime.

- Simulations of the red giant ξ Hya strongly indicate that no frequencies can be detected unambiguously from the velocity measurements published by Frandsen et al. (2002) (see Chapter 4). This is due to both the non-continuous coverage of the oscillations and the apparently short mode lifetime (see Fig. 4.10 page 65).

- Based on measurements of the mode lifetime and oscillation periods in main-sequence stars and the red giant ξ Hya, there seems to be a steep decline in the quality factor (the period mode-lifetime ratio) towards evolved stars (see Chapter 4, Fig. 4.1 page 53). This implies that the number of coherent oscillation periods that we can observe will be low for evolved stars, which ultimately limits the precision by which we can determine their frequencies. However, this result needs confirmation from additional observations of either the same star with more continuous data coverage or, preferably, of many red giant stars.

- We obtained photometric time series of the open cluster M67 during a multi-site campaign lasting 43 days (see Chapter 5). The nine telescopes (0.6–2.1 metre) collected in total 560 hours of time series of the cluster. On the best nights the noise was limited by irreducible terms (scintillation and photon noise), and reached down to 0.5 mmag per minute of integration.

- Our photometric observations of 20 red giant stars in the open cluster M67 showed excess power in the Fourier spectra consistent with solar-like oscillations (see Chapter 6). The location of the excess power of three different groups of stars (grouped according to their luminosity) matched with expectations (see Fig. 6.3 page 107). In three stars, the excess power was more or less in agreement with the expected amplitudes based on L/M-scaling (see Fig. 6.4 page 109). Simulations further supported that a significant part of the excess seen at low frequencies could be of stellar origin for most target stars (Fig. 6.6 page 112). It was not possible to obtain unambiguous detection of a characteristic frequency separation. The signal-to-noise and lack of a clear frequency pattern did not support further extraction of individual peaks. The limitations of this data set was mainly due to the apparent presence of significant non-white noise, which however, could not be quantified or separated clearly from the stellar signal.

- I was not able to find evidence of solar-like oscillations in any of the red stars (assumed to be predominantly giants) based on the photometric data set provided by the STARE project (see Chapter 2). The white noise alone was too high to allow detection of oscillations with amplitudes below a few millimagnitudes, which excludes red giants with periods shorter than $\sim$ 5 days (see Fig. 2.6 page 25). More luminous red giants with longer periods are not likely to show a clear solar-like power excess (broad envelope with many "equally spaced" modes), and were not investigated. This is because the acoustic cut-off frequency, which is proportional to the inverse of the luminosity (see Eq. 6.2 page 101), gets very small for these stars, allowing only a narrow frequency range for possible oscillations. Although the frequency separation between modes also decreases, it does so only as the luminosity to the power of $-3/4$

(see Eq. 6.3 page 102). As a result, the number of modes that can be excited will decrease and, due to a finite mode lifetime, these modes will eventually overlap. In addition to the white noise, the STARE data was dominated by non-white noise at low frequencies which was roughly ten times larger than the expected mode amplitudes, making it unlikely that this data set could be used for asteroseismic investigations of red giant stars that display signatures of solar-like oscillations.

7.2 Future work

So far, the lack of data with continuous coverage has clearly limited our ability to study the red giant stars in detail. Continuous data coverage of the solar oscillations from the SOHO satellite and the ground-based networks BiSON and GONG has improved the scientific output, and hence our knowledge about the Sun, tremendously. Similarly, observations from dedicated ground-based networks, Antarctic telescopes and space missions such as MOST, COROT and Kepler are the only way we can fully explore and possibly exploit the power of asteroseismic investigations on red giant stars.

Data with almost continuous coverage has already been obtained from the ground for main-sequence stars (e.g. Bedding et al., 2004; Kjeldsen et al., 2005), and red giants (Stello et al., 2006b, see Chapter 5). Very recently, observations from space targeting the red giant star ε Oph provided almost 100% coverage (Barban et al., 2006, in prep.). Much more data of such, and even higher, quality will be available in the near future. MOST is still in operation and has proven to be valuable for observing solar-like oscillations in red giant stars and COROT (although not specifically targeting red giants) is likely to be launched even before the reviewing process of this thesis is over.

Only slightly further down the track, in 2008, the NASA Kepler satellite is expected to be launched. Although its main aim is to detect planets like Earth around solar-like stars, it will observe many thousands of red giant stars, as well as hundreds of thousands of main-sequence stars, with unprecedented precision. Photometric observations will be almost continuous for at least five years. These data will be tremendously exciting, and will enable us to derive empirical relations of the oscillation properties such as amplitude, frequency and mode lifetime. This will almost certainly provide a breakthrough in this research field.

Drift in time-series data causes extra non-white noise at low frequencies, which can jeopardise the results of the time-series analysis even when data are continuous. Data from two of the three observing projects presented in this thesis show dominating or, at least, significant non-white noise at low frequencies. In both cases this has limited and even prevented our ability to detect oscillations. These results clearly demonstrate that the overall stability, including drift, has to be addressed in future ground-based observing campaigns and space missions, and should be taken very seriously when attempting to detect low amplitude solar-like oscillations in red giant stars.

As more high-quality data accumulate, our focus will (hopefully) shift from observational limitations of the scientific output towards more intrinsic limitations of applying asteroseismic techniques to these stars. In other words, we will more directly be able to address the question: What can we actually do with asteroseismology on these stars? To answer this question, we need to investigate the characteristics of the oscillations for this particular group of stars, such as their amplitudes and frequency patterns. One important and interesting aspect, which is likely to play a key role, is the oscillation mode lifetime. Not only does it determine the precision by which we can measure the frequencies, it also holds information about the physics behind the driving and damping mechanisms of the modes.

One of the results from this thesis was that the red giant star ξ Hya seems to have a short mode lifetime. Whether this is a general trend for evolved stars, and hence pointing towards a steep decline in the oscillation quality factor (see Chapter 4, Fig. 4.1) as stars evolve, cannot be concluded at this stage. Interestingly, new observations of the subgiant ν Ind (Bedding et al., 2006) do not support such a steep decline in the quality factor, as indicated by Stello et al. (2006c) (see Chapter 4) (Carrier et al. in prep.), while the new observations of the subgiant β Hyi (Bedding et al. in prep.) does indicate a short mode lifetime. Also, very recently Barban et al., (2006, in prep.) showed evidence of a short mode lifetime in the star ε Oph, which is located in the same part of the HR diagram as ξ Hya (see Fig. 1.9 page 15). Their result confirms the steep decline in the quality factor as suggested by Stello et al. (2006c) (see Chapter 4). These new, and still unpublished, measurements of mode lifetimes in β Hyi, ν Ind and ε Oph are included in Fig. 7.1, which is an updated version of Fig. 4.1. A further test of how the quality factor might scale according to the global stellar parameters, will be possible with the data that we can expect to see in the near future.

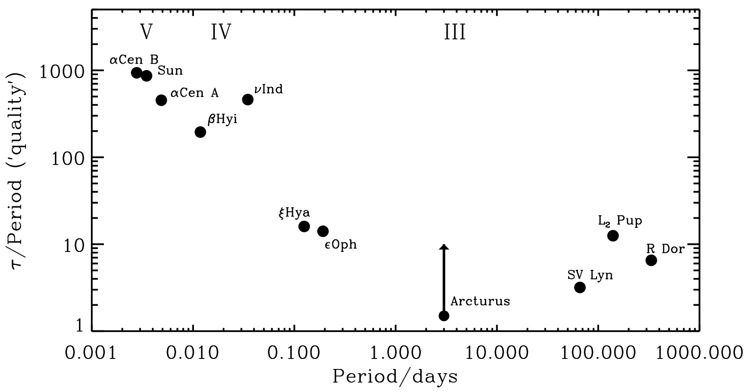

Figure 7.1: The oscillation 'quality' factor vs. period for selected stars. This figure is an updated version of Fig. 4.1 on page 53. The arrow indicates a lower limit. Luminosity classes are indicated at the top. The measured values are from: α Cen B, Kjeldsen et al. (2005); Sun, Chaplin et al. (1997); α Cen A, Kjeldsen et al. (2005); β Hyi, Bedding et al. in prep.; ν Ind, Carrier et al. in prep.; ξ Hya, Stello et al. (2006c) (see Chapter 4); ε Oph, Barban et al., (2006, in prep.); Arcturus, Retter et al. (2003); L_2 Pup, Bedding et al. (2005a); SV Lyn and R Dor, Dind (2004).

List of publications

Papers near completion for peer-reviewed publication

(PhD) 1. Multi-site campaign on the open cluster M67. III. Delta Scuti pulsations in the blue stragglers.
Bruntt, H., **Stello, D.**, Suarez, J. C., Arentoft, T., Bedding, T. R., Sterken, C., Bouzid, M. Y., H., Csubry, Z., Dind, Z. E., Frandsen, S., Gilliland, R. L., Jacob, A. P., Jensen, H. R., Kang, Y. B., Kim, S.-L., Kiss, L. L., Kjeldsen, H., Koo, J.-R., Lee, J.-A., Lee, C.-U., Nuspl, J. and Szabo, R., 2006, Mon. Not. R. Astron. Soc., near submission.

(PhD) 2. Multi-site campaign on the open cluster M67. II. Solar-like oscillations in red giant stars.
Stello, D., Bruntt, H., Kjeldsen, H., Bedding, T. R., Arentoft, T., Gilliland, R. L., Nuspl, J., Kim, S.-L., Kang, Y. B., Koo, J.-R., Lee, J.-A., Sterken, C., Lee, C.-U., Jensen, H. R., Jacob, A. P., Szabo, R., Frandsen, S., Csubry, Z., Dind, Z. E., Bouzid, M. Y. and Kiss, L. L., 2006, Mon. Not. R. Astron. Soc., submitted. (**paper is reproduced in Chapter 6**)

Reviewed publications

(PhD) 3. Multi-site campaign on the open cluster M67. I. Observations and photometric reductions.
Stello, D., Arentoft, T., Bedding, T. R., Bouzid, M. Y., Bruntt, H., Csubry, Z., Dind, Z. E., Frandsen, S., Gilliland, R. L., Jacob, A. P., Jensen, H. R., Kang, Y. B., Kim, S.-L., Kiss, L. L., Kjeldsen, H., Koo, J.-R., Lee, J.-A., Lee C.-U., Nuspl, J., Sterken, C. and Szabo, R., 2006, Mon. Not. R. Astron. Soc., accepted, astro-ph/0609340. (**paper is reproduced in Chapter 5**)

(PhD) 4. Bayesian Inference from Solar-Like Oscillation Data.
Brewer,B. J., Kjeldsen,H., Bedding,T. R. and **Stello,D.** 2006, Astrophys. J., accepted, astro-ph/0608571.

(PhD) 5. Oscillation mode lifetimes in xi Hydrae: Will strong mode damping limit asteroseismology of red giant stars?
Stello,D., Kjeldsen,H., Bedding,T. R. and Buzasi,D. 2006, Astron. & Astrophys. 448, 709. (**paper is reproduced in Chapter 4**)

(PhD) 6. Simulating stochastically excited oscillations: The mode lifetime of xi Hya.
Stello,D., Kjeldsen,H., Bedding,T. R., DeRidder,J., Aerts,C., Carrier,F. and Frandsen,S., 2004, Solar Physics, 220, 207. (**paper is reproduced in Chapter 3**)

(MSc) 7. Giant Vibrations in Dip.
Teixeira, T. C., Christensen-Dalsgaard, J., Carrier, F., Aerts, C., Frandsen, S., **Stello, D.**, Maas, T., Burnet, M., Bruntt, H., de Medeiros, J. R., Bouchy, F., Kjeldsen, H. and Pijpers, F., 2002, Astrophys. & Space Sci., 284, 233.

(MSc) 8. The detection of Solar-like oscillations in the G7 giant star xi Hya.
Frandsen, S., Carrier, F., Aerts, C, **Stello, D.**, Maas, T., Burnet, M., Bruntt, H., Teixeira, T. C., de Medeiros, J., Bouchy, F., Kjeldsen, H., Pijpers, F. and Christensen-Dalsgaard, J., 2002, Astron. & Astrophys. 394, 5.

(MSc) 9. Time-series Spectroscopy of Pulsating sdB Stars II: Velocity Analysis of PG1605+072.
O'Toole, S. J., Bedding, T. R., Kjeldsen, H., Dall, T. H. and **Stello, D.**, 2002, Mon. Not. R. Astron. Soc., 334, 471.

(U.grad.) 10. The problem of the Pleiades distance: Constraints from Strömgren photometry of nearby field stars.
Stello, D. and Nissen, P. E., 2001, Astron. & Astrophys., 374, 105.

Edited conference papers in proceedings

(PhD) 11. Do red giants have short mode lifetimes?
Stello,D., Kjeldsen,H., Bedding,T. R., Buzasi,D., 2005, Proceedings to appear in "Memorie della Societa' Astronomica Italiana", Vol 76/4 eds. A.R. Walker & G. Bono.

(PhD) 12. Multi-Site Time Series Photometry of the Open Cluster M67.
Stello, D., Arentoft, T., Bedding, T. R., Bouzid, M. Y., Bruntt, H., Csubry, Dall, T. H., Z., Dind, Z. E., Frandsen, S., Gilliland, R. L., Jacob, A. P., Jensen, H. R., Kang, Y. B., Kim, S.-L., Kiss, L. L., Kjeldsen, H., Koo, J.-R., Lee, J.-A., Lee, C.-U., Nuspl, J., Qiu, Y., Sterken, C., Szabo, R. and Xiao, P., 2004, ESA SP-559, 639.

(R.ass.) 13. The Eddington CCD data simulator.
Arentoft, T., Kjeldsen, H., De Ridder, J., **Stello, D.**, 2004, ESA SP-538, 59

(MSc) 14. Time Resolved Spectroscopy of the Pulsating sdB Star PG 1605+072.
O'Toole, S. J., Bedding, T. R., Kjeldsen, H., Dall, T. H., & **Stello, D.**, 2002, ASP Proc., 259, 372.

Bibliography

Allen, C. W. (1973). *Astrophysical quantities*. London: University of London, Athlone Press, —c1973, 3rd ed.

Anderson, E. R., Duvall, T. L., & Jefferies, S. M. (1990). Modeling of solar oscillation power spectra. ApJ, **364**, 699.

Baker, N. & Kippenhahn, R. (1962). The Pulsations of Models of δ Cephei Stars. With 17 Figures in the Text. *Zeitschrift Astrophysics*, **54**, 114.

Baldry, I. K. (1999). *Time-series spectroscopy of pulsating stars*. Ph.D. thesis, School of Physics, University of Sydney.

Barban, C., De Ridder, J., Mazumdar, A., Carrier, F., Eggenberger, P., de Ruyter, S., Vanautgaerden, J., Bouchy, F., & Aerts, C. (2004). Detection of Solar-Like Oscillations in Two Red Giant Stars. In *Proceedings of the SOHO 14 / GONG 2004 Workshop (ESA SP-559). "Helio- and Asteroseismology: Towards a Golden Future". 12-16 July, 2004. New Haven, Connecticut, USA. Editor: D. Danesy., p.113*, page 113.

Bedding, T., Kiss, L., & Kjeldsen, H. (2003). Solar-Like Oscillations in Red Giants. *Solar and Solar-Like Oscillations: Insights and Challenges for the Sun and Stars, 25th meeting of the IAU, Joint Discussion 12, 18 July 2003, Sydney, Australia*, **12**.

Bedding, T. R. (2003). Solar-like Oscillations in Semiregular Variables. Ap&SS, **284**, 61–64.

Bedding, T. R. & Kjeldsen, H. (2003). Solar-like Oscillations. *Publications of the Astronomical Society of Australia*, **20**, 203–212.

Bedding, T. R., Butler, R. P., Kjeldsen, H., Baldry, I. K., O'Toole, S. J., Tinney, C. G., Marcy, G. W., Kienzle, F., & Carrier, F. (2001). Evidence for Solar-like Oscillations in β Hydri. ApJ, **549**, L105–L108.

Bedding, T. R., Kjeldsen, H., Butler, R. P., McCarthy, C., Marcy, G. W., O'Toole, S. J., Tinney, C. G., & Wright, J. T. (2004). Oscillation Frequencies and Mode Lifetimes in α Centauri A. ApJ, **614**, 380–385.

Bedding, T. R., Kiss, L. L., Kjeldsen, H., Brewer, B. J., Dind, Z. E., Kawaler, S. D., & Zijlstra, A. A. (2005a). The light curve of the semiregular variable L2 Puppis - II. Evidence for solar-like excitation of the oscillations. MNRAS, **361**, 1375–1381.

Bedding, T. R., Kjeldsen, H., Bouchy, F., Bruntt, H., Butler, R. P., Buzasi, D. L., Christensen-Dalsgaard, J., Frandsen, S., Lebrun, J.-C., Martić, M., & Schou, J. (2005b). The non-detection of oscillations in Procyon by MOST: Is it really a surprise? A&A, **432**, L43–L48.

Bedding, T. R., Butler, R. P., Carrier, F., Bouchy, F., Brewer, B. J., Eggenberger, P., Grundahl, F., Kjeldsen, H., McCarthy, C., Bjorn Nielsen, T., Retter, A., & Tinney, C. G. (2006). Solar-like oscillations in the metal-poor subgiant ν Indi: constraining the mass and age using asteroseismology. *ArXiv Astrophysics e-prints*.

Belmonte, J. A., Jones, A. R., Palle, P. L., & Roca Cortes, T. (1990). Global acoustic oscillations on α Bootis. ApJ, **358**, 595–609.

Bouchy, F. & Carrier, F. (2002). The acoustic spectrum of alpha Cen A. A&A, **390**, 205–212.

Bouchy, F., Bazot, M., Santos, N. C., Vauclair, S., & Sosnowska, D. (2005). Asteroseismology of the planet-hosting star μ Arae. I. The acoustic spectrum. A&A, **440**, 609–614.

Breger, M. (2000). Amplitude Variability of Delta Scuti Stars: 4 CVn. In L. Szabados and D. Kurtz, editors, *ASP Conf. Ser. 203: IAU Colloq. 176: The Impact of Large-Scale Surveys on Pulsating Star Research*, pages 421–425.

Breger, M. & Pamyatnykh, A. A. (2006). Amplitude variability or close frequencies in pulsating stars - the δ Scuti star FG Vir. MNRAS, **368**, 571–578.

Breger, M., Stich, J., Garrido, R., Martin, B., Jiang, S. Y., Li, Z. P., Hube, D. P., Ostermann, W., Paparó, M., & Scheck, M. (1993). Nonradial Pulsation of the Delta-Scuti Star Bu-Cancri in the Praesepe Cluster. A&A, **271**, 482.

Brown, T. M. & Gilliland, R. L. (1994). Asteroseismology. ARA&A, **32**, 37–82.

Brown, T. M., Gilliland, R. L., Noyes, R. W., & Ramsey, L. W. (1991). Detection of possible p-mode oscillations on Procyon. ApJ, **368**, 599–609.

Bruntt, H., Kjeldsen, H., Buzasi, D. L., & Bedding, T. R. (2005). Evidence for Granulation and Oscillations in Procyon from Photometry with the WIRE Satellite. ApJ, **633**, 440–446.

Butler, R. P., Bedding, T. R., Kjeldsen, H., McCarthy, C., O'Toole, S. J., Tinney, C. G., Marcy, G. W., & Wright, J. T. (2004). Ultra-High-Precision Velocity Measurements of Oscillations in α Centauri A. ApJ, **600**, L75–L78.

Buzasi, D., Catanzarite, J., Laher, R., Conrow, T., Shupe, D., Gautier, T. N., Kreidl, T., & Everett, D. (2000). The Detection of Multimodal Oscillations on α Ursae Majoris. ApJ, **532**, L133–L136.

Carrier, F. & Bourban, G. (2003). Solar-like oscillations in the K1 dwarf star alpha Cen B. A&A, **406**, L23–L26.

Carrier, F. & Eggenberger, P. (2006a). Asteroseismology of solar-type stars with CORALIE and HARPS . I: Observations and modelling of single stars. *Memorie della Societa Astronomica Italiana*, **77**, 326–+.

Carrier, F. & Eggenberger, P. (2006b). Asteroseismology of the visual binary 70 Ophiuchi. A&A, **450**, 695–699.

Carrier, F., Eggenberger, P., & Bouchy, F. (2005a). New seismological results on the G0 IV η Bootis. A&A, **434**, 1085–1095.

Carrier, F., Eggenberger, P., D'Alessandro, A., & Weber, L. (2005b). Solar-like oscillations in the F9 V β Virginis. *New Astronomy*, **10**, 315–323.

Chang, H.-Y. & Gough, D. O. (1998). On the Power Distribution of Solar p Modes. *Sol. Phys.*, **181**, 251–263.

Chaplin, W. J., Elsworth, Y., Isaak, G. R., McLeod, C. P., Miller, B. A., & New, R. (1997). Solar p-mode linewidths from recent BiSON helioseismological data. MNRAS, **288**, 623–626.

Christensen-Dalsgaard, J. (1995). Stellar Structure and Evolution. Lecture notes, Aarhus Universitet, August 1995, Fourth edition.

Christensen-Dalsgaard, J. (2002). Helioseismology. *Reviews of Modern Physics*, **74**, 1073–1129.

Christensen-Dalsgaard, J. (2003). Stellar Oscillations. Lecture notes, Aarhus Universitet, May 2003, Fifth edition.

Christensen-Dalsgaard, J. (2004). Physics of solar-like oscillations. Sol. Phys., **220**, 137–168.

Christensen-Dalsgaard, J. & Frandsen, S. (1983). Stellar 5 min oscillations. Sol. Phys., **82**, 469–486.

Christensen-Dalsgaard, J., Kjeldsen, H., & Mattei, J. A. (2001). Solar-like Oscillations of Semiregular Variables. ApJ, **562**, L141–L144.

Cochran, W. D. (1988). Confirmation of radial velocity variability in Arcturus. ApJ, **334**, 349–356.

Cox, J. P. (1980). *Theory of stellar pulsation.* Research supported by the National Science Foundation Princeton, NJ, Princeton University Press, 1980. 393 p.

De Ridder, J. (2002). Time-series simulator. Technical report, Rømer Science Data Center, Aarhus Universitet.

De Ridder, J., Kjeldsen, H., Arentoft, T., & Claret, A. (2004). The Eddington light curve simulator. In F. Favata, S. Aigrain, and A. Wilson, editors, *ESA SP-538: Stellar Structure and Habitable Planet Finding*, pages 67–70.

De Ridder, J., Barban, C., Carrier, F., Mazumdar, A., Eggenberger, P., Aerts, C., Deruyter, S., & Vanautgaerden, J. (2006). Discovery of solar-like oscillations in the red giant ε Ophiuchi. A&A, **448**, 689–695.

Delache, P. & Scherrer, P. H. (1983). Detection of solar gravity mode oscillations. Nature, **306**, 651–653.

Dind, Z. E. (2004). Mode lifetimes in semi-regular variables. Honours thesis, School of Physics, University of Sydney.

Dziembowski, W. A., Gough, D. O., Houdek, G., & Sienkiewicz, R. (2001). Oscillations of α UMa and other red giants. MNRAS, **328**, 601–610.

Edmonds, P. D. & Gilliland, R. L. (1996). K Giants in 47 Tucanae: Detection of a New Class of Variable Stars. ApJ, **464**, L157.

Elsworth, Y. P. & Thompson, M. J. (2004). Asteroseismology: Asteroseismology of Sun-like stars. *Astronomy and Geophysics*, **45**, 5.14.

Frandsen, S., Jones, A., Kjeldsen, H., Viskum, M., Hjorth, J., Andersen, N. H., & Thomsen, B. (1995). CCD photometry of the δ-Scuti star κ^2 Bootis. A&A, **301**, 123.

Frandsen, S., Carrier, F., Aerts, C., Stello, D., Maas, T., Burnet, M., Bruntt, H., Teixeira, T. C., de Medeiros, J. R., Bouchy, F., Kjeldsen, H., Pijpers, F., & Christensen-Dalsgaard, J. (2002). Detection of Solar-like oscillations in the G7 giant star ξ Hya. A&A, **394**, L5–L8.

Gilliland, R. L. & Brown, T. M. (1988). Time-resolved CCD photometry of an ensemble of stars. PASP, **100**, 754–765.

Gilliland, R. L. & Brown, T. M. (1992a). Limits to CCD ensemble photometry precision, and prospects for asteroseismology. PASP, **104**, 582–591.

Gilliland, R. L. & Brown, T. M. (1992b). The oscillating blue stragglers in the open cluster M67. AJ, **103**, 1945–1954.

Gilliland, R. L., Brown, T. M., Duncan, D. K., Suntzeff, N. B., Lockwood, G. W., Thompson, D. T., Schild, R. E., Jeffrey, W. A., & Penprase, B. E. (1991). Time-resolved CCD photometry of an ensemble of stars in the open cluster M67. AJ, **101**, 541–561.

Gilliland, R. L., Brown, T. M., Kjeldsen, H., McCarthy, J. K., Peri, M. L., Belmonte, J. A., Vidal, I., Cram, L. E., Palmer, J., Frandsen, S., Parthasarathy, M., Petro, L., Schneider, H., Stetson, P. B., & Weiss, W. W. (1993). A search for solar-like oscillations in the stars of M67 with CCD ensemble photometry on a network of 4 M telescopes. AJ, **106**, 2441–2476.

Girard, T. M., Grundy, W. M., Lopez, C. E., & van Altena, W. F. (1989). Relative proper motions and the stellar velocity dispersion of the open cluster M67. AJ, **98**, 227–243.

Goldreich, P. & Keeley, D. A. (1977). Solar seismology. II - The stochastic excitation of the solar p-modes by turbulent convection. ApJ, **212**, 243–251.

Gough, D. O. & Novotny, E. (1993). Asteroseismic Calibration of Stellar Clusters. In T. M. Brown, editor, *ASP Conf. Ser. 42: GONG 1992. Seismic Investigation of the Sun and Stars*, page 355.

Gray, D. F. (1992). *The observation and analysis of stellar photospheres*. Cambridge Astrophysics Series, Cambridge: Cambridge University Press, 1992, 2nd ed., ISBN 0521403200.

Gray, D. F. & Nagel, T. (1989). The granulation boundary in the H-R diagram. ApJ, **341**, 421–426.

Guenther, D. B., Demarque, P., Buzasi, D., Catanzarite, J., Laher, R., Conrow, T., & Kreidl, T. (2000). Evolutionary Model and Oscillation Frequencies for α Ursae Majoris: A Comparison with Observations. ApJ, **530**, L45–L48.

Guenther, D. B., Kallinger, T., Reegen, P., Weiss, W. W., Matthews, J. M., Kuschnig, R., Marchenko, S., Moffat, A. F. J., Rucinski, S. M., Sasselov, D., & Walker, G. A. H. (2005). Stellar Model Analysis of the Oscillation Spectrum of η Bootis Obtained from MOST. ApJ, **635**, 547–559.

Handler, G. (2003). Merging Data from Large and Small Telescopes – Good or Bad? And: How Useful is the Application of Statistical Weights to Time-Series Photometric Measurements? *Baltic Astronomy*, **12**, 253–270.

Hatzes, A. P. & Cochran, W. D. (1993). Long-period radial velocity variations in three K giants. ApJ, **413**, 339–348.

Hatzes, A. P. & Cochran, W. D. (1994). Short-period radial velocity variations of α Bootis: Evidence for radial pulsations. ApJ, **422**, 366–373.

Hatzes, A. P. & Cochran, W. D. (1998). Stellar Oscillations in K Giant Stars. In *ASP Conf. Ser. 154: Cool Stars, Stellar Systems, and the Sun*, volume 10, page 311.

Hekker, S., Reffert, S., Quirrenbach, A., Mitchell, D. S., Fischer, D. A., Marcy, G. W., & Butler, R. P. (2006a). Precise radial velocities of giant stars. I. Stable stars. A&A, **454**, 943–949.

Hekker, S., Aerts, C., De Ridder, J., & Carrier, F. (2006b). Pulsations detected in the line profile variations of red giants: Modelling of line moments, line bisector and line shape. *ArXiv Astrophysics e-prints*.

Henry, G. W., Fekel, F. C., Henry, S. M., & Hall, D. S. (2000). Photometric Variability in a Sample of 187 G and K Giants. ApJS, **130**, 201–225.

Honeycutt, R. K. (1992). CCD ensemble photometry on an inhomogeneous set of exposures. PASP, **104**, 435–440.

Horner, S. (1996). A Search for Pulsations in Four Late-Type Giants. ApJ, **460**, 449.

Houdek, G. & Gough, D. O. (2002). Modelling pulsation amplitudes of ξ Hydrae. MNRAS, **336**, L65–L69.

Houdek, G., Balmforth, N. J., Christensen-Dalsgaard, J., & Gough, D. O. (1999). Amplitudes of stochastically excited oscillations in main-sequence stars. A&A, **351**, 582–596.

Jiménez, A., Roca Cortés, T., Severino, G., & Marmolino, C. (1999). Phase Differences and Gains between Intensity and Velocity in Low-Degree Acoustic Modes Measured by SOHO. ApJ, **525**, 1042–1055.

Kippenhahn, R. & Weigert, A. (1990). *Stellar Structure and Evolution*. Stellar Structure and Evolution, XVI, 468 pp. 192 figs.. Springer-Verlag Berlin Heidelberg New York. Also Astronomy and Astrophysics Library.

Kiss, L. L. & Bedding, T. R. (2003). Red variables in the OGLE-II data base - I. Pulsations and period-luminosity relations below the tip of the red giant branch of the Large Magellanic Cloud. MNRAS, **343**, L79–L83.

Kjeldsen, H. (2003). Space and Ground Based Data for Asteroseismology. Ap&SS, **284**, 1–12.

Kjeldsen, H. & Bedding, T. R. (1995). Amplitudes of stellar oscillations: the implications for asteroseismology. A&A, **293**, 87–106.

Kjeldsen, H. & Bedding, T. R. (1998). MONS: A proposal for a Danish satellite. In *The First MONS Workshop: Science with a Small Space Telescope, held in Aarhus, Denmark, June 29 - 30, 1998, Eds.: H. Kjeldsen, T.R. Bedding, Aarhus Universitet, p. 1.*, page 1.

Kjeldsen, H. & Bedding, T. R. (2001). Current status of asteroseismology. *Proceedings of the SOHO 10/GONG 2000 Workshop: Helio- and asteroseismology at the dawn of the millennium, 2-6 October 2000, Santa Cruz de Tenerife, Tenerife, Spain. Edited by A. Wilson, Scientific coordination by P. L. Pallé. ESA SP-464, Noordwijk: ESA Publications Division, ISBN 92-9092-697-X, 2001, p. 361 - 366*, **464**, 361.

Kjeldsen, H. & Frandsen, S. (1992). High-precision time-resolved CCD photometry. PASP, **104**, 413–434.

Kjeldsen, H., Bedding, T. R., Viskum, M., & Frandsen, S. (1995). Solarlike oscillations in η Boo. AJ, **109**, 1313–1319.

Kjeldsen, H., Bedding, T. R., Baldry, I. K., Bruntt, H., Butler, R. P., Fischer, D. A., Frandsen, S., Gates, E. L., Grundahl, F., Lang, K., Marcy, G. W., Misch, A., & Vogt, S. S. (2003). Confirmation of Solar-like Oscillations in η Bootis. AJ, **126**, 1483–1488.

Kjeldsen, H., Bedding, T. R., Butler, R. P., Christensen-Dalsgaard, J., Kiss, L. L., McCarthy, C., Marcy, G. W., Tinney, C. G., & Wright, J. T. (2005). Solar-like Oscillations in α Centauri B. ApJ, **635**, 1281–1290.

Knudsen, M. R. (2000). *Measuring oscillations in the roAp star HR1217 using echelle-spectroscopy. An oblique pulsator in a new perspective.* Master's thesis, Institut for Fysik og Astronomi, Aarhus Universitet.

Leifsen, T., Andersen, B. N., & Toutain, T. (2001). Temporal behaviour of radial p-modes. In *ESA SP-464: SOHO 10/GONG 2000 Workshop: Helio- and Asteroseismology at the Dawn of the Millennium*, page 63.

Leighton, R. B., Noyes, R. W., & Simon, G. W. (1962). Velocity Fields in the Solar Atmosphere. I. Preliminary Report. ApJ, **135**, 474.

Lejeune, T., Cuisinier, F., & Buser, R. (1998). A standard stellar library for evolutionary synthesis. II. The M dwarf extension. A&AS, **130**, 65–75.

Libbrecht, K. G. (1988). Solar p-mode phenomenology. ApJ, **334**, 510–516.

Martić, M., Lebrun, J.-C., Appourchaux, T., & Korzennik, S. G. (2004). p-mode frequencies in solar-like stars. I. Procyon A. A&A, **418**, 295–303.

Matthews, J. M., Kusching, R., Guenther, D. B., Walker, G. A. H., Moffat, A. F. J., Rucinski, S. M., Sasselov, D., & Weiss, W. W. (2004). No stellar p-mode oscillations in space-based photometry of Procyon. Nature, **430**, 51–53.

Montgomery, K. A., Marschall, L. A., & Janes, K. A. (1993). CCD photometry of the old open cluster M67. AJ, **106**, 181–219.

Montgomery, M. H. & O'Donoghue, D. (1999). Delta Scuti Star Newsletter 13, 28 (University of Vienna).

Nissen, P. E., Twarog, B. A., & Crawford, D. L. (1987). UvbyH-beta photometry of main-sequence stars in M67. AJ, **93**, 634–646.

Pasquini, L., de Medeiros, J. R., & Girardi, L. (2000). Ca II activity and rotation in F-K evolved stars. A&A, **361**, 1011–1022.

Pietrinferni, A., Cassisi, S., Salaris, M., & Castelli, F. (2004). A Large Stellar Evolution Database for Population Synthesis Studies. I. Scaled Solar Models and Isochrones. ApJ, **612**, 168–190.

Ponman, T. (1981). The analysis of periodicities in irregularly sampled data. MNRAS, **196**, 583–596.

Press, W. H., Teukolsky, S. A., Vetterling, W. T., & Flannery, B. P. (1992). *Numerical recipes in C. The art of scientific computing*. Cambridge: University Press, —c1992, 2nd ed.

Priestley, M. B. (1981). *Spectral analysis and time series*, volume 1 of *Probability and mathematical statistics*. London; New York: Academic Press.

Retter, A., Bedding, T. R., Buzasi, D. L., Kjeldsen, H., & Kiss, L. L. (2003). Oscillations in Arcturus from WIRE photometry. ApJ, **591**, L151–L154. Erratum: 596, L125.

Samadi, R., Goupil, M. J., Baudin, F., Georgobiani, D., Trampedach, R., Stein, R., & Nordlund, A. (2004). Oscillation Power Spectra of the Sun and of CEN a: Observations Versus Models. In *ESA SP-559: SOHO 14 Helio- and Asteroseismology: Towards a Golden Future*, page 615.

Samadi, R., Goupil, M.-J., Alecian, E., Baudin, F., Georgobiani, D., Trampedach, R., Stein, R., & Nordlund, Å. (2005). Excitation of Solar-like Oscillations: From PMS to MS Stellar Models. *JApA*, **26**, 171.

Sanders, W. L. (1977). Membership of the open cluster M 67. A&AS, **27**, 89–116.

Schultheis, M., Glass, I. S., & Cioni, M.-R. (2004). Late-type giant variables in NGC 6522, LMC and SMC. How do they differ? A&A, **427**, 945–958.

Smith, P. H., McMillan, R. S., & Merline, W. J. (1987). Evidence for periodic radial velocity variations in Arcturus. ApJ, **317**, L79–L84.

Stello, D. (2002). *Detecting solar-like oscillations in the giant star ξ Hydrae. New prospects for asteroseismology throughout the HR-diagram*. Master's thesis, Institut for Fysik og Astronomi, Aarhus Universitet. Available HTTP: http://www.phys.au.dk/∼stello/Publications/thesis.pdf.

Stello, D., Kjeldsen, H., Bedding, T. R., De Ridder, J., Aerts, C., Carrier, F., & Frandsen, S. (2004). Simulating stochastically excited oscillations - The mode lifetime of ξ Hya. Sol. Phys., **220**, 207–228.

Stello, D., Bruntt, H., Kjeldsen, H., Bedding, T. R., Arentoft, T., Gilliland, R. L., Nuspl, J., Kim, S.-L., Kang, Y. B., Koo, J.-R., Lee, J.-A., Sterken, C., Lee, C.-U., Jensen, H. R., Jacob, A. P., Szabo, R., Frandsen, S., Csubry, Z., Dind, Z. E., Bouzid, M. Y., & Kiss, L. L. (2006a). Multi-site campaign on stellar variability in the open cluster m67. ii. solar-like oscillations in red giant stars. submitted to MNRAS.

Stello, D., Arentoft, T., Bedding, T. R., Bouzid, M. Y., Bruntt, H., Csubry, Z., Dind, Z. E., Frandsen, S., Gilliland, R. L., Jacob, A. P., Jensen, H. R., Kang, Y. B., Kim, S.-L., Kiss, L. L., Kjeldsen, H., Koo, J.-R., Lee, J.-A., Lee, C.-U., Nuspl, J., Sterken, C., & Szabo, R. (2006b). Multi-site campaign on the open cluster m67. i. observations and photometric reductions. submitted to MNRAS.

Stello, D., Kjeldsen, H., Bedding, T. R., & Buzasi, D. (2006c). Oscillation mode lifetimes in ξ Hydrae: will strong mode damping limit asteroseismology of red giant stars? A&A, **448**, 709–715.

Tassoul, M. (1980). Asymptotic approximations for stellar nonradial pulsations. ApJS, **43**, 469–490.

Teixeira, T. C., Christensen-Dalsgaard, J., Carrier, F., Aerts, C., Frandsen, S., Stello, D., Maas, T., Burnet, M., Bruntt, H., de Medeiros, J. R., Bouchy, F., Kjeldsen, H., & Pijpers, F. (2003). Giant Vibrations in Dip. Ap&SS, **284**, 233–236.

Thévenin, F., Kervella, P., Pichon, B., Morel, P., di Folco, E., & Lebreton, Y. (2005). VLTI/VINCI diameter constraints on the evolutionary status of δ Eri, ξ Hya, η Boo. A&A, **436**, 253–262.

Ulrich, R. K. (1986). Determination of stellar ages from asteroseismology. ApJ, **306**, L37–L40.

VandenBerg, D. A. & Stetson, P. B. (2004). On the Old Open Clusters M67 and NGC 188: Convective Core Overshooting, Color-Temperature Relations, Distances, and Ages. PASP, **116**, 997–1011.

Walker, G. A. H., Yang, S., Campbell, B., & Irwin, A. W. (1989). Yellow giants - A new class of radial velocity variable? ApJ, **343**, L21–L24.

Winget, D. E., Nather, R. E., Clemens, J. C., Provencal, J., Kleinman, S. J., Bradley, P. A., Wood, M. A., Claver, C. F., Frueh, M. L., Grauer, A. D., Hine, B. P., Hansen, C. J., Fontaine, G., Achilleos, N., Wickramasinghe, D. T., Marar, T. M. K., Seetha, S., Ashoka, B. N., O'Donoghue, D., Warner, B., Kurtz, D. W., Buckley, D. A., Brickhill, J., Vauclair, G., Dolez, N., Chevreton, M., Barstow, M. A., Solheim, J. E., Kanaan, A., Kepler, S. O., Henry, G. W., & Kawaler, S. D. (1991). Asteroseismology of the DOV star PG 1159 - 035 with the Whole Earth Telescope. ApJ, **378**, 326–346.

Young, A. T. (1967). Photometric error analysis. VI. Confirmation of Reiger's theory of scintillation. AJ, **72**, 747.

Zhao, J. L., Tian, K. P., Pan, R. S., He, Y. P., & Shi, H. M. (1993). Study of proper motions in the region of the open cluster M67 and membership of stars. A&AS, **100**, 243–261.

Appendix A

The detection of oscillations in α Cen A: is it really a surprise?

In 2004, while I was visiting Aarhus University, a paper in *Nature* was published by Matthews et al. (2004), who reported 'No stellar p-mode oscillations in space-based photometry of Procyon'. The content of this paper sparked a following letter by Bedding et al. (2005b) in A&A with the title 'The non-detection of oscillations in Procyon by MOST: Is it really a surprise?', which was aimed directly at the paper previously published by Matthews et al. (2004).

During late hours at a cafe in downtown Aarhus, which is known for its very tasty Belgian beverage, I and a group of other astronomers got inspired by the ongoing discussions about Procyon. The more beer we tasted the more inspired we got. At the end of the night we had decided to give a presentation at the weekly colloquium in Aarhus and to write a supplementary paper to hand out to the audience with a title similar to that of the Bedding et al. (2005b) paper, but with completely different content. The presentation was by myself and Torben Arentoft who also contributed substantially to the paper, and should therefore be equally blamed `;O)`

Although the paper was not meant to be published in a journal it has been included in its original A&A-style in this Appendix for completeness.

One piece of information the reader needs (apart from reading the two papers mentioned above) is that one of the authors of the Bedding et al. (2005b) paper who is addressed in our paper is generally very positive which can be heard over long distances as a characteristic laugh.

The paper was presented as a poster at the *Stellar Pulsation and Evolution Workshop* in Rome 2004.

WARNING: This paper contains a lot of humour and very little science!!!

Astronomy & Astrophysics manuscript no. laugh February 3, 2005
(DOI: will be inserted by hand later)

The detection of oscillations in α Cen A: is it really a surprise?

D. Stello[1,2,3]⋆, T. Arentoft[1], H. Bruntt[1,3], F. Grundahl[1], J. De Ridder[4], and nearly everybody else except T. R. Bedding, H. Kjeldsen and J. Christensen-Dalsgaard

[1] Department of Physics and Astronomy, Aarhus University, 8000 Aarhus C, Denmark
[2] School of Physics, University of Sydney, NSW 2006, Australia
[3] Department of Physics, US Air Force Academy, Colorado Springs, CO 80840, USA
[4] Instituut voor Sterrenkunde, Katholieke Universiteit Leuven, 3001 Leuven, Belgium

Received 1. February 2005/ Accepted

Abstract. We will prove conclusively that the detection of solar-like oscillations in α Cen A by Butler et al. (2004) and Bedding et al. (2004) are not, as claimed by the authors, of stellar origin. They are of human origin. We have compelling evidence from measurements from a number of seismic stations on ground that there is a 1:1 correlation between the frequencies of the detected oscillations and unusual seismic activity on the earth during the observing period. Using techniques acquired by one of us (HB) during his time in the US Air Force, and which we cannot reveal for security reasons (we would have to kill you all if we did), we have secretly monitored the frequency spectrum of the laughter of one of the observers (Hans Kjeldsen) and we show beyond doubt that the detected "oscillations" can be traced directly to this noise source. We do, however, recognize that the erroneous results were not deliberately presented, but that this is instead a case of misinterpretation due to lack of data. Our ground-based seismic data, which represents the best seismic data ever obtained on earth by an order of magnitude, and which were not available to the authors of the α Cen A papers, disclose the faulty interpretation.

1. Introduction

The search for oscillations in solar-like stars has been intensified in recent years and several claims of detected oscillations have been made for bright stars such as α Cen A (Bedding et al. 2004; Butler et al. 2004), Procyon (Martić et al. 1999), η Boo (Kjeldsen & Bedding 1995) and β Hydri (Bedding et al. 2001). None of these results were, however, really very convincing and the first serious attempt to detect solar-like oscillations was made with the Canadian micro-satellite MOST during observations of Procyon almost uninterrupted for 32 days (Matthews et al. 2004). But, their null-result, despite the fact that their data was the best data ever obtained for seismic studies of stars other than the Sun, by an order of magnitude, cast unsurprising doubt upon the previous claims of detections of solar-like oscillations in stars. In this paper we join Matthews et al. (2004) and reject yet another claim of detection of solar-like oscillations, by demonstrating that α Cen A, despite seemingly convincing variability data, is, in fact, just another flat-liner.

2. Data

Our data comprise four independent datasets. The first is the actual data presented by Butler et al. (2004); Bedding et al. (2004), used for claiming that solar-like oscillations are present in α Cen A. By presenting our arguments to "The Danish Committees on Scientific Dishonesty", we were given permission to access the α Cen A data without the consent of the authors. We did this using undisclosed methods (okay, it was hacking). Due to the security level at Aarhus University it was, however, not very difficult.

Another dataset was measured by one of the authors (HB) using highly specialized equipment developed at the US Air force Academy in Colorado Springs (see Fig. 1). The measurements were made at Aarhus University where the pressure modes (p-modes) of a very strong noise source often are present. The choice of location was due to the fact that these solar-like p-modes are heard with very large amplitudes, especially in building 520 room 222 of Aarhus University, and hence we expected our result to prove the highest S/N observations of these solar-like p-modes here on Earth (see Fig. 2).

The two remaining datasets which show the same solar-like p-modes – perhaps by coincidence, perhaps not – have kindly been supplied by two seismic networks in Denmark (Kort- og Matrikelstyrelsen; P. Foss, see Fig. 3) and in Chile (CINCA95; R. Patzig, Fig. 4).

The first of these comprise measurements from central Jutland at a time where we know Hans Kjeldsen was at his home in Engesvang. The second include measurements from the local earthquake tomography in the Antofagasta (Chile) re-

⋆ stello@phys.au.dk

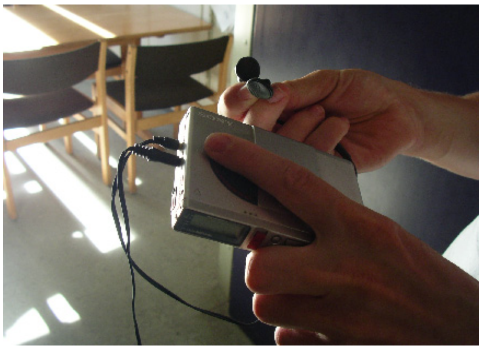

Fig. 1. Our specialized equipment to measure oscillations of pressure modes (p-modes), which is developed by the US Air force Academy in Colorado Springs.

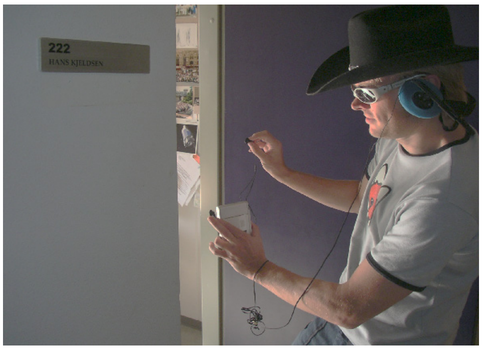

Fig. 2. The p-mode source was measured by HB using the most sophisticated technique ever used for ground based observations.

gion. R. Patzig (Berlin) writes: "In May, 2001, several earthquakes with magnitudes up to Mw = 8.0 (Mb = 6.6) occurred during a period of 5 days, all with epi-centers 120 km south of Antofagasta (Northern Chile), at the mountain of Cerro Paranal. Fortunately the city of Antofagasta was spared from big damage. At the times when the quakes hit, the active seismic measurements of the project CINCA95 were ongoing. It was planned from the beginning that the project should include a temporal seismological network. So the rare chance of several earthquakes originating from the same spot, within a short period of time, was used to register sufficient events for a computation of a 3D velocity model. Moreover the network could be enlarged when the German Task Force for Earthquakes (GeoForschungsZentrum Potsdam, Germany) of the German IDNDR Committee additionally installed seismological stations in the Antofagasta region. This is a truly remarkable and wonderful dataset." To this we just add that the time of the strong earth-quake activity coincides very precisely with the time Hans Kjeldsen was observing α Cen A at VLT, located at – of course – Cerro Paranal.

Fig. 3. Seismologist Peter Foss from Kort- og Matrikelstyrelsen in Denmark shows the instrument at the seismic station near Silkeborg were part of the data have been measured (we cannot tell you the exact location. Well, we could, but then we would have to kill you once again).

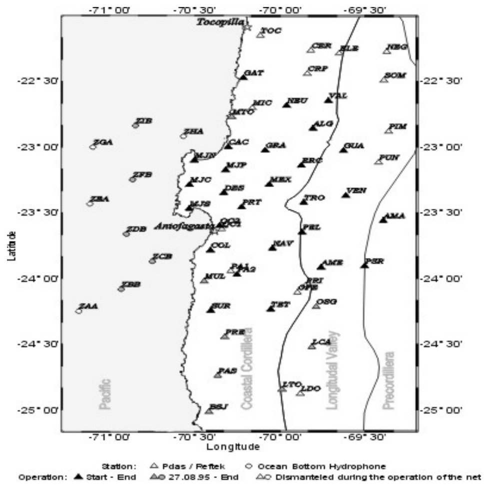

Fig. 4. The seismic network in the Antofagasta region in Chile.

3. Discussion

We show in Fig. 5 the power spectrum of the combined time series obtained at VLT (ESO, Chile) and AAT (Australia). This plot was used by Bedding et al. (2004) to claim detection of solar-like oscillations in α Cen A. In Fig. 6 and Fig. 7 we show in addition the power spectra of the time series of the two individual sites.

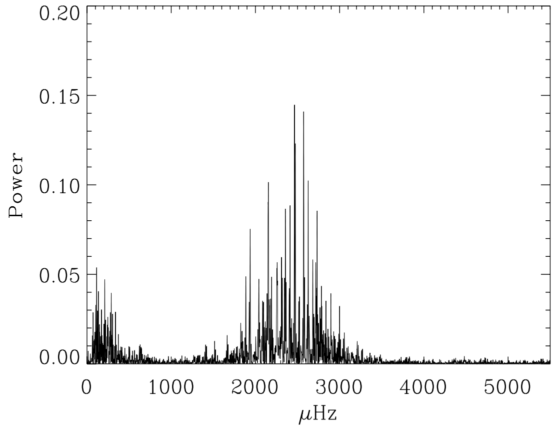

Fig. 5. The VLT+AAT data used for claiming stellar p-modes by Bedding et al. (2004).

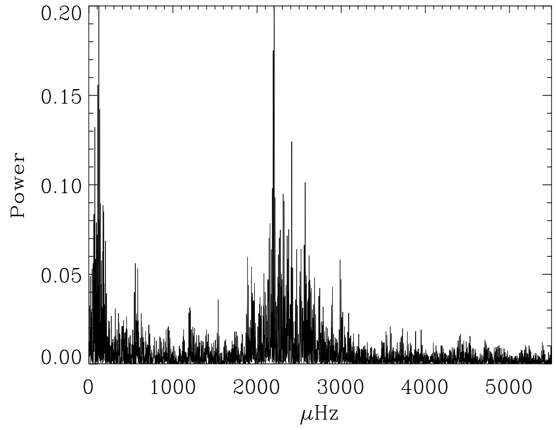

Fig. 7. The AAT data used for claiming stellar p-modes by Bedding et al. (2004).

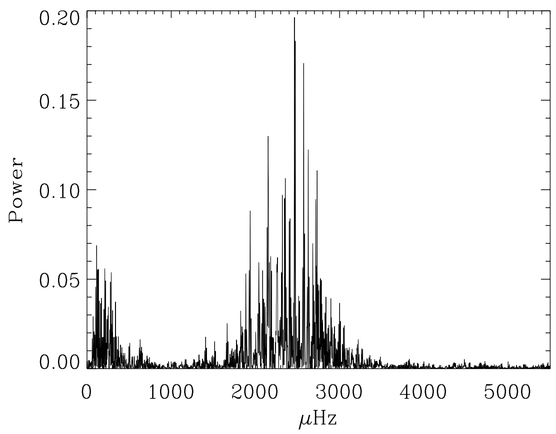

Fig. 6. The VLT data used for claiming stellar p-modes by Bedding et al. (2004).

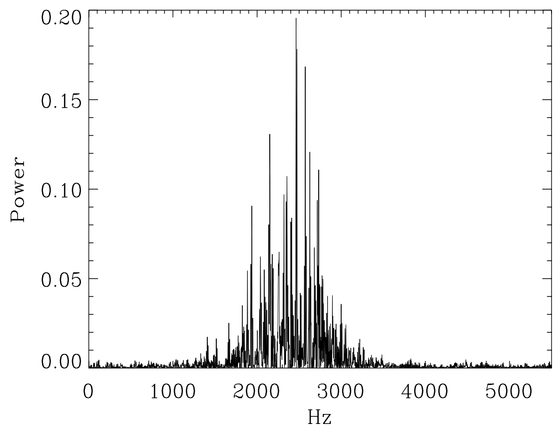

Fig. 8. The power spectrum of the p-modes heard on a daily basis in building 520 of Aarhus University, near Hans Kjeldsens office (see also Fig. 2).

For comparison we show in Fig. 8 the power spectrum of the p-mode oscillations measured close to Hans Kjeldsens office (Fig. 2). The similarity between Fig. 5 and Fig. 8 is astonishing indeed, with the only significant difference being the shift in frequency of the excess power. After shifting the frequencies by 10^6 of the data shown in Fig. 8 we de-correlate the time series from VLT with the time series of the p-mode oscillations measured close to Hans Kjeldsens office, and the resulting power spectrum is shown in Fig. 9. This result indicates that the claimed solar-like oscillation in α Cen A (Bedding et al. 2004) could in fact just be oscillations in the instrument caused by the strong p-mode vibrations as Hans Kjeldsen is laughing. To fully explain the correlation between the two datasets would require that the vibrations from Hans Kjeldsen are shifted by the surrounding media e.g. service building, telescope dome, telescope structure, and instrument. Due to the large difference in radius of Hans Kjeldsens lungs and the telescope dome we estimate the shift in frequency of Hans Kjeldsens excess power using the scaling relation by Brown et al. (1991). It can explain the required shift within the errors introduced by the effect from the service building, telescope structure, instrument and even the mountain which are not taken into account. Furthermore we assumed that both the telescope dome and Hans Kjeldsen are spherical objects which is a small approximation though.

To further strengthen our hypothesis we show seismic measurements from the seismic network CINCA95 (near Antofagasta) obtained both at the time Hans Kjeldsen was observing at VLT (Fig. 10), and after he left Chile (Fig. 11). These two power spectra show extremely good evidence that the ex-

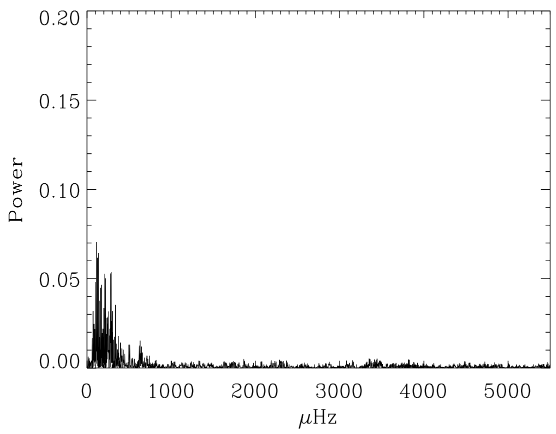

Fig. 9. The VLT power spectrum after de-correlation with the signal shown in Fig. 8

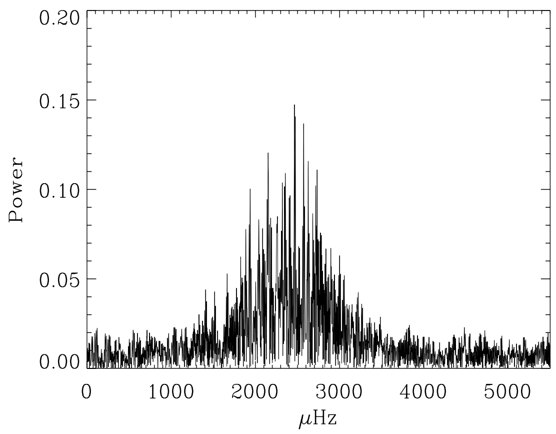

Fig. 10. Seismic measurements from the seismic network CINCA95 (near Antofagasta), when Hans was observing at VLT.

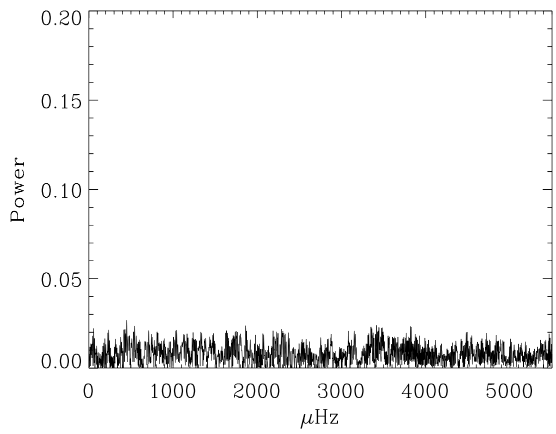

Fig. 11. Seismic measurements from the seismic network CINCA95 (near Antofagasta), after Hans had returned home after his observing run.

Fig. 12. The detected noise source. He might look innocent, but this expert in noise can ruin your data.

cess of power seen in Fig. 6 is due to the presence of Hans Kjeldsen and not of stellar origin. The larger noise in these spectra compared to Fig. 6 is due to the slightly larger distance between the p-mode source and the detecting devices. The seismic measurements from Kort- og Matrikelstyrelsen obtained near Hans Kjeldsens home show a very similar structure of excess power, but reversed (i.e. no power excess when Hans Kjeldsen was in Chile, and clear signal after returning home).

Finally, we explain how power excess similar to Fig. 6 was observed in the AAT data (Fig. 7). Due to close mate ship between one of the authors and people internal in ESO (we will not mention any names...you know...have to kill you) we got access to lists of phone calls to and from Cerro Paranal (VLT) during the 2001 observing run of α Cen A. These lists show several long, nearly continuous, phones calls between Cerro Paranal and Siding Spring in Australia (AAT). This unusual intense telephone contact can explain the excess power in the AAT power spectrum as resonances from Hans Kjeldsen via phone to the AAT dome. The extra noise from the relelatively poor phone connection explains the slightly higher noise in the AAT data (Fig. 7).

4. Concluding remarks

Our very thorough examination of the α Cen A data (Butler et al. 2004) provide clear evidence of how crucial it is to fully understand the noise sources involved when observing solar-like oscillations. By several independent measurements we show that the source of p-modes, claimed to be of stellar origin from α Cen A (Bedding et al. 2004), are in fact coming

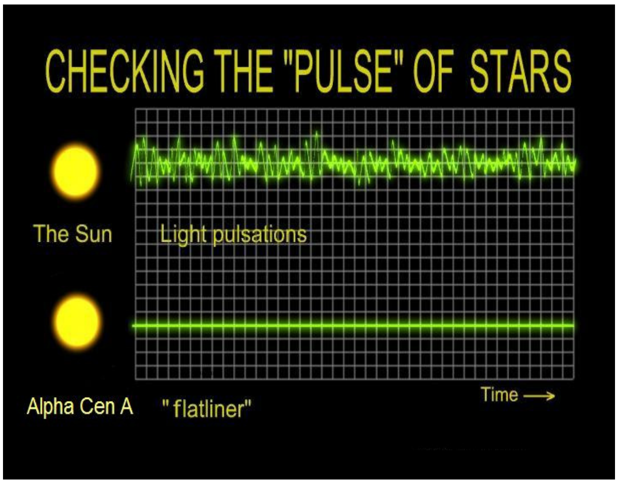

Fig. 13. The results of the present paper summarized in a single figure, comparing the light curves of the Sun and of α Cen A.

from a, by some people, unexpected (by others not so unexpected) noise source. Due to the unambiguity of our results we can reveal the source of noise beyond any doubt (see Fig. 12).

With these results, we are left to the conclusion that α Cen A is just another flat-liner (Fig. 13)

Acknowledgements. We would like to thank Dr. Hans Kjeldsen for always maintaining a positive and constructive atmosphere wherever he goes, and for funding this publication. We acknowledge the contribution from Cafe Ris-Ras in Aarhus especially their fantastic Belgian beer which stimulated our discussion of the present work.

References

Bedding, T. R., Butler, R. P., Kjeldsen, H., et al. 2001, ApJ, 549, L105
Bedding, T. R., Kjeldsen, H., Butler, R. P., et al. 2004, apJ, submitted
Brown, T. M., Gilliland, R. L., Noyes, R. W., & Ramsey, L. W. 1991, ApJ, 368, 599
Butler, R. P., Bedding, T. R., Kjeldsen, H., et al. 2004, ApJ, 600, L75
Kjeldsen, H. & Bedding, T. R. 1995, A&A, 293, 87
Martić, M., Schmitt, J., Lebrun, J.-C., et al. 1999, A&A, 351, 993
Matthews, J. M., Kusching, R., Guenther, D. B., et al. 2004, Nature, 430, 51